THE UNIVERSITY OF CHICAGO

IMPACT CRATER STATISTICS AND THE HISTORY OF RIVERS ON MARS

A DISSERTATION SUBMITTED TO
THE FACULTY OF THE DIVISION OF THE PHYSICAL SCIENCES
IN CANDIDACY FOR THE DEGREE OF
DOCTOR OF PHILOSOPHY

DEPARTMENT OF THE GEOPHYSICAL SCIENCES

BY
SAMUEL HOLO

CHICAGO, ILLINOIS
MARCH 2021

This dissertation is dedicated to Dr. Stephen Palfrey, who taught me to apply myself.

“Let there be songs to fill the air” -Jerry Garcia

TABLE OF CONTENTS

LIST OF FIGURES

LIST OF TABLES

LIST OF CODES

ACKNOWLEDGMENTS

There are numerous people to whom I am grateful. My advisor, Edwin Kite, never failed to challenge me intellectually. My committee members, Dorian Abbot and Susan Kidwell, provided valuable insight as I developed scientifically. The faculty and staff of the Department of Geophysical Sciences created a stimulating environment in which I was excited to learn. Special thanks go to my DoGS friends: Jade Checlair, Nigel Brauser, Andrew Heard, Gaia Stucky de Quay, Anne Davis, Dylan Gaeta, Kellie Swadba, and Rich Lyons.

Finally, I also thank my family: Robert, Christine, and Johanna Holo, as well as Lindsey McClary, Halston Lim, Andrew Stier, Steven-Louis Dreyfus, Mathieu Rolfo, Justin Gilston, Andre Manuel, Brian Zdeb, Claudia Cañamas, Marlon Facey, Zach Lipel, Anup Kishore, Valerie Pietrasz, Nicholas Perry, Stephen Palfrey, Michael Lamb, and Marisa Palucis.

ABSTRACT

River valleys and deposits record periods of time when Mars' climate supported liquid water on the planet's surface. However, the majority of geomorphic studies focus on detailed reconstructions of local or regional hydrology, thereby limiting our global understanding of Mars' climate through time. In this dissertation, we set out to constrain our view of Mars' climate history through novel applications of impact crater statistics. Impact craters are ideal for probing the history of river erosion because (a) they formed globally throughout history and (b) they record geologic and solar system processes in their morphologies and populations. In Chapter 2, we tested the hypothesis that ancient Martian surfaces were subjected to intense resurfacing by river erosion. Using statistical methods developed by astronomers to detect galactic clustering on the celestial sphere, we found that resurfacing on the ancient Martian highlands was shallower than previously expected. In Chapter 3, we investigated the duration of chaotic high-obliquity excursions, which are believed to have enabled river-forming climates in the last $\sim$ 3.5 Gyr. Using a novel model relating Mars' obliquity to the distribution of elliptic impact crater orientations, we found that the amount of time Mars spent in a high obliquity state was $\sim$ 50% lower than expected. In Chapter 4, we used global databases of impact craters and alluvial fans to constrain parameters in a statistical model for global fan formation. We found that climate-driven alluvial fan formation likely persisted into the last $\sim$ 2.5 Gyr. In Chapter 5, we synthesized our work and described how our observations together directionally affect our view of Mars' climate evolution. In the supplementary files, we include minor planet center and elliptic crater data.

CHAPTER 1

INTRODUCTION

1.1 Context and Motivation

Mars has been the target of robotic space exploration for over 50 years. The numerous landed and orbital missions to Mars were equipped with scientific instruments to decipher the physical and chemical properties of Mars' surface, shallow subsurface, and atmosphere. Despite this incredible diversity and abundance of data, this thesis focuses exclusively on Mars' surface geomorphology, as observed from orbit in both images (visible and thermal) and topographic data (derived from laser altimetry and visible image stereopairs).

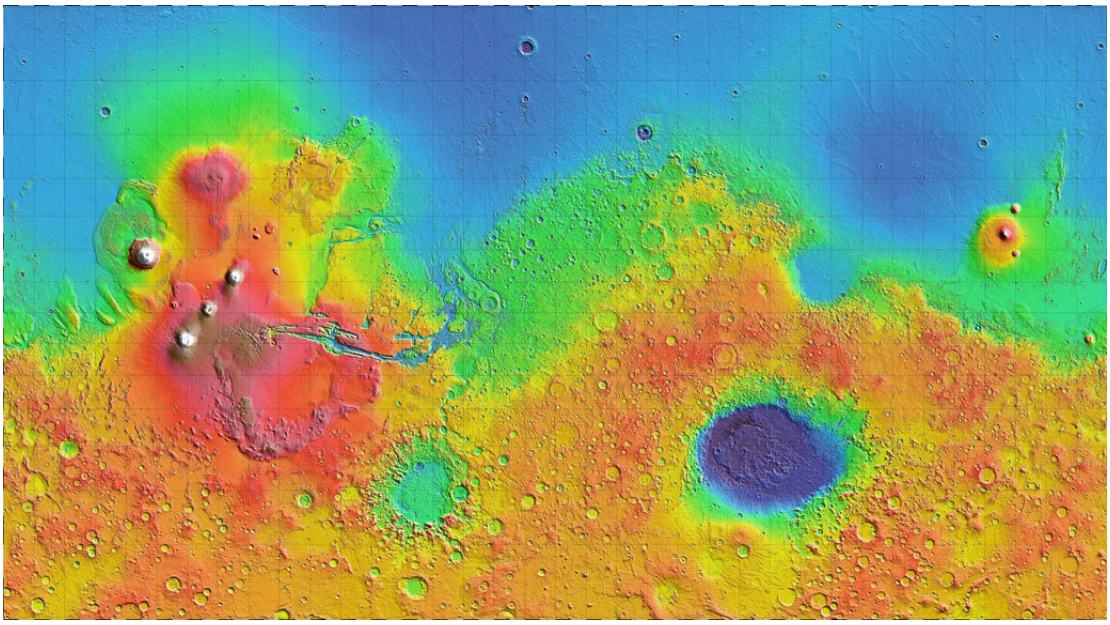

Figure 1.1: Global MOLA Topography of Mars (75° S to 75° N). The southern highlands (red, sit at ~ 4 km elevation) are heavily cratered, while the northern lowlands (lowest points, colored dark blue, sit at ~ -8 km elevation) are relatively smooth. High points in white sit at ~ 12 km elevation. Mars' circumference is $\sim 21 \times 10^3$ km.

Evident in the global topography of Mars as measured by the Mars Orbiter Laser Altimeter (MOLA) on the Mars Global Surveyor, is a hemispheric topographic dichotomy where the southern hemisphere sits several kilometers above the northern hemisphere (Figure 1.1).

Further, the high-standing southern hemisphere is clearly heavily-cratered, indicating an ancient age of ~ 3.8 Ga (see among many others, Fassett 2016). Thus, Mars' surface provides an ancient geologic record that is difficult to access on Earth. In addition, images reveal that these ancient terrains preserve river valleys and deposits, indicating that Mars' climate once supported flowing liquid water on its surface (see among many others, Kite 2019). This observation leads to an apparent paradox. Mars receives too little solar insolation to support surface liquid water today, but solar insolation is expected to have been even lower when these rivers formed billions of years ago (see among many others, Wordsworth 2016). As a result, Mars has become a critical data point in understanding the evolution of planetary climates in general (see Kite 2019).

Perhaps the most striking observation that indicates past surface liquid water on Mars is regionally-integrated valley networks on the ancient highlands (Fassett and Head, 2008; Hynek et al., 2010; Fassett and Head, 2011). These valley networks, with apparent branching tributaries, bear a clear resemblance to mountain rivers on Earth (Figure 1.2). While it has been suggested that the valley networks could have formed from fluids other than water (like CO_2; e.g. Hoffman, 2000), detection of abundant aqueous mineral alteration on Mars' surface and in Mars' sub-surface indicates that water is the most likely (see among many others, Arvidson, 2016). Detailed studies of valley network morphometry enable estimates of landscape-averaged erosion (Luo et al., 2017), as well as reconstructions of peak discharges and runoff production using empirical hydraulic relationships derived from Earth data (e.g. Irwin et al., 2005; Irwin et al., 2005b). Although these relationships are known to have order-of-magnitude uncertainty (e.g. Dietrich et al. 2017), they provide an important constraint on precipitation and/or snowmelt rates on early Mars (see Kite 2019). We note that it is possible that these valley networks formed by groundwater sapping rather than erosion by surface runoff, but groundwater sapping is likely unable to reproduce the deep erosion into bedrock (Lamb et al., 2006) and spatially-extensive, regionally-integrated branching networks observed (Craddock and Howard, 2002).

Despite their clear relevance to constraining early Martian climate, the valley networks have inherently limited utility for constraining the evolution of Mars' climate through time. Counting craters that cross-cut valley networks has revealed that the majority of valley networks stopped forming near the Noachian/Hesperian boundary, $\sim$ 3.6 Ga (e.g. Fassett and Head, 2008; Fassett and Head, 2011). Further, regional analysis of valley network lengths, slopes, and depths indicates that the valley networks began forming late in the Noachian, with a spatial signature of fluvial erosion that differs from the early and middle Noachian (Howard et al., 2005). Thus, the valley networks only represent a narrow slice of time in Mars' history. In order to fully constrain Mars' climate evolution, one must consider the river activity that occurred both before and after the era of regionally-integrated valley network formation.

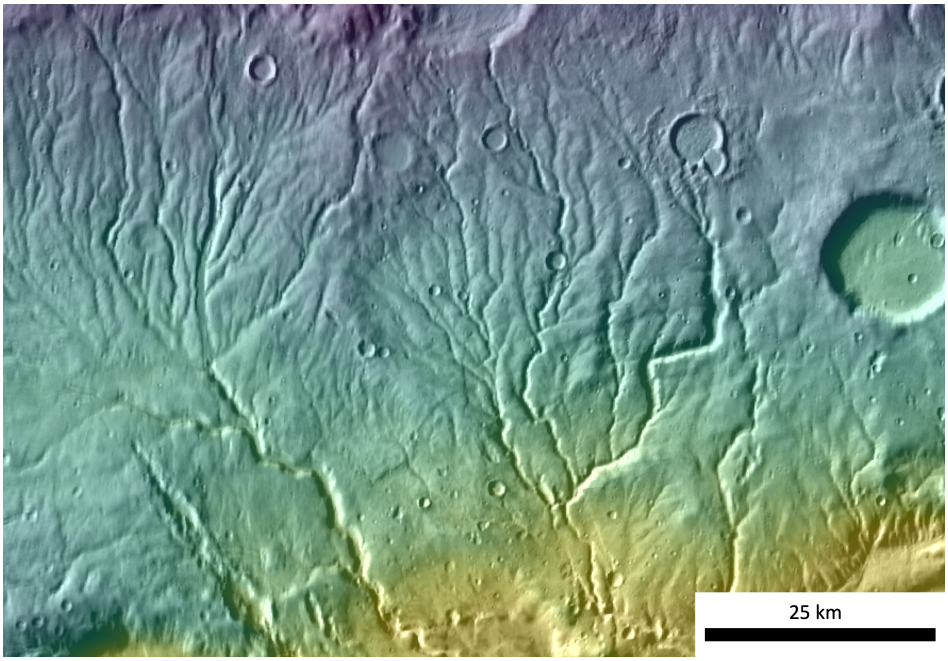

Figure 1.2: Example Late-Noachian/Early-Hesperian Valley Networks. HRSC/MOLA 200m colorized topography over THEMIS daytime IR (267° E, 42° S). Numerous tributaries are apparent and merge downstream. Topography color-scale ranges from yellow (elevation $\sim$ 2.5 km) to blue (elevation $\sim$ 5.5 km). North is towards the top of the page. Apparent lighting direction from NW to SE.

Impact cratering is ubiquitous in the solar system, and hundreds of thousands of impact craters are preserved on Mars' surface (Robbins and Hynek, 2012). These impact craters have

continued to form since the period of heavy bombardment (see among many others, Fassett, 2016). Further, they record surface processes such as fluvial erosion, aeolian infilling, volcanic infilling, and diffusion in their topography (e.g. Craddock and Maxwell, 1990; Moore and Howard, 2005). In particular, fluvial erosion is known to have modified impact craters both before the formation of regionally-integrated valley networks (e.g. Craddock and Maxwell, 1993; Forsberg-Taylor et al., 2004; Howard et al., 2005; Irwin et al., 2005; Howard 2007) and after the formation of regionally-integrated valley networks (e.g. Moore and Howard, 2005; Kraal et al., 2008; Mangold et al., 2012a; Wilson, et al., 2016; Morgan and Wilson, 2019; Palucis et al., 2020). During these time periods, rivers were much shorter and possessed fragmented drainage networks (e.g. Howard et al., 2005). Because ancient crater degradation is ubiquitous (e.g. Craddock and Maxwell, 1993; Forsberg-Taylor et al., 2004) but recent fluvial modification is more sparse (e.g. Kraal et al. 2008, Wilson et al. 2016), planetary geoscientists typically anchor themselves on what we will call the "prevailing view" of the history of rivers on Mars (Figure 1.3). In this view, the scale of fluvial erosion declined quickly early in Mars' history, with intermittent river-forming climates in recent history (e.g. Kite et al., 2017a).

In this thesis, we set out to demonstrate that a global view of impact cratering and crater degradation can place new constraints on Mars' fluvial history. In particular, we will demonstrate that impact craters have unique utility because they are globally distributed and thus enable global, statistically significant statements about Mars' fluvial history. This work builds on an existing research theme, where quantitative crater degradation trends in space or time are used to unravel climatic forcing on crater modification (e.g. Craddock and Maxwell, 1993; Forsberg-Taylor et al., 2004; Grant and Wilson, 2011; Mangold et al., 2012a; Weiss and Head, 2015; Kreslavsky and Head, 2018; Morgan and Wilson, 2019). In particular, we aimed to extend this overall approach in two ways: (a) extend analyses to global studies using newly available global datasets (e.g. Robbins and Hynek, 2012; Tanaka et al., 2014; Morgan and Wilson, 2019) and (b) go beyond crater counts or morphologic trends and use

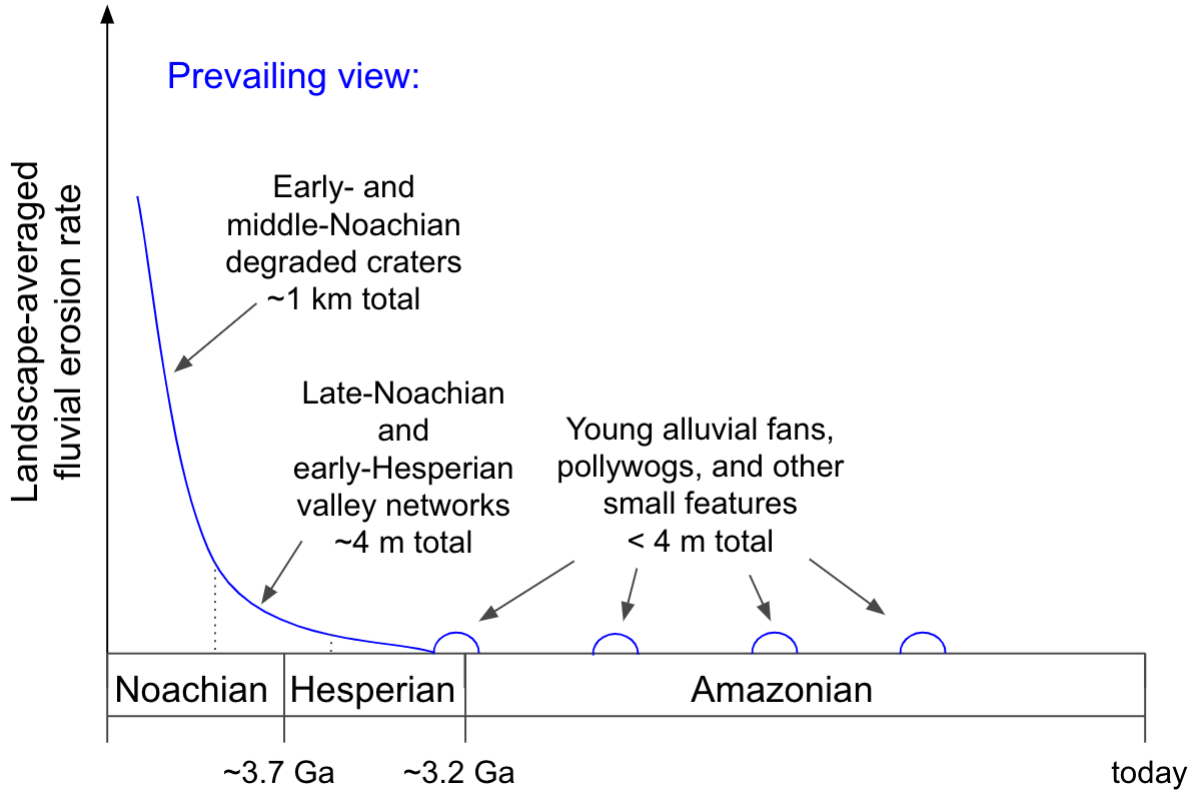

Figure 1.3: Prevailing View of the History of Fluvial Erosion on Mars. Fluvial erosion declined rapidly early in Mars' history, with intermittent, river-forming climates occurring in the Hesperian and Amazonian. Figure not drawn to scale.

additional crater information (e.g. ellipticities or crater spacing) for quantitative inference of climate-relevant parameters.

In the coming sections, we will describe how crater populations are most commonly interpreted on Mars currently, as well as shortcomings of the existing paradigms. In the following chapters, we will describe three examples of how statistical modeling of global crater populations enables new constraints on the amount, timing, and frequency of fluvial erosion throughout Mars' history. Further, we will argue that our constraints favor an alternate view of Mars' fluvial history in which fluvial activity resulted from intermittent and transient river-forming climates, rather than from a steadily declining propensity for precipitation/snowmelt.

1.2 The Cratering Record of Mars

Impact craters are ubiquitous on Mars. Indeed, over 600,000 unique craters have been identified (Robbins and Hynek, 2012), and even more are being mapped as higher resolution imagery becomes readily available. Impact craters are most commonly used as a chronometer in solar system science because geologic surfaces are expected to accumulate craters as time passes (Fassett, 2016). On Mars, the story is complicated by the fact that surface processes that are known to have modified impact craters (e.g. Craddock and Maxwell, 1993; Moore and Howard, 2005) may also be responsible for fully obliterating craters, censoring them from surveys (e.g. Öpik 1966; Chapman and Jones, 1977; Cradock and Maxwell 1990; Robbins et al., 2013; Quantin-Nataf et al., 2019; Palucis et al., 2020). In this section, we review how impact crater data is visualized and used for retrieving age estimates for geologic surfaces. Further, we discuss shortcomings of existing methodologies in interpreting the record of cratering and crater obliteration.

1.2.1 The Martian Chronology Function

The primary method of obtaining absolute age estimates on Mars is through comparing measured crater densities to the chronology function, which represents the expected relationship between crater density and time (e.g. Michael, 2013). However, to construct the chronology function in the first place, one must obtain crater counts from areas with known absolute age. Such calibration points are provided by lunar samples collected by the Apollo and Luna missions (see Fassett, 2016). To relate the lunar chronology to the Martian chronology, several corrections need to be made. One must correct for the difference in the expected number of impactors per unit surface area, differences in typical impact velocity, differences in gravity, and differences in atmospheric filtering of small craters (e.g. Ivanov, 2001; Neukum et al., 2001; Hartmann and Neukum, 2005; Hartmann, 2005). The resultant Martian chronology (Figure 1.4; from Michael, 2013, based on Hartmann, 2005) suggests that impactor flux has

been relatively constant for the last $\sim$ 3 Gyr but exponentially declined between $\sim$ 4 and $\sim$ 3 Ga.

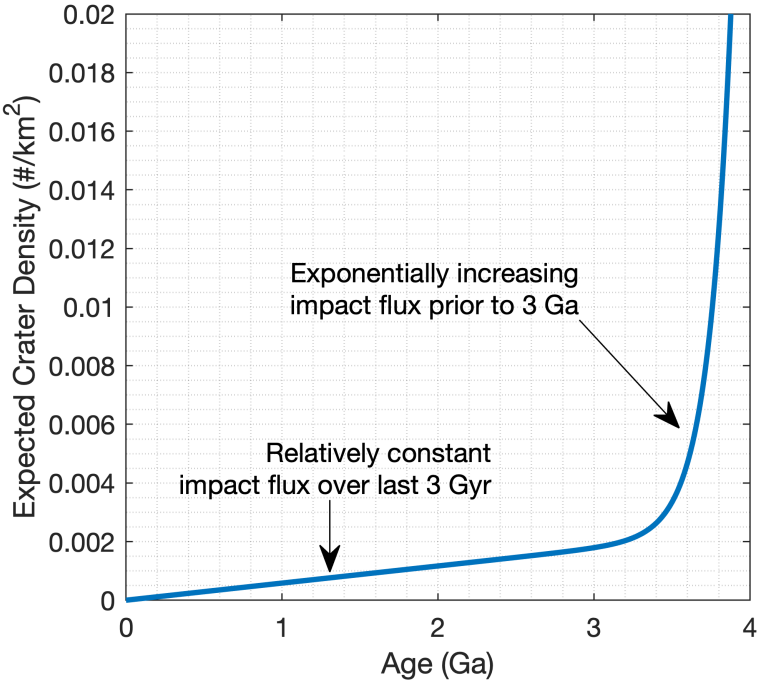

Figure 1.4: The Chronology Function of Mars. Chronology function as reported by Michael (2013), based on Hartmann (2005). Over the last 3 Gyr, impact flux has been relatively constant, while impact flux exponentially decreased between 4 and 3 Ga.

An alternate approach to constructing or calibrating chronology functions is through direct dynamical modeling of the inner solar system (see Fassett, 2016). Although models differ in detail, they generally agree that the modern solar system has been in an approximate steady state for the last $\sim$ 3 Gyr (e.g. Bottke et al., 2002; Bottke et al., 2005; Nesvorny et al., 2017). This enables confidence in the belief that Mars' impactor flux has also been steady for the last $\sim$ 3 Gyr. However, the dynamical history of the solar system prior to $\sim$ 3 Ga continues to be debated today. Models differ in proposed early impactor populations, as well as in the timing and trigger of dynamical instabilities (see among others Bottke and Norman, 2017; Nesvorny et al., 2017; Marchi, 2020). Because of this, the pre-3 Ga Martian impactor flux is highly uncertain. Indeed, in situ radiogenic dating of Martian rocks indicate that crater rim materials from Gale have a K-Ar age $>\sim$ 4 Ga, which is older than estimated

from crater counting (Farley et al., 2014). Further, new crater count data from the lunar sample sites has motivated further updating of the lunar chronology (Robbins, 2014). As a result, absolute ages should all be taken with a grain of salt (recent studies suggest that surfaces inferred to have ages 2-3 Ga have the largest uncertainty; Robbins, 2014).

1.2.2 The Martian Crater Production Function

When applying the chronology function to estimate absolute ages, one must account for the size range of craters considered (e.g. Fassett, 2016). Craters span orders-of-magnitude in size, but large craters are orders-of-magnitude less numerous (Figure 1.5). Further, smaller craters are shallower and thus preferentially susceptible to obliteration by erosion/burial and thus censorship from crater counts. Thus, to evaluate the dependence of crater density on crater diameter, one typically visualizes the crater count data in what is referred to as an incremental crater size-frequency distribution (CSFD) plot (Figure 1.5). This name is a misnomer, but we will adopt the terminology for consistency with the literature. Incremental CSFD's are constructed by counting the craters over a defined area, binning them by diameter (usually bins edges are defined by $2^{n/2}$ km, for all n), and dividing the number of craters in each bin by the count area. Standard errors are assumed to be the square root of the number of craters – motivated by the standard deviation in a Poisson distribution. While these errors approximately account for uncertainties arising from counting statistics, they do not account for uncertainty in the crater counts that arises from human judgment when determining a crater's diameter (e.g. Robbins et al., 2014) or whether a crater is a secondary crater (Robbins and Hynek, 2014). Ultimately, this procedure results in a curve that demonstrates not only the relative contribution of different crater diameters to the population (shape of the curve) but also the overall density of craters in the area (vertical positioning of the curve). In principle, steep incremental CSFD's can be limited by saturation equilibrium at small diameters and high overall densities, when new crater emplacement perfectly balances obfuscation of older craters by the new craters (see dark dotted line, Figure 1.5). However,

crater saturation is not generally believed to affect interpretations of crater populations on Mars (although it is likely relevant on heavily cratered terrains on the Moon and Mercury; see Fassett, 2016).

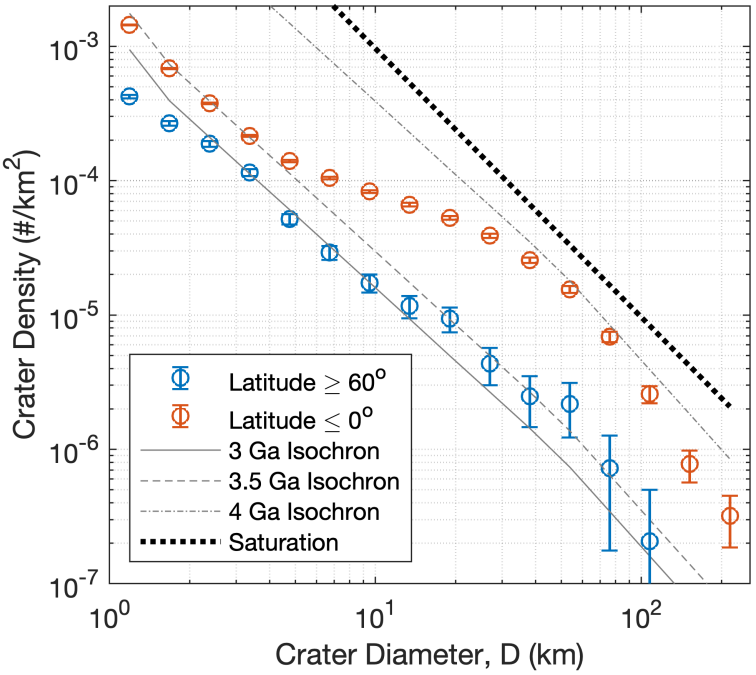

Figure 1.5: Example Crater Size-Frequency distributions and Isochrons. CSFD's (2σ errors) from the southern hemisphere and northern polar region (latitude $\geq 60°$) plotted over 3, 3.5, and 4 Ga isochrons. Dark dashed line shows the geometric saturation curve. Crater data was taken from Robbins and Hynek (2012), with isochrons as reported in Michael (2013).

In order to correct chronology inferences for the size of craters surveyed, one must develop a model for the dependence of crater density on crater diameter, which is commonly known as the production function (e.g. Ivanov et al., 2002; Hartmann, 2005). However, because ancient terrains suffer from erosion/burial of small craters and small terrains suffer from poor counting statistics of the less dense large craters, the production function cannot be determined from crater counts on a single surface (see Fassett, 2016). Thus, existing estimates (e.g. Ivanov et al., 2002; Hartmann, 2005) are stitched together from crater counts at different diameters on different terrains. This has two key problems. First, this procedure requires human judgment about which diameters are acceptable for use on each terrain. Second,

it assumes that the diameter dependence of crater density is unchanged through time and can be inferred from different-aged surfaces. Together, these problems make reproducing production function estimates difficult. Indeed, the two most common production functions for Mars (Ivanov et al., 2002; Hartmann, 2005) differ substantially from each other for craters > 1 km in diameter (see Fassett, 2016).

To infer ages from incremental CSFD's, one typically constructs isochrons, which are production function curves scaled by the expected overall crater density as a function of time (see Figure 1.5; Fassett, 2016). Despite some problematic assumptions (i.e. that binning crater diameters does not introduce bias and that count data is sufficient to justify approximating uncertainties as normal distributions), one typically estimates the age of a surface by fitting isochrons to incremental CSFD data via weighted least squares regression for bins above a critical diameter. There is no widely accepted, systematic method for determining this critical diameter. In some special cases like crater counts on fresh superposed lava flows, the critical diameter is visually obvious due to a step function shift at some diameter in the CSFD, with crater densities at bins above and below the cutoff diameter matching isochrons (corresponding to the first and second lava flow ages, respectively) nearly exactly (see Fassett, 2016). However, most surfaces do not produce visually striking matches to isochrons, and further, their deviations from isochrons at small diameters are smooth, rather than clear step functions (Figure 1.5). This is commonly interpreted to represent continuous, spatially varying resurfacing of the count area systematically obliterating small craters in greater proportions than larger craters (e.g. Robbins et al., 2013; Quantin-Nataf et al., 2019; Palucis et al., 2020). In this framework, the cutoff diameter, above which isochrons fit the data well, represents the maximum diameter of craters eroded/buried by surface processes. This in turn corresponds to a maximum depth of erosion/burial in that area (e.g. Robbins et al., 2013; Quantin-Nataf et al., 2019; Palucis et al., 2020). In the next section, we review geologic observations of crater degradation and discuss how crater counts, isochron fitting, and age estimation have been used to make inferences about fluvial erosion in Mars' past.

1.3 Crater Degradation on Mars

Craters formed on Mars produce predictable morphologies with consistent initial depths, well defined rims, easily identified ejecta deposits, and central peaks (for complex craters). Because of this consistency in the morphology of fresh craters, it is relatively straightforward to identify craters that have been modified by geologic surface processes (Figures 1.6 and 1.7). Indeed, degraded craters are ubiquitous on Mars and record in their style of modification the history of surface processes (e.g. Mangold et al., 2012a). In the coming sections, we review the observations and significance of major crater degradation styles both prior to and after the era of regionally-integrated valley network formation. Further, we review some examples of how existing crater statistics methodologies have been used to make inferences about the timing, magnitude, and rates of fluvial activity throughout Mars' history.

1.3.1 Noachian Crater Degradation

The majority ($\sim 75\%$) of craters on low-latitude Noachian terrains have been heavily degraded relative to fresh Martian craters (e.g. Craddock and Maxwell, 1993; Forsberg-Taylor et al., 2004; Mangold et al., 2012a). In particular, they possess subdued rims, flat floors, shallow interior depths, and a lack of visible ejecta (e.g. Figure 1.6; Craddock and Maxwell, 1993; Mangold et al., 2012a). The lack of regionally-integrated valley networks (e.g. Howard et al., 2005), bi-modality of crater infilling states (depth divided by expected initial depth; Forsberg-Taylor et al., 2004) and the combination of flat floors and steep walls (e.g. Craddock and Maxwell, 1993) together suggest that a combination of impact cratering and fluvial backwasting (lateral erosion) of crater walls dominated pre-valley network surface processes (Howard, 2007). In this framework, fluvial bedrock erosion rapidly infilled ancient craters via backwasting of the crater rims (Forsberg-Taylor et al., 2004), while local valley networks were disrupted by impact cratering and aeolian erosion/infilling, inhibiting regional integration (Howard, 2007). Younger craters avoided such backwasting (Forsberg-Taylor et al., 2004).

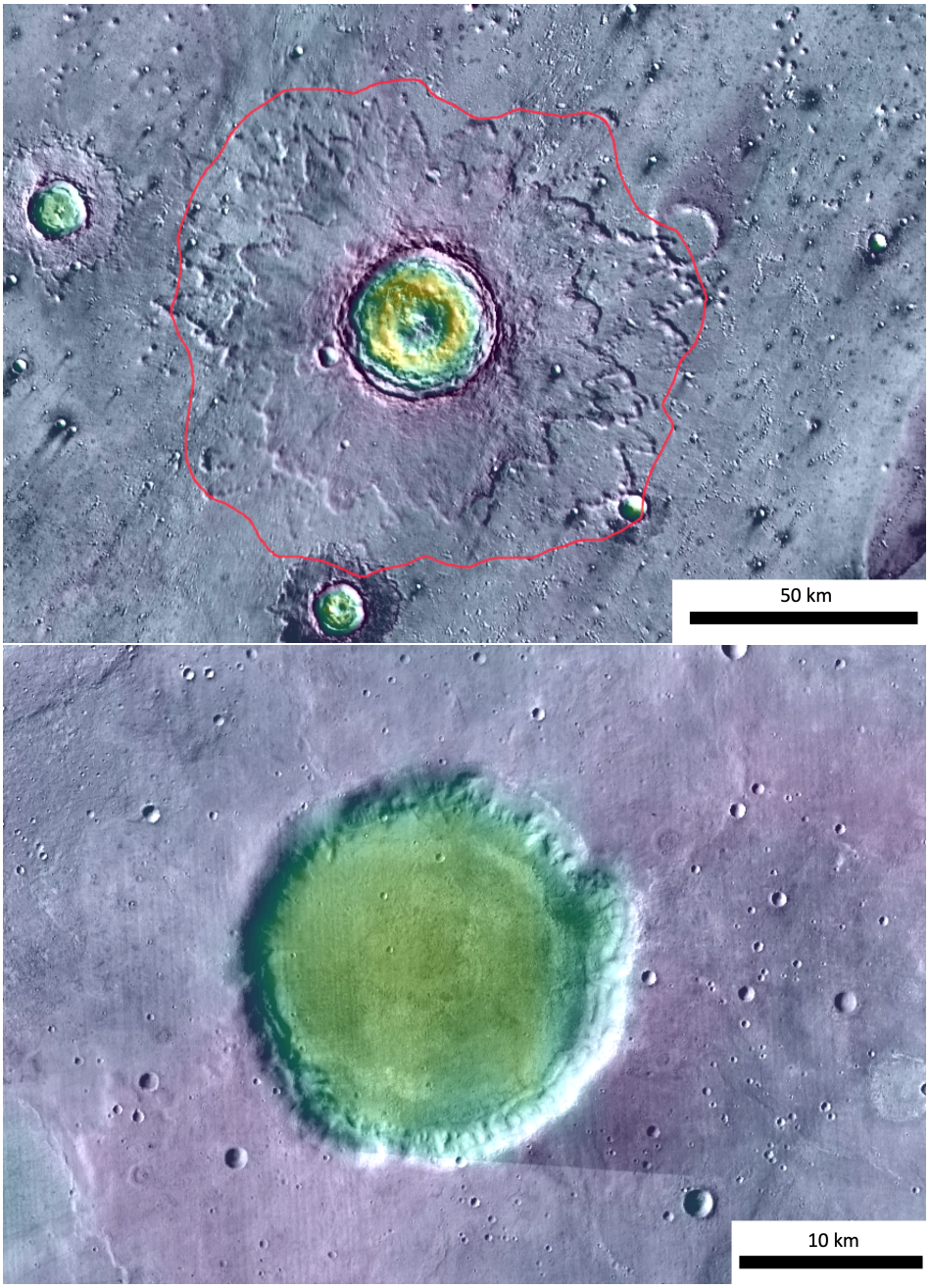

Figure 1.6: Comparison of Fresh and Noachian Craters. Top (also in Figure 4.1): HRSC/MOLA 200m colorized elevation over THEMIS daytime IR image of fresh impact crater (321° E, 26° N), with red outline around the ejecta as mapped in Tanaka et al. (2014). Note the preservation of the ejecta, rim, and central peak. Illumination is from SW to NE. Colorized elevation goes from yellow (elevation ~ -5 km) to indigo (elevation ~ -3 km). Bottom: HRSC/MOLA 200m colorized elevation over CTX Global Mosaic image of a typically degraded Noachian impact crater (358° E, 32° S). Note the flat floor, subdued rim, and lack of visible ejecta. Illumination is from NW to SE. Colorized elevation goes from yellow-green (elevation ~ 0.9 km) to indigo (elevation ~ 1.5 km). North is towards the top of the page in both images.

In models (e.g. Howard, 2007), these surface processes (including fluvial erosion) are sufficient to bury craters and censor them from surveys. However, the total contribution of these surface processes (and the relative contribution of fluvial erosion) to crater obliteration remains unknown. Some studies have used the cutoff-diameter in isochron fits (see discussion of the production function above) to reconstruct maximum resurfacing depths as a function of time (Robbins et al., 2013; Quantin-Nataf et al., 2019). These studies (Robbins et al., 2013; Quantin-Nataf et al., 2019) both indicate erosion/burial rates that sharply decline during the Noachian, consistent with the prevailing view of Mars' fluvial history (Figure 1.3). However, this conclusion is heavily dependent on the assumption that the production function did not change through time and that deviations of Noachian crater counts from isochrons at small diameters (see Figure 1.5) are in fact the result of obliteration by surface processes. This assumption is not secure, as crater counts from multiple terrestrial planets possess an apparent shift in the crater production function across surfaces of different ages (Strom et al., 2005; Fassett et al., 2012; Strom et al., 2015). In chapter 2 of this thesis, we describe a new test of this hypothesis and discuss the implications for reconstructing Noachian resurfacing (Holo and Kite, 2020).

1.3.2 Hesperian and Amazonian Crater Degradation

The majority of craters on Hesperian and Amazonian terrains maintain a fresh appearance, with easily visible rims (e.g. Figure 1.7). Despite their recent age and general fresh appearance, young craters have also been subjected to degradation by fluvial processes. Indeed, since the early Hesperian, $\sim$ 3.4 Ga, fluvial processes were responsible for producing landforms such as small, 'pollywog', exit breach craters (Wilson et al., 2016; Warren et al., in press), alluvial fans (e.g. Figure 1.7; Moore and Howard, 2005; Kraal et al., 2008; Grant and Wilson, 2011; Hauber et al. 2013; Kite et al. 2017b; Morgan and Wilson, 2019), and gullies (which may or may not be fluvial in origin; see Conway et al., 2019). The pollywog craters and alluvial fans (including deltas, which form in standing bodies of water rather than dry basins)

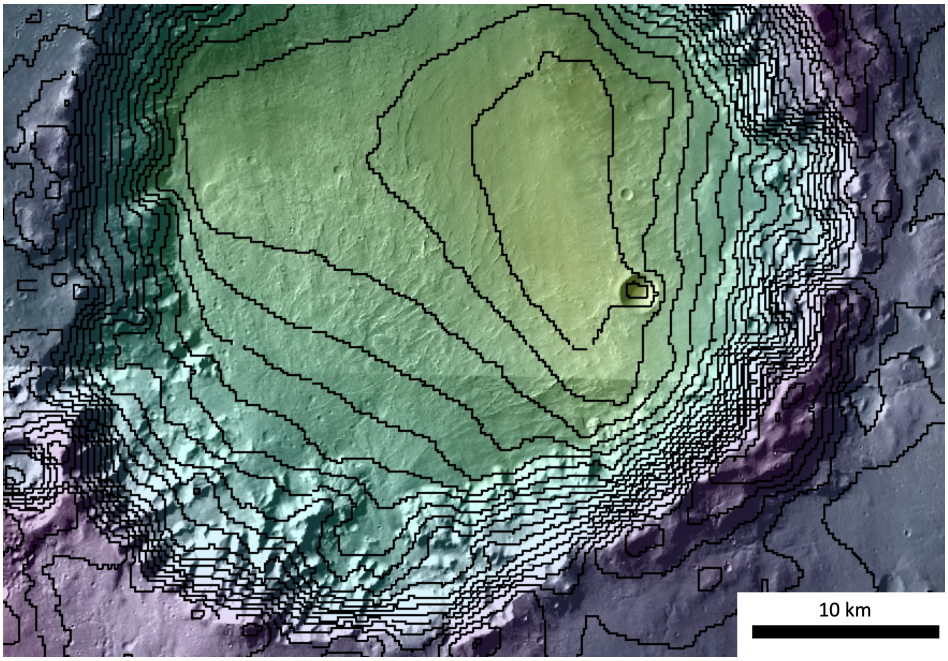

Figure 1.7: Example Crater-Hosted Alluvial Fan (also in Figure 4.1). HRSC/MOLA 200m colorized elevation over CTX Global Mosaic image of a large crater-hosted alluvial fan deposit, formed by erosional backwasting of the southwestern crater rim (333° E, 29° S). Contour spacing is 100m. North is towards the top of the page, and colorized elevation goes from green (low) to indigo (high).

unambiguously record periods of fluvial activity in a climate that is expected to otherwise be cold and dry due to rapid atmospheric loss early in Mars' history (e.g. Carr, 1979; Kite et al., 2019). The apparent erosion of bedrock in alluvial fan alcoves (e.g. Stucky de Quay et al., 2019) and pollywog outflow valleys (e.g. Warren et al., in press) is difficult to achieve with groundwater (e.g. Lamb et al., 2006), especially with channel heads near local topographic maxima (i.e. crater rims). Thus, explaining the presence of these fluvial features is critical for constraining post-valley network climate evolution on Mars.

Several mechanisms can, in principle explain recent runoff-driven fluvial activity. The first is localized impact triggers, in which impacts themselves provide the energy to induce local precipitation and/or snowmelt (e.g. Williams and Malin, 2008; Mangold et al., 2012b). However, detailed studies of alluvial fans indicate that localized-impact trigger cannot be the sole mechanism responsible (Irwin et al., 2015). For example, Kite et al. (2017b)

performed surveys of syn-fluvial craters (those that formed while fan buildout was still active), interbedded in alluvial fan deposits. By carefully considering the area over which one might find interbedded craters, Kite et al. (2017b) determined a fan build-up duration of $\sim 20 - 200$ Myr by estimating the time required to accumulate the observed syn-fluvial craters (see chronology function section above). In addition, detailed morphometric studies of ~ 1 km thick alluvial fans and their channels reveal that rivers had to have flowed for $\sim 10^2 - 10^6$ years, based on earth-calibrated, semi-empirical hydraulic and sediment transport relationships (Irwin et al., 2015; Stucky de Quay et al., 2019). These timescales are too long to be explained by localized impact trigger (Turbet et al., 2020), and so these observations of large alluvial fans require an alternate explanation (e.g. Kite et al., 2017b).

The other leading candidate mechanisms for enabling surface liquid water on post-valley network Mars are transient greenhouse atmospheres (e.g. Kite et al., 2017a) and obliquity-shift induced snowmelt/precipitation (e.g. Irwin et al., 2015). In the transient greenhouse atmosphere scenario, greenhouse gases are released from some geologic reservoir (e.g. volcanoes, methane-clathrate) and transiently warm Mars' surface (e.g. Kite et al., 2017a). In the obliquity-shift induced scenario, high obliquity ($> 40°$) excursions that arise from Mars' chaotic obliquity evolution (e.g. Touma and Wisdom, 1993; Laskar and Robutel, 1993; Laskar et al., 2004) drive water ice to mid-latitudes (due to enhanced stellar insolation at the poles during summer/winter) and increase water vapor pressure, enabling melting (e.g. Jakosky and Carr, 1985; Zent, 2013; Forget et al., 2017). These scenarios are not mutually exclusive, as obliquity shifts can in principle be responsible for modulating atmospheric loss (Grimm et al., 2017), as well as triggering transient greenhouse gas outgassing (Kite et al., 2017a). In chapter 3 of this thesis, we introduce a new methodology, using the orientations of elliptic impact craters, to constrain how frequently chaotic, high-obliquity excursions occurred on Mars (Holo et al., 2018). Knowing the frequency/duration of river-forming climates is not sufficient for deciphering recent Martian rivers - one must also figure out when the river forming climates occurred. Indeed, different proposed mechanisms have different dependencies

on volcanism and/or $p\mathrm{CO}_2$, both of which declined over time (Fassett and Head, 2011). Thus, in chapter 4 of this thesis, we apply new statistical approaches to global crater and alluvial fan databases to obtain global constraints on the timing of alluvial fan formation.

1.4 Work in this Thesis

The history of river activity on Mars provides essential data for understanding planetary climate evolution in general (e.g. Kite, 2019). We have described in the previous sections how fluvial processes have modified impact craters throughout Mars' history. In this thesis, we set out to constrain our global view of Mars' fluvial history through novel applications of crater statistics. In particular, in chapter 2, we describe a new statistical test (based on statistical tests for galactic clustering on the celestial sphere) to differentiate between a changing Noachian crater size-frequency distribution and intense Noachian surface processes (Holo and Kite, 2020). In chapter 3, we describe a novel method in which elliptic craters constrain the chaotic evolution of Mars obliquity in the Hesperian/Amazonian (Holo et al., 2018). Finally, in chapter 4 we describe how age estimates and statistical modeling of alluvial fan formation can constrain the timing of global alluvial fan formation.

These studies are timely, as global Mars data has become increasingly available over the last decade but remains under-utilized. Further, impact craters are globally distributed and have well-understood initial topography, making them ideal for studies of global geomorphic evolution. Our work builds upon existing work, where quantitative crater degradation trends are reported and interpreted (e.g. Craddock and Maxwell, 1993; Forsberg-Taylor et al., 2004; Grant and Wilson, 2011; Mangold et al., 2012a; Weiss and Head, 2015; Kreslavsky and Head, 2018; Morgan and Wilson, 2019). In particular, we go beyond trends and ages, use non-traditional crater data (including ellipticities, spacing, and degradation states, not just CSFD's), and implement new statistical models. This approach allows us to robustly perform parameter estimation and model selection, the inferences from which enable quantitative interpretations of global crater populations. Further, these models and inferences

will continually produce tighter constraints on Mars' fluvial history as more data becomes available and as high performance computing resources become cheaper and more readily accessible.

CHAPTER 2

THE SPATIAL SIGNATURE OF A CHANGING ANCIENT IMPACTOR POPULATION FOR MARS

Originally published as: Holo, S.J. and Kite, E.S., The Spatial Signature of a Changing Ancient Impactor Population for Mars, Icarus, 2020. The research question addressed was conceived collaboratively by S.J.H. and E.S.K. The study's design, execution, and writing were performed by S.J.H.

Abstract. Ancient solar system processes are recorded by impact crater populations on Mars. We investigated the spatial distribution of Noachian-aged ($\sim$ 3.8-4.0 Ga) craters in order to test hypotheses for the shortage of $<$ 32 km diameter craters. Using (i) a global database of Mars impact craters and (ii) angular two-point correlation statistics to quantify local to regional crater clustering, we found that degraded craters on low-lying middle-Noachian-highland terrains were subject to spatially-patchy crater obliteration by surface processes, while older, higher-standing craters on the early Noachian highlands remain consistent with being drawn from a spatially uniform distribution. This result supports the hypothesis that the multi-sloped Noachian crater size-frequency distribution results from an early impactor population that changed during the Noachian, rather than from extensive obliteration of craters $<$ 32 km in diameter by surface processes such as fluvial erosion, volcanic flooding, and aeolian infilling. The cause of the change in impactor populations remains unknown.

2.1 Introduction

The Noachian highlands of Mars are heavily-cratered terrain that, in their geology, record ancient ($\sim$ 4 Ga) Mars, the geomorphic evolution of which remains enigmatic (e.g. Irwin et al., 2013). The majority of craters $>$ 4 km in diameter on Noachian terrain are degraded (e.g. Craddock and Maxwell, 1993), and several aspects of the Noachian highland landscape

can be explained by the interplay of impact cratering and the erosion of crater rims by fluvial erosion (e.g. Forsberg-Taylor et al., 2004, Howard, 2007). Further, examination of latitudinal/elevational trends in crater density and morphometric properties has enabled studies on the history of climatic forcing on crater modification and degradation (e.g. Craddock and Maxwell, 1993; Bouley and Craddock, 2014; Kreslavsky and Head, 2018). While we see abundant evidence for crater degradation by surface processes, our understanding of ancient resurfacing and crater obliteration remains incomplete (Irwin et al., 2013).

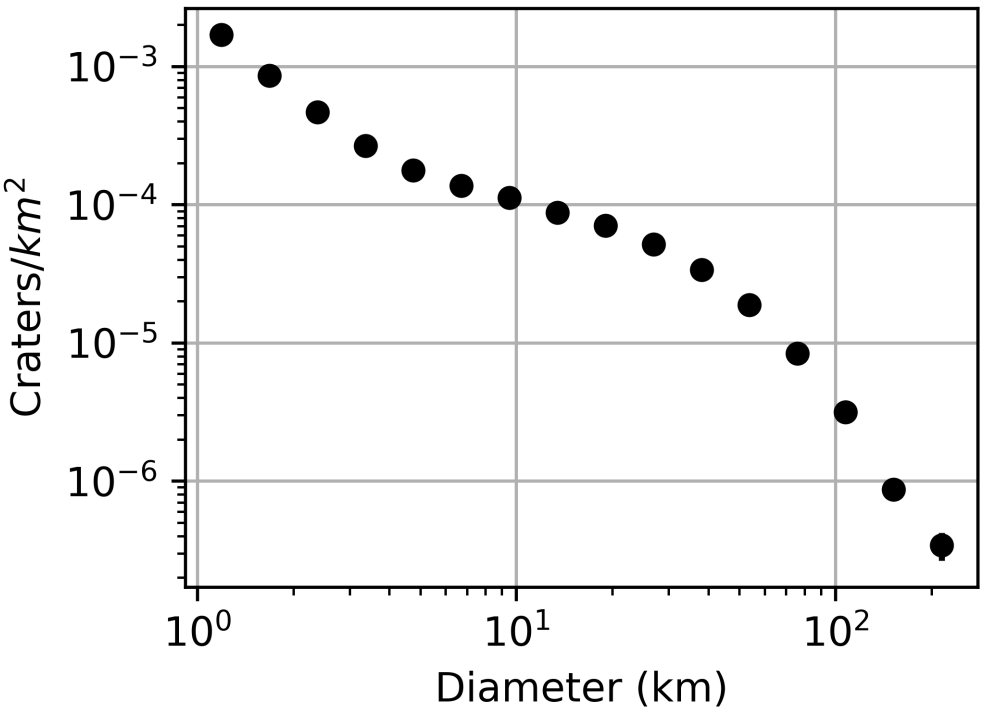

Figure 2.1: Noachian Crater Size-Frequency Distribution. Incremental crater size-frequency distribution ($2^{0.5}$-scaled bins, with 1σ error bars smaller than marker symbols) on the Noachian highlands between 0°N and 30°S latitude. Data from Robbins and Hynek (2012).

The incremental crater size-frequency distribution (CSFD) on the Noachian highlands exhibits a shallow slope in the 4–32 km diameter range, relative to the < 4 km and > 32 km ranges (Figure 2.1). This results in a paucity of craters $\lesssim 32$ km in diameter relative to extrapolation from isochron fits to larger craters (e.g. Irwin et al., 2013; Robbins et al., 2013). This lack of small craters has been observed for decades and is commonly interpreted as the

result of diameter-dependent crater obliteration by surface processes such as fluvial erosion, aeolian infilling, volcanic infilling, ejecta infilling, and diffusion (e.g. Öpik, 1966; Chapman and Jones, 1977; Craddock and Maxwell, 1990; Robbins et al., 2013; Quantin-Nataf et al., 2019). However, surface processes are not the only explanation for the lack of small craters. Specifically, the multi-sloped CSFD on the Noachian highlands is similar to that observed on the Lunar highlands and Mercury's heavily-cratered terrains, while single-sloped CSFD's in the $\sim$ 1-32 km diameter range are observed in young terrains across these planets (e.g. Barlow, 1988, Strom et al., 2005, Ćuk et al., 2010, Fassett et al., 2012, Strom et al., 2015). This suggests that the apparent paucity of craters $\lesssim$ 32 km in diameter on Noachian terrains could require a distinct inner-solar-system impactor population during the period of heavy bombardment $\gtrsim$ 3.8 Ga, with a subsequent shift to the modern impactor population and correspondingly single-sloped CSFD (Strom et al., 2005; Fassett et al., 2012; Strom et al., 2015).

These observations beg the questions: did obliteration by surface processes create the shallow-sloped portion of the Noachian CSFD? Can the shape of the Noachian CSFD be attributed to a changing impactor population? Are both required? In this work, we examine the compatibility of the Noachian crater record with each of these scenarios. In particular, we take advantage of statistical advances made by astronomers (e.g. Davis and Peebles, 1983, Bhavsar, 1990, Wall et al., 1993, Landy and Szalay, 1983) to robustly detect clustering of galaxies on the celestial sphere, and we apply their techniques to craters on the Noachian highlands. Assuming that crater obliteration processes are not spatially uniform (but that impact cratering is), our clustering analysis serves as a means of detecting crater obliteration on ancient geologic surfaces.

2.2 Geologic Datasets and Context

To investigate clustering of craters and resurfacing on Noachian highland terrains, we used two global datasets. The first is a global database of crater latitudes, longitudes, diameters, and degradation states (Robbins and Hynek, 2012). The second is a global geologic map of Mars (Tanaka et al., 2014). In this map, the Noachian highlands are divided into three main units (Figure 2.2): the early-Noachian highlands (eNh) that were mapped as heavily-cratered, high-standing, rugged, high-relief terrain; the middle-Noachian highlands (mNh) that were mapped as low-lying, often visibly layered, relatively smooth surfaces that make up most of the observable Noachian highlands; and the late-Noachian highlands (lNh) that were mapped as basin fill at topographic minima in the mNh/lNh (Irwin et al., 2013; Tanaka et al., 2014). The eNh unit retains a crater population > 32 km in diameter that is near saturation (Irwin et al., 2013), but the mNh and lNh retain lower crater densities for diameters > 16 km due to Noachian-era, gravity-dependent burial of large craters by some combination of volcanic, aeolian, and fluvial surface processes (Irwin et al., 2013). Further, the distribution of mapped geomorphic surfaces with distinct modification styles/processes (e.g. debris-mantled escarpments, regolith pediments, deposi- tional plains, and sloping aggradational surfaces) on the Noachian highlands was shown to be variable on $\sim 10^\circ$ angular scales (~ 600 km) (Cawley and Irwin, 2018). The observed spatial non-uniformity of Noachian surface processes motivates use of clustering as a detection of Noachian crater obliteration by erosion/burial.

Integration of these two datasets allowed us to restrict the global Robbins database (Robbins and Hynek, 2012) to craters lying on the eNh and mNh units in the Tanaka et al. (2014) map (Figure 2.2). Further, we restricted our dataset to craters ≥ 4 km in diameter to avoid potential database completeness issues (Stuart Robbins – personal communication) and to craters ≤ 32 km in diameter to avoid incorrectly assigning units to larger craters (many > 32 km diameter craters with centers on the mNh or lNh unit can be unambiguously assigned to older units via cross-cutting relationships; see Irwin et al., 2013). Finally, we restricted our dataset to latitudes -30° N to 0° N to avoid potentially confusing signals from

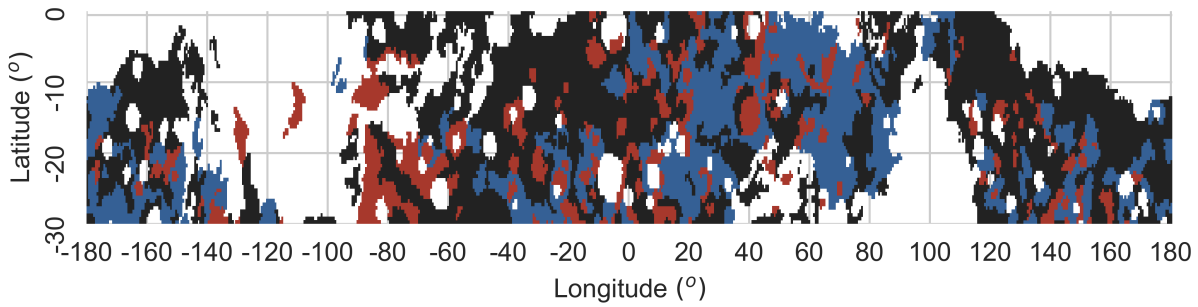

Figure 2.2: Map of Noachian Highland Terrains. $0.5° \times 0.5°$ resolution grid of latitudes and longitudes in our study area, colored by geologic unit according to Tanaka et al. (2014). Blue areas correspond to the eNh, black areas to the mNh, and red areas to the lNh. White areas represent post-Noachian materials or small Noachian massif units (Tanaka et al., 2014).

post-Noachian high-latitude modification (e.g. Kreslavsky and Head, 2018) and from the extensive resurfacing in Arabia Terra (Hynek and Phillips 2001). We did not restrict our dataset by longitude (Figure 2.2).

2.3 Methods

With our integrated dataset, we quantified crater clustering using the angular two-point correlation function, which has been typically used to quantify clustering of galaxies and test cosmological models (see Wall and Jenkins, 2012). The angular two-point correlation function, $w(\theta)$, is defined in terms of the incremental probability, dP, of finding two craters with separation θ in a solid angle element, $d\Omega$:

$$dP = \bar{R}(1 + w(\theta))d\Omega \tag{2.1}$$

where $\bar{R}$ is the probability of finding two points with separation θ in a randomly distributed dataset with the same mean density as our actual data. Thus, $w(\theta)$ can be thought of as a fractional enhancement (or depletion) factor of pairwise distances at a particular scale, relative to that expected for random points from a spatially-uniform distribution. Because $w(\theta)$ is estimated numerically by generating a random catalog of points (with no diameter

information) and comparing the pairwise distance distribution to that found in our dataset (see Appendix A.1), it is easy to incorporate the effects of geologic masking (i.e. by irregular count area geometry from mapped units in Tanaka et al., 2014) by applying the same masking to said random catalog.

To detect clustering on a particular angular scale, one must do more than just estimate $w(\theta)$ for a number of angular separation bins. In particular, $w(\theta)$ can be enhanced on small scales due to longer-wavelength density variations (see Bhavsar, 1990; Wall et al., 1993; Wall and Jenkins, 2012). Thus, the canonical method is to search for increasing $w(\theta)$ with decreasing angular scales by fitting a power-law to $w(\theta)$ and estimating the power-law slope in log-log space (Bhavsar, 1990; Wall et al., 1993; Wall and Jenkins, 2012). Note: we are fitting a power-law function within a limited domain, not a probability distribution subject to normalization constraints, so ordinary least squares regression in log-log space is appropriate. To assess the uncertainty in the slope estimate, one cannot assume any particular distribution structure to the errors, as they are both non-normal and correlated (e.g. Wall and Jenkins, 2012). However, the uncertainty is readily estimated by performing the computation many times, each time generating a new random catalog, and computing pairwise distance from a bootstrapped (resampled with replacement) version of the original dataset each time (Bhavsar, 1990). Examination of the histogram of slope values obtained allows one to determine how frequently the slope is < 0 and thus, how confident one is that a clustering signal exists (Wall et al., 1993). In this study, we demonstrate the application of this procedure to craters of different sizes, degradation states, and maximum ages to gain insight into resurfacing in the early and middle Noachian highlands.

2.4 Clustering of Noachian Craters

We binned our crater database by diameter (factor-of-2 width bins), geologic unit (we exclude the late Noachian highlands unit due to large uncertainties in calculated two-point correlations), and degradation state (grouping qualitatively determined preservation states

1 & 2 and 3 & 4 as "degraded" and "fresh," respectively). These qualitatively determined preservation states are described in more detail in Robbins and Hynek (2012). For each of these groupings, we estimated the angular two-point correlation function in 10 logarithmically-spaced separation bins between 2° and 30° (Figure 2.3; also see Appendices A.1 and A.2). Further, we computed 500 bootstrapped estimates of the corresponding power-law slope to determine to what extent craters on each unit, in a particular diameter range, experienced local to regional variations in crater obliteration (Figure 2.4).

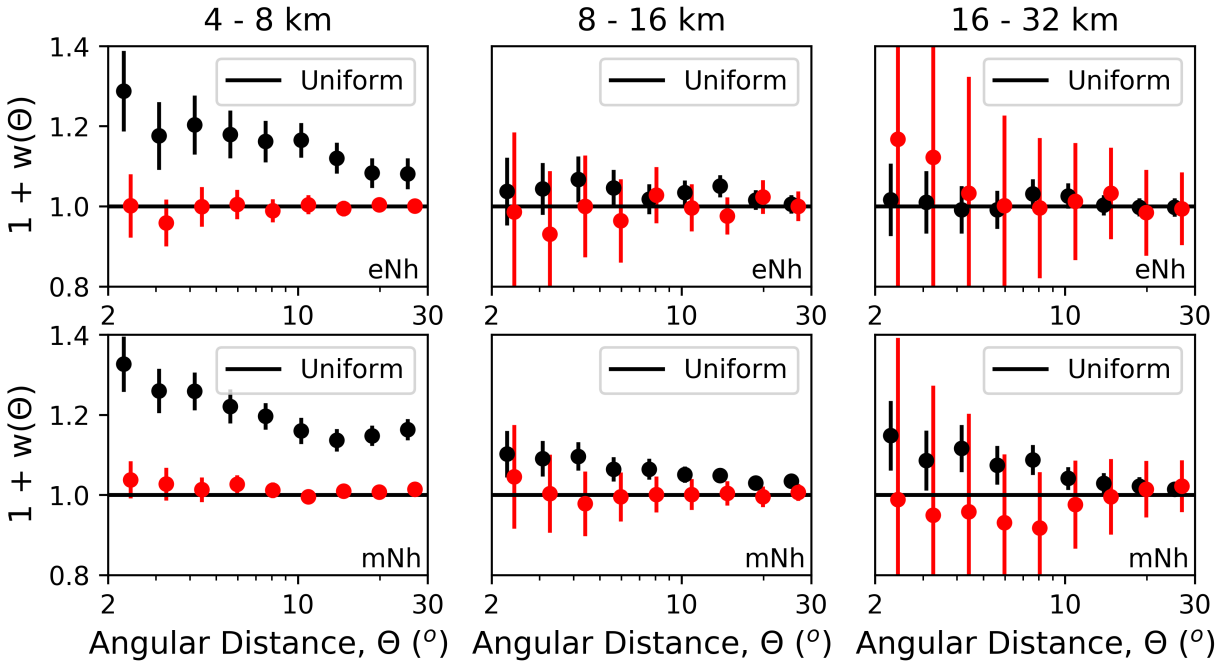

Figure 2.3: Two Point Correlation Function. Results from computation of the angular two-point correlation function for different diameter bins and geologic units (eNh-top row, mNh- bottom row). Fresh craters are shown in red, and degraded craters are shown in black. Error bars are one standard deviation, but recall that errors are non-normal and correlated.

We found that morphologically fresh craters have correlation power-law slopes that are consistent with 0, regardless of diameter or geologic unit (Figure 2.4). This indicates that, as expected, fresh craters are consistent with being randomly drawn from a spatially uniform distribution on the surveyed scales. On the early Noachian highlands unit ('eNh' in Tanaka et al., 2014), we found that degraded craters between 4 and 8 km in diameter show statistically

significant clustering (Figure 2.4), but that no such signal exists for degraded craters > 8 km in diameter (Figure 2.4). On the middle Noachian highlands unit ('mNh' in Tanaka et al., 2014), we found statistically significant clustering in each of the 4–8, 8–16, and 16–32 km diameter bins of degraded craters.

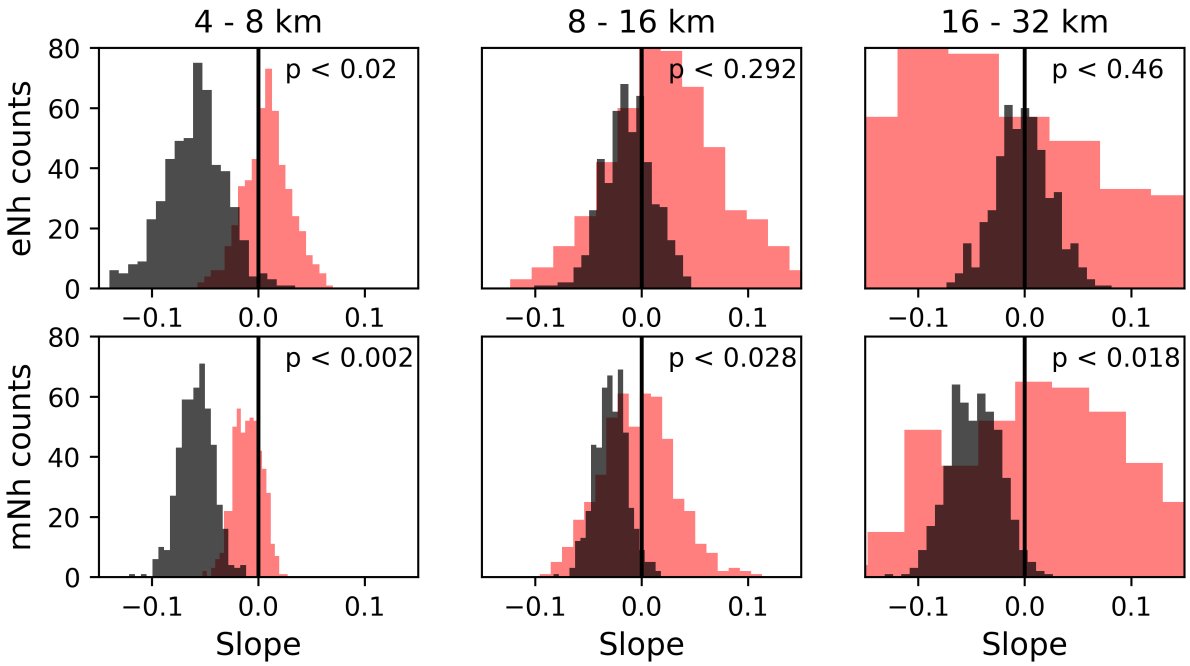

Figure 2.4: Two Point Correlation Function Power-Law Slopes. Histograms of bootstrapped best-fit power-law slopes for the angular two-point correlation function for different diameter bins and geologic units. Fresh craters are shown in red, and degraded craters are shown in black. All fresh craters are consistent with being drawn randomly from a spatially uniform distribution. p = significance level for degraded craters.

2.5 Implications for Ancient Resurfacing and Impactor Populations

As stated above, we assumed that impacts are spatially uniform but that crater-obliteration processes are not. Thus, from the geologic context of heavily degraded craters (e.g. Craddock and Maxwell, 1993), one may expect the observed clustering for degraded craters 4–8 km in diameter on both mNh and eNh terrains to be the result of spatially-patchy crater obliteration

by surface processes. While we favor this explanation, we note that the reference random catalogs for our two-point correlation function estimates contain no diameter/mutual occlusion information. As a result, it is at least in principle possible for clustering of craters to occur from obliteration by larger craters, or, "cookie-cutting" (Michael et al., 2012; Christian Riedel, personal communication). However, the cookie-cutting effect should increase in efficiency with overall crater density. Thus, we can attribute clustering of 8–32 km diameter degraded craters on the mNh unit to spatially-patchy obliteration and resurfacing processes. Our reasoning is as follows: if this clustering on the mNh unit did arise from cookie-cutting, then one would expect a clustering signal to be present for the 8–16 km bin on the eNh unit, which has a similar number of craters ($\sim$ 1000) as the 16–32 km bin on the larger mNh unit (and thus similar statistical power of the test), but greater overall density. However, this clustering signal is not observed. In addition, secondary craters may produce clustering signals (e.g. Riggs et al., 2015), but most secondary craters are too small to significantly affect our sampled populations (Robbins and Hynek, 2014).

We found that resurfacing of the mNh unit was spatially patchy on local-to-regional scales, not just on planetary length scales. This result is consistent with the study of Cawley and Irwin (2018). Further, because degraded craters > 8 km in diameter on the eNh unit are consistent with being drawn randomly from a spatially uniform distribution, we conclude that Noachian resurfacing processes on the local topographic highs comprising the unit (Irwin et al., 2013; Tanaka et al., 2014) were weak (relative to those on the mNh) and did not fully bury large craters. That the eNh has (a) craters in the 8–32 km that are consistent with being drawn randomly from a spatially uniform distribution and (b) a shallower sloping 8–32 km CSFD than does the mNh (Irwin et al., 2013), indicates that diameter-dependent obliteration alone cannot explain the shallow-sloped portion of the Noachian CSFD. Instead (or in addition), the data requires that the impactor SFD changed during the Noachian, perhaps due to planet migration (e.g. Barlow, 1988; Strom et al., 2005; Strom et al., 2015).

2.6 Discussion

We made use of the angular two-point correlation function as a means of detecting clustering of craters on a range of pre-specified scales. Other methods have been used to detect crater clustering, but these methods rely on nearest-neighbor statistics (e.g. Squyres et al., 1997; Kreslavsky, 2007; Michael et al., 2012; Kirchoff, 2017). Nearest-neighbor statistics detect clustering only on the scale of nearest-neighbors, which is itself dependent on point density (and can thus complicate comparisons of different crater diameter ranges). In contrast, the two-point correlation function preserves information from all scales, and our detection procedure is performed on a pre-specified range of scales (e.g. Wall and Jenkins, 2012; Riggs et al., 2015). Finally, the two-point correlation function is rigorously statistically defined, with well-understood errors and estimators (e.g. Wall and Jenkins, 2012), while nearest neighbor statistics are not (e.g. Riggs et al., 2015).

We combined mapped stratigraphic relationships, crater degradation classifications, and robust detection of crater clustering (via correlation function power-law slope determination) to draw conclusions about local to regional resurfacing on the Noachian highlands. In principle, because the angular two-point correlation function provides amplitude information (not just a binary detection output), it can provide higher-order information than what was utilized in this study. This has been done extensively by astronomers, who are able to explicitly model the two-point correlation function from the basic physics of the systems observed (e.g. Blake and Wall, 2002). However, the two-point correlation function does not preserve phase information and is less sensitive than power-spectrum analysis for larger angular scales (e.g. Wall and Jenkins, 2012). Thus, other metrics of clustering could be useful in unraveling global-scale resurfacing.

In our analysis, we assumed that detection of clustering served as a detection of obliteration by spatially-patchy surface processes (or even "cookie-cutting" of small craters by large impact craters). It is feasible that clustering could be observed due to real anisotropies in Mars' impactor flux (Le Feuvre and Wieczorek, 2008). However, on the measured scales of 2° to

30° density variations are expected to be small (Le Feuvre and Wieczorek, 2008). This is corroborated by the fact that fresh craters in the Noachian highlands are all consistent with being drawn randomly from a spatially uniform distribution (Figure 2.4). In addition, surface processes can in principle obliterate craters uniformly (e.g. resurfacing by planetary-scale impacts), but these are not likely relevant to Noachian-era resurfacing (Irwin et al., 2013; Cawley and Irwin, 2018).

Our work was partly motivated by recent studies that use the observed paucity of small craters on the Noachian highlands to infer the maximum depth of burial/erosion in various areas (Robbins et al.,2013; Quantin-Nataf et al., 2019). While our study does not invalidate their overall approach, it does invalidate the assumption that crater production functions (and thus the shape of fit isochrons) do not change in time. Further, our study provides evidence for a changing impactor population for Mars, but does not retrieve exactly how that population has changed as a function of time. As a result, revised determination of the maximum depth of burial on different terrains in the Noachian highlands is beyond the scope of this paper. We note that it is possible, in principle, that estimates of maximum burial/erosion depth that incorporate a changing production function will not significantly differ from previous estimates, but that estimates of typical burial/erosion depth (which should more strongly influence regional clustering) change drastically.

While our study supports the hypothesis that the population of objects bombarding pre-3.8 Ga Mars was different than the population of objects currently bombarding Mars post-3.8 Ga, the cause of this shift remains unknown. The hypothesis that giant planets migrated around 3.8 Ga (e.g. Strom et al., 2005) has been supplanted by the hypothesis that major shifts in the orbits of the giant planets occurred > 4.45 Ga (Morbidelli et al., 2018; Nesvorny et al., 2018). This is probably too old to explain our data. An incomplete list of processes that may have contributed to changes in the size-frequency distribution of Mars-crossing objects includes: collisional grinding within the asteroid belt (Bottke et al., 2005; Bottke and Morbidelli, 2017); tidal disruption of a Vesta-sized object (Ćuk et al., 2010); or

early size-agnostic sweep-up by Mars of an extension of the asteroid belt (Ćuk and Nesvorny, 2018).

2.7 Conclusions

Integration of a global database of craters (Robbins and Hynek, 2012) with globally mapped geologic units (Tanaka et al., 2014) enabled us to examine the first-order stratigraphic (i.e. geologic age) control on clustering (as measured by the angular two-point correlation function) of degraded Noachian highland craters. We found that low-lying, middle Noachian highland terrains experienced spatially varying rates of resurfacing and burial that produced clustering of > 8 km diameter craters on 2° to 30° angular scales. However, early Noachian craters are consistent with being drawn randomly from a spatially uniform distribution, implying shallow burial/erosion on the high-standing eNh unit (relative to the mNh). Our result supports the hypothesis that the multi- sloped CSFD on the Noachian highlands requires changes in crater production (e.g. Strom et al., 2005; Strom et al., 2015), rather than spatially-patchy destruction of craters alone (e.g. Öpik,1966; Chapman and Jones, 1977; Craddock and Maxwell, 1990; Robbins et al., 2013; Quantin-Nataf et al., 2019).

CHAPTER 3

MARS OBLIQUITY HISTORY CONSTRAINED BY ELLIPTIC CRATER ORIENTATIONS

Originally published as: Holo, S.J., Kite, E.S., and Robbins., S.J., Mars Obliquity History Constrained by Elliptic Crater Orientations, Earth and Planetary Science Letters, 2018. The research question addressed was conceived collaboratively by S.J.H and E.S.K. Elliptic crater data was provided by S.J.R. The study's design, execution, and writing were performed by S.J.H.

Abstract. The dynamics of Mars' obliquity are believed to be chaotic, and the historical ~ 3.5 Gyr (late-Hesperian onward) obliquity probability density function (PDF) is highly uncertain and cannot be inferred from direct simulation alone. Obliquity is also a strong control on post-Noachian Martian climate, enhancing the potential for equatorial ice/snow melting and runoff at high obliquities ($\gtrsim 40^\circ$) and enhancing the potential for desiccation of deep aquifers at low obliquities ($\lesssim 25^\circ$). We developed a new technique using the orientations of elliptical craters to constrain the true late-Hesperian-onward obliquity PDF. To do so, we developed a forward model of the effect of obliquity on elliptic crater orientations using ensembles of simulated Mars impactors and ~ 3.5 Gyr-long Mars obliquity simulations. In our model, the inclinations and speeds of Mars crossing objects bias the preferred orientation of elliptic craters, which are formed by low-angle impacts. Comparison of our simulation predictions with a validated database of elliptic crater orientations allowed us to invert for the best-fitting obliquity history. We found that since the onset of the late Hesperian, Mars' mean obliquity was likely low, between $\sim 10^\circ$ and $\sim 30^\circ$, and the fraction of time spent at high obliquities $> 40^\circ$ was likely $< 20\%$.

3.1 Introduction

Mars' obliquity, ϵ, is currently $\sim 25^\circ$ but has changed dramatically over billions of years since solar system formation (Ward, 1973; Touma and Wisdom, 1993; Laskar and Robutel, 1993; Laskar et al., 2004). The dynamics of Mars' obliquity are driven by secular spin-orbit resonances (Touma and Wisdom, 1993; Laskar and Robutel, 1993). However, the obliquity evolution is sensitive to orbital properties that vary chaotically on timescales < 100 Myr (Touma and Wisdom, 1993; Laskar and Robutel, 1993; Laskar et al., 2004). Many geologic methods have been proposed to vault the fundamental barrier of the chaotic diffusion of the Solar System (e.g. Ma et al., 2017; Kent et al., 2018), but all are indirect. Further, no more than a few transitions between low and high values of ϵ should occur (Section 3.3.1), preventing variations in obliquity from "averaging out" over billions of years. Thus, both the full obliquity history and the historical obliquity probability density function (PDF) are highly uncertain. Here we propose a direct method to constrain obliquity history.

Obliquity variations are a strong control on post-Noachian Martian climate (Jakosky and Carr, 1985; Laskar et al., 2004). At low obliquities ($\lesssim 25^\circ$) the Martian atmosphere is more likely to collapse at the poles (Kreslavsky and Head, 2005; Phillips et al., 2011; Soto et al., 2015) and H_2O surface melting is unlikely (Fastook et al., 2012). At high obliquities ($\gtrsim 40^\circ$) models predict that H_2O vapor pressure increases (Zent, 2013; Forget et al., 2017), H_2O surface melting is more likely (Jakosky and Carr, 1985), and strong dust storms initiate near the poles (Haberle et al., 2003). Insolation driven ice and snow melt has been proposed to explain observed sedimentary features near the equator (e.g. Kite et al., 2013; Irwin et al., 2015; Palucis et al., 2014). Further, low values of obliquity have been shown in models to dramatically enhance desiccation of deep aquifers via sublimation (Grimm et al., 2017).

To constrain the true effects of Mars' obliquity on post-Noachian climate, it is necessary to constrain the true obliquity history, and thus we sought a geologic constraint on Mars' obliquity history. Previous attempts to constrain Mars' obliquity from geologic features such as mid-latitude glaciers (e.g. Fassett et al., 2014) show that Mars' obliquity was high

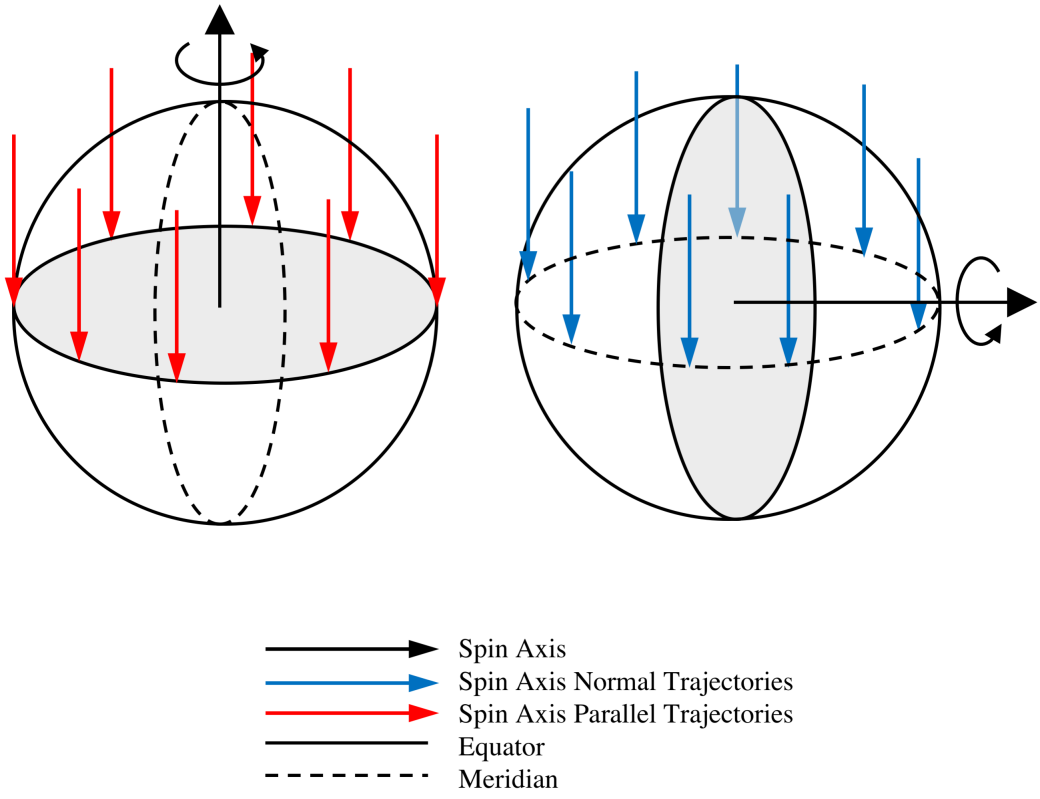

Figure 3.1: Obliquity Model Schematic. Schematic illustrating the basic principle in our model. Spin axis parallel impactors create N-S elliptic craters near the equator, while spin axis normal impactors produce elliptic craters that are E-W oriented at all latitudes except near the pole. The effects of gravity focusing are not shown here for simplicity.

($\sim 35°$) for ~ 1 Gyr. However, no study has quantitatively constrained the full ~ 3.5 Gyr post-Noachian Mars obliquity PDF with geologic evidence. Here, we propose a new method of constraining the historical Mars obliquity PDF using the orientations of elliptic craters. The vast majority of craters on Mars are nearly circular, but impactors with small impact angles relative to the surface produce elliptic craters with major axes aligned with impactor velocity vector (Bottke et al., 2000; Collins et al., 2011). As a result, impactors that travel parallel to Mars' spin pole will create North–South oriented craters at the equator, and impactors that travel normal to the spin pole will create elliptic craters at all latitudes that are East–West oriented everywhere except near the pole (Figure 3.1). As the obliquity changes, the angles between impactors and the spin axis change, causing a change in predicted orientation of elliptic craters. We developed a numerical forward model of the effect of obliquity on the

orientations of elliptic craters using realistic ensembles of simulated Martian impactor orbits and ~ 3.5 Gyr-long Martian obliquity simulations. We then used a validated version of a global database of Martian crater ellipticities and orientations (Robbins and Hynek, 2012; Appendix B.1.1) and the ages of underlying geologic units (Tanaka et al., 2014) to invert for the true Martian obliquity history. From that we construct estimates of the mean obliquity and the number of years with $\epsilon > 40^\circ$ (Figure 3.2).

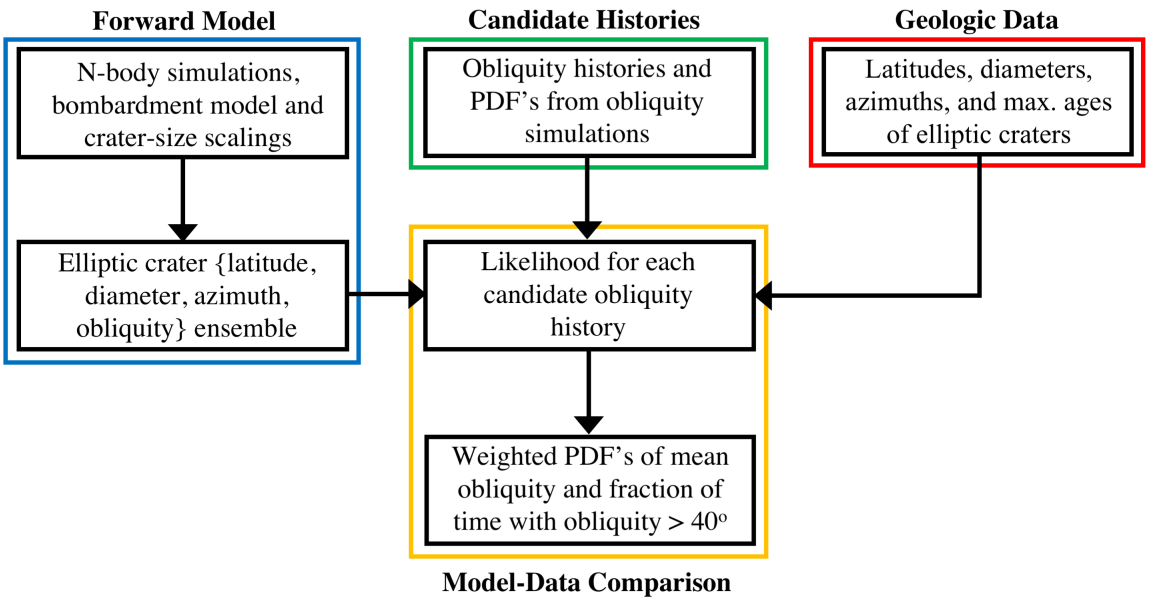

Figure 3.2: Model Workflow Schematic.

3.2 Elliptic Crater Orientations Database

The Robbins global Mars crater database (Robbins and Hynek, 2012) contains measurements of crater ellipticities (ratio of major to minor axes lengths) and major axis orientations (absolute azimuth from due North) obtained from fitting ellipses to points traced around crater rims. The publicly available data has a known bug in these parameters where some

major axis orientations have been shifted by 90°. While this error has been internally corrected (interested parties can obtain the corrected database from S.J.R.), there has been no independent check of the correction's accuracy. Thus, we carried out an exhaustive search for systematic inter-analyst variability (See Appendix B.1.1) and found that, restricting our analysis to craters > 4 km in diameter and degradation state ≥ 2 (i.e. filtering out the most degraded craters), inter-analyst residuals for both the ellipticity and orientation of craters are not systematically biased. Thus, we concluded that the Robbins database (Robbins and Hynek, 2012) provides a suitable constraint on our model with no systematic inter-analyst error and well quantified random inter-analyst error (Figure B.3).

Because our goal is ultimately to compare the population of elliptic crater orientations to predictions made by an ensemble of ~ 3.5 Gyr Mars obliquity simulations, we must filter out elliptic craters older than ~ 3.5 Gyr. Individual crater ages are difficult to constrain, but maximum crater ages are constrained by the age of the underlying geologic unit. Thus, we can use the Tanaka et al. (2014) global geologic map of Mars to identify the maximum ages of craters. Because not all of the geologic localities have well determined individual ages due to small surface areas, we rely on the reported geologic epoch of each locality. All terrains listed as Amazonian, early/middle/late Amazonian, Late Hesperian, and Amazonian–Hesperian were included in our analysis ($\sim 45\%$ of the Martian surface area). The maximum ages associated with each epoch are taken from Tanaka et al. (2014) assuming that the Amazonian–Hesperian units have a maximum age halfway through the late Hesperian. We bracket our uncertainty in absolute ages by using both the Hartmann and Neukum chronology ages as reported in Tanaka et al. (2014).

After filtering for maximum geologic ages, minimum diameter, and minimum preservation state, we are left with $N = 1502$ elliptic craters (crater data can be found in the Supplementary Files). Roughly 2/3 of these craters are found in the northern plains, while the remaining craters are found in the Tharsis region and other young volcanic and apron units in the Southern hemisphere (Figure 3.3, Tanaka et al., 2014). The craters possess a preference for

North–South oriented major axes that varies in strength with crater diameter and latitude (Figure 3.3). Integrated over diameter and latitude, the global preference for North–South vs. East–West oriented elliptic craters is roughly 3:2 (Figure 3.4).

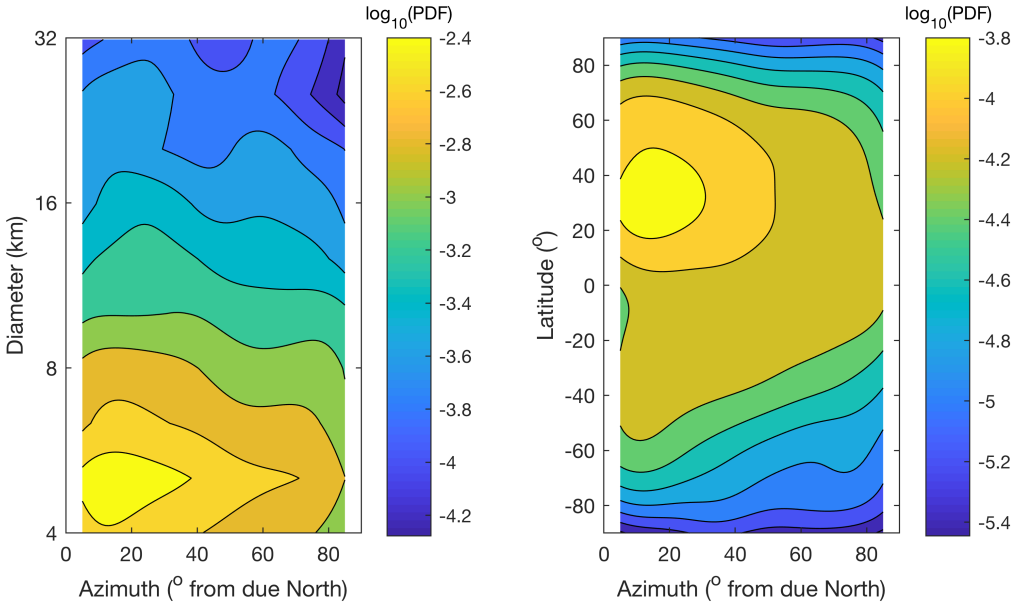

Figure 3.3: Elliptic Crater Orientation Data. Smoothed heat maps of crater diameter vs. major axis orientation (left) and latitude vs major axis orientation (right). Azimuth data has been trimmed below 5° and above 85° to eliminate artifacts of the smoothing kernel (bandwidth of 5° in azimuth). Diameters were smoothed in $\log_{10}$ space (bandwidth of .05).

To estimate our uncertainty in the major axis orientation PDF, we cannot use typical $\sqrt{N}$ estimates. This is because elliptic crater locations and the observed orientation distribution are a function of both impact processes and geologic masking due to erosion and resurfacing. Thus, the errors in our estimate are not necessarily random and are drawn from a distribution that is not well-described by a Poisson process. To overcome this barrier, we instead assume that the observed crater orientations represent a sample from some distribution with unknown shape. In this framework, we can take the observed crater orientations as a non-parametric estimate of the underlying distribution from which they are drawn and perform a procedure called bootstrapping (e.g. Robbins et al., 2018). The bootstrapping procedure involves re-sampling a population (usually taking the same number of samples as is in the original dataset) with replacement such that some values can be chosen multiple times. We computed

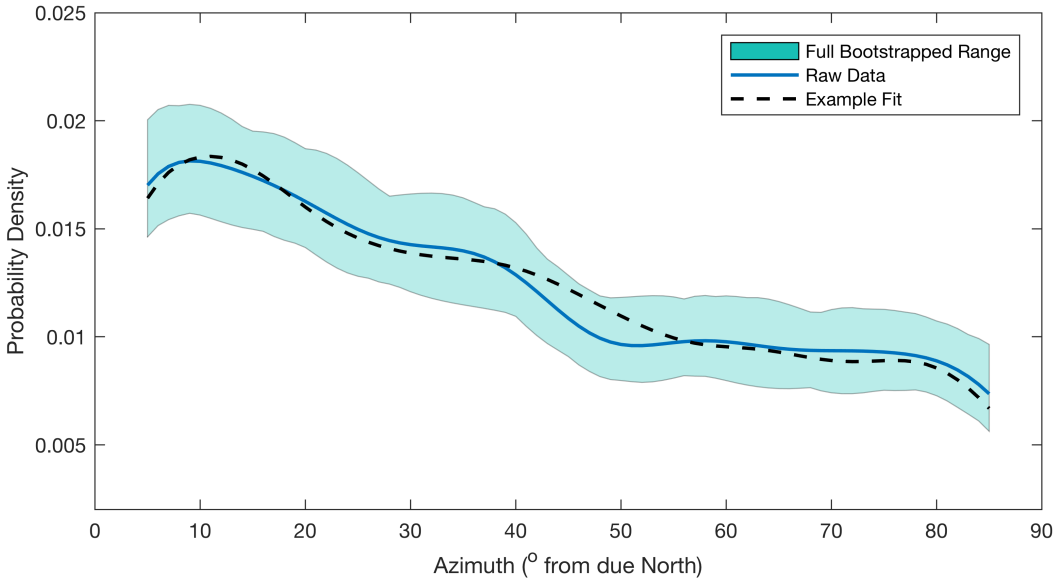

Figure 3.4: Elliptic Crater Orientation PDF and Model Best-Fit. Smoothed Gaussian kernel estimates of crater azimuth probability density (bandwidth of 5°). Azimuth data has been trimmed below 5° and above 85° to eliminate artifacts of the smoothing kernel. Example fit was chosen from the stochastic fitting scheme.

1000 bootstrapped re-samples of the data, and computed a kernel density estimate (bandwidth of 5° as measured in the data-validation process) of the resulting orientations. The envelope of possible orientation PDF's is shown in Figure 3.4.

3.3 Forward Model Description

We developed a forward model for the PDF of elliptic crater orientations on Mars that contains two major components: 1. An ensemble of possible Mars obliquity histories (Kite et al., 2015) and 2. a long-term cratering model that, using a forward N-body simulation, estimates the locations, sizes and orientations of elliptic impact craters as a function of obliquity. From this we can determine which obliquity histories are most likely to reproduce the observed elliptic crater orientations found in the now-vetted Robbins database (Robbins and Hynek, 2012). Our workflow is shown schematically in Figure 3.2.

3.3.1 Mars Obliquity History Ensemble

We generated an ensemble of forward integrations of Mars' obliquity to estimate the range of ~ 3.5 Gyr Mars obliquity PDF's (Kite et al., 2015). To do so, we computed 38 orbital trajectories for Mars using the `mercury6` N-Body code (Chambers, 1999). For each of these trajectories, the present day solar system with a small randomly generated offset in the position of Mars was taken as the initial condition. Each of these orbital trajectories was used to drive 24 instances of an obliquity code (Armstrong et al., 2004) where the initial obliquity was drawn from the PDF's of 3 Ga Martian obliquity reported by Laskar et al. (2004). In our simulations, Mars' obliquity undergoes only one-to-a few transitions between high and low values in ~ 3.5 Gyr, which is consistent with results for a moonless Earth (Lissauer et al., 2012; Li and Batygin, 2014). Further, Mars' obliquity exhibits $\sim 15^\circ$ peak-to-trough amplitude quasi-periodic non-chaotic oscillations on Myr timescales (Laskar et al., 2004). Thus, we restricted the $38 \times 24 = 912$ obliquity time series (with output every 1000 years) to the 250 that were both (a) stable (i.e. Mercury does not fall into the sun and the model run did not crash) for > 3.61 Gyr and (b) had a final Myr-mean obliquity between 10° and 40° (i.e. close to the modern value). This ensemble acts as a random sample from a large chaotic phase space of possible obliquity tracks. While none of these integrations is the true obliquity history, they represent a realistic distribution of obliquity PDF summary statistics. Thus, we used these 250 obliquity tracks to calculate estimates of the prior distribution (i.e. before considering the elliptic crater constraint) of the historical Martian mean obliquity and time spent with $\epsilon > 40^\circ$.

3.3.2 Cratering Model

In reality, Martian impactors come from all directions and with varying speeds. To estimate the Gyr-averaged impactor population on Mars, we assumed that the main asteroid populations are in steady state (Bottke et al., 2002) and that asteroids dominate the crater record (Bottke et al., 2000). With these assumptions, modern solar system impactors can be taken as

representative of solar system impactors in the last few Gyr. We initiated a 10 Myr modern solar system integration in `mercury6` with the modern Mars crossing objects (as reported by the Minor Planet Center in September 2016) as test particles and the planets as massive bodies. Mars crossers were defined as having perihelion distance less than $a(1+e)$ and aphelion distance greater than $a(1-e)$, where $a = 1.52$ AU is the semi-major axis of Mars and $e = 0.15$ was chosen to include the entire range of Mars eccentricities observed in our simulations (Figure 3.5). Instances of an object passing within one Hill radius of Mars were taken as a close encounter, and the relative velocity of each close encounter asteroid relative to Mars was stored. From this we calculated the encounter speed, v_∞, (magnitude of the relative velocity vector) and encounter inclination, i_∞, (angle between relative velocity vector and plane of Mars' orbit). Note that the effect of relative velocity causes objects to possess encounter inclinations much larger than their orbital inclinations. After a single close encounter, the asteroid was removed from the simulation (we confirmed that the total population of Mars crossers does not change significantly over the duration of our simulation). To ensure that our ensemble of close encounters is statistically complete and does not possess an inclination bias, we considered only bright objects with absolute magnitude $H \leq 14$ (Bottke et al., 2002). Following the completeness check of JeongAhn and Malhotra (2015), we confirmed that the absolute magnitude distributions for high and low inclination objects (with an orbital inclination cutoff of 15°) follow a power law for $H \leq 14$ and are indistinguishable via a two sample Kolmogorov–Smirnov test (p = 0.05). This procedure resulted in 124 total close encounters.

From this ensemble, we seeded a forward model (Figure 3.6; Appendix B.1.2) of crater locations, sizes, and orientations as a function of obliquity. We assume the impactor follows an angular-momentum-conserving hyperbolic orbit about the center of Mars (Le Feuvre and Wieczorek, 2008), and thus, for a given $\{i_\infty, v_\infty\}$, all impactors within a circular gravitational cross section with radius τ must impact the surface (Figure 3.6). To generate statistics on the long term predicted distribution of orientations as a function of location and size,

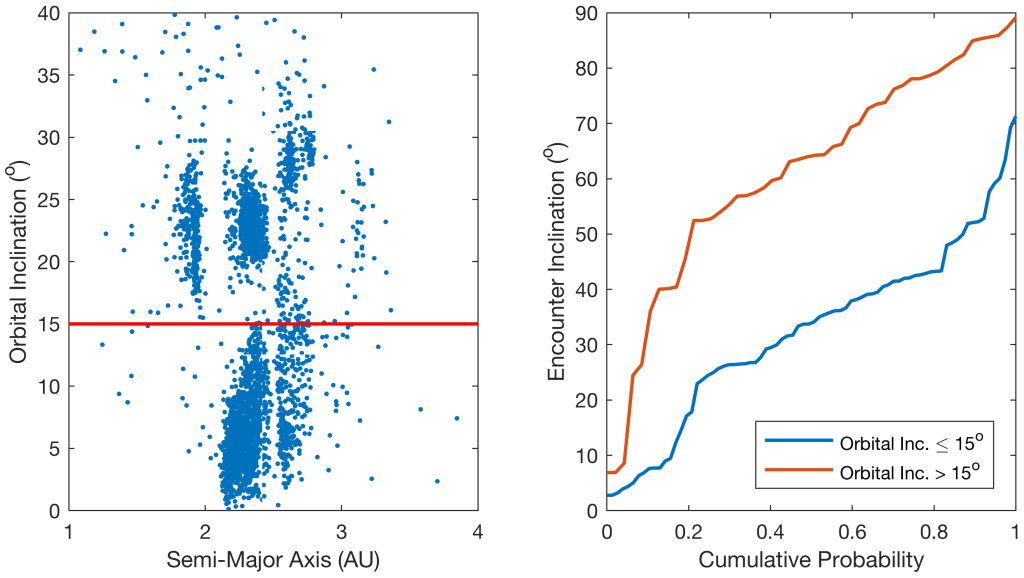

Figure 3.5: Orbital Statistics of Mars Crossing Objects. Scatter plot of orbital inclination vs. semi-major axis of potential Mars crossing objects. The red line separates what we refer to as high and low inclination objects. For absolute magnitude < 16, there are 3282 objects. Right: cumulative probability function of the encounter inclinations, upon entering Mars' Hill sphere, of the 124 objects with absolute magnitude ≤ 14 that experience a close encounter.

we generated 10^7 random samples from the encounter $\{i_\infty, v_\infty\}$ distribution obtained from the N-body simulations. For each sampled inclination-speed pair, we generate a random trajectory from a uniform distribution within the gravitational cross section (i.e. the square of the impact parameter b^2 is distributed uniformly in $[0, \tau^2]$, and the impact argument δ is distributed uniformly in $[0, 2\pi]$) and analytically solve for the velocity and position of the impactor at the time of impact, assuming that the spin pole precession angle (i.e. the angle between the axes of rotation for encounter inclination and obliquity in the model geometry) is uniformly distributed in $[0, 2\pi]$ (Le Feuvre and Wieczorek, 2008).

From this forward model we produced two {latitude, azimuth, impact velocity, obliquity, impact angle} ensembles: one with obliquity 0° and all impact angles (i.e. including circular craters), the other varying obliquity between 0° and 90° for impact angles less than the critical angle for elliptic crater formation (calculated using the scaling relation of Collins et al., 2011 that reports the critical impact angle as a function of cratering efficiency). We

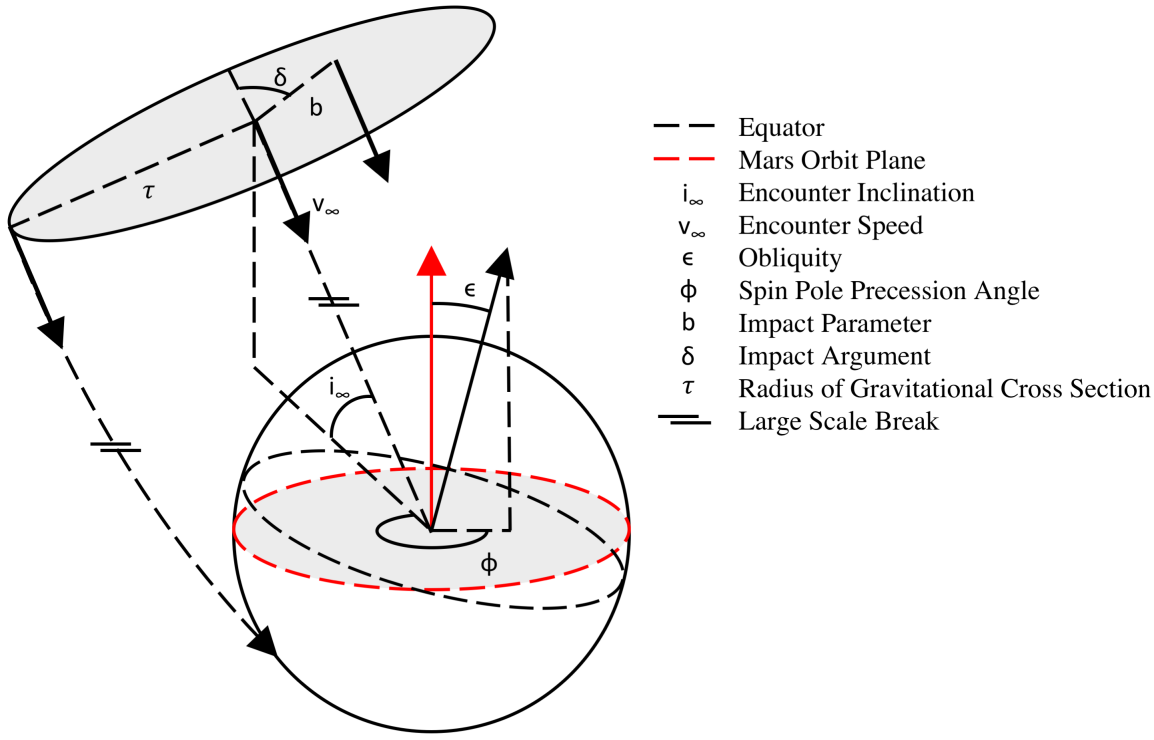

Figure 3.6: Impact Model Geometry Schematic

compared the first ensemble with the observed size frequency distribution (SFD) of craters between 4 and 32 km in the Robbins database (Robbins and Hynek, 2012) and tuned a single power law SFD for the impactors that, via a realistic crater diameter scaling (eq. (A7) in Collins et al., 2011, in which crater diameter depends positively on impactor speed), provides a best fit (minimized χ^2 statistic for $\sqrt{2}$-scaled bin widths results in power law slope of 1.5) to the observed SFD when convolved with the impact conditions. Our model fit and the data were found to be in close agreement. We then applied the tuned impactor SFD and crater diameter to the elliptic crater ensemble and produced a {latitude, azimuth, diameter, obliquity} ensemble. The ensembles shift from a North–South orientation preference at low obliquities to an East–West preference at high obliquities (Figure 3.7). This is largely due to the fact that, while there are roughly twice as many low-inclination close encounters as high-inclination ones, the high inclination objects have larger encounter speeds and thus

contribute more to the ≥ 4 km crater population (Collins et al., 2011).

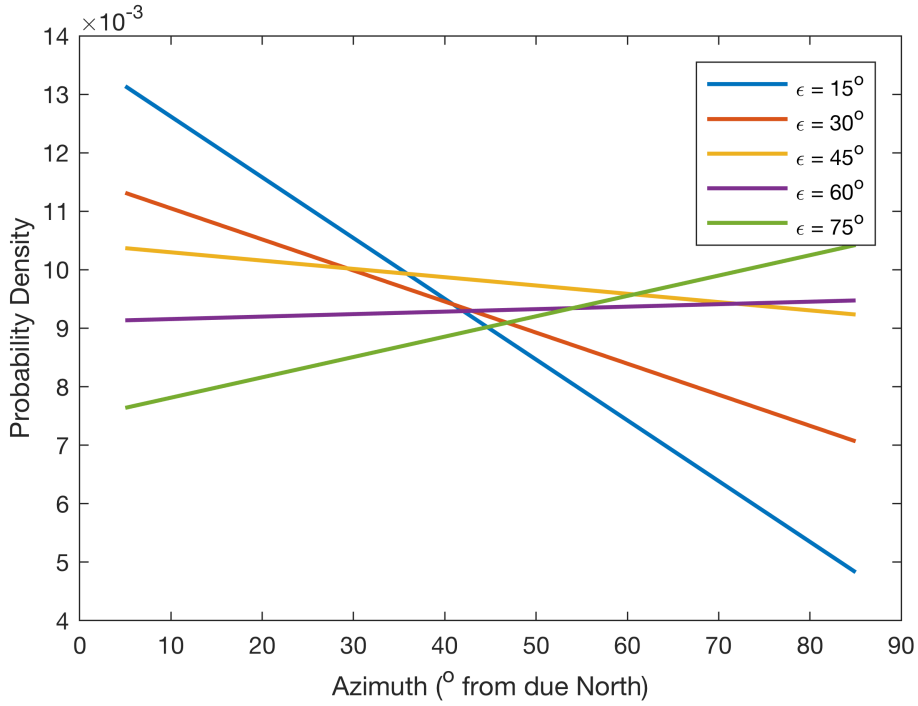

Figure 3.7: Single Obliquity Predictions. Gaussian kernel estimate of crater azimuth PDF (5° bandwidth) as a function of a single fixed obliquity prior to geologic correction. At low obliquities, there is a preference for North-South oriented elliptic craters. This trend is reversed at high obliquities. Azimuth data has been trimmed below 5° and above 85° to remove artifacts of the kernel smoothing process.

3.4 Model-Data Comparison

To compare our model outputs with the ~ 1500 observed elliptic craters, we must account for several factors. First, for a particular 3.5 Gyr obliquity PDF, the possible obliquities during the time of a crater's emplacement are constrained by that crater's maximum age. Second, for a given obliquity, our forward model ensemble represents the orientation preference of elliptic craters once the surface is essentially saturated with elliptic craters (recall there are $\sim 500,000$ elliptic craters in each single-obliquity ensemble). However, it is possible in principle that an obliquity PDF that produces an E–W preference after saturating the surface with elliptic craters could produce a N–S preference when only ~ 1500 craters are

selected. Finally, the orientation preference of elliptic craters is not independent of latitude or diameter, but, as discussed above, the latitude-diameter distribution of elliptic craters is largely a function of geologic resurfacing processes and does not have well-parameterized errors.

To overcome these difficulties, we developed a stochastic fitting algorithm that determines which candidate obliquity PDF's are most likely to reproduce the observed orientation preference given the selection of $\sim$ 1500 elliptic craters at the observed latitudes and diameters. For a particular candidate obliquity PDF, we take a bootstrapped re-sampling of the observed elliptic craters with the same number of craters as the original sample and assign random time stamps to each crater between the present and each crater's maximum age (from the geologic unit it lies on). This procedure assumes that the flux of craters has been constant between the late Hesperian and the present. We then, for each crater, randomly choose a crater from the model latitude, diameter, obliquity, azimuth ensemble with the constraints that the obliquity corresponds to the obliquity at the assigned time stamp (within 1 kyr), that the latitude is within 2.5° of the observed crater's latitude, and that the diameter is within 5% of the observed crater's diameter. This has the effect of both incorporating the maximum age constraint and approximately fixing the predicted latitude-diameter distribution to the observed distribution. Thus, the orientations from the ensemble-sampled model craters represent a crater orientation prediction for the chosen obliquity PDF.

We can then calculate a goodness-of-fit by calculating the two-sample Kolmogorov-Smirnov statistic between the bootstrapped re-sample of observed crater orientations and the predicted crater orientations. We repeat this process for each of our ensemble obliquity PDF's and determine which provides the best goodness-of-fit. This process is highly stochastic, and, as expected, obliquity PDF's which frequently produce poor fits can occasionally produce good fits. Thus, we repeat the entire process 1000 times and determine with what frequency each obliquity PDF provides the best fit (Figure 3.8). We can then weight each obliquity PDF by its relative best-fitting frequency to produce weighted PDF's of both the mean obliquity and

the fraction of time spent since the onset of the late Hesperian with obliquity $> 40°$(Figure 3.9). We repeat this entire analysis with both the Hartmann and Neukum chronology ages as reported in Tanaka et al. (2014) to account for our uncertainty in absolute ages.

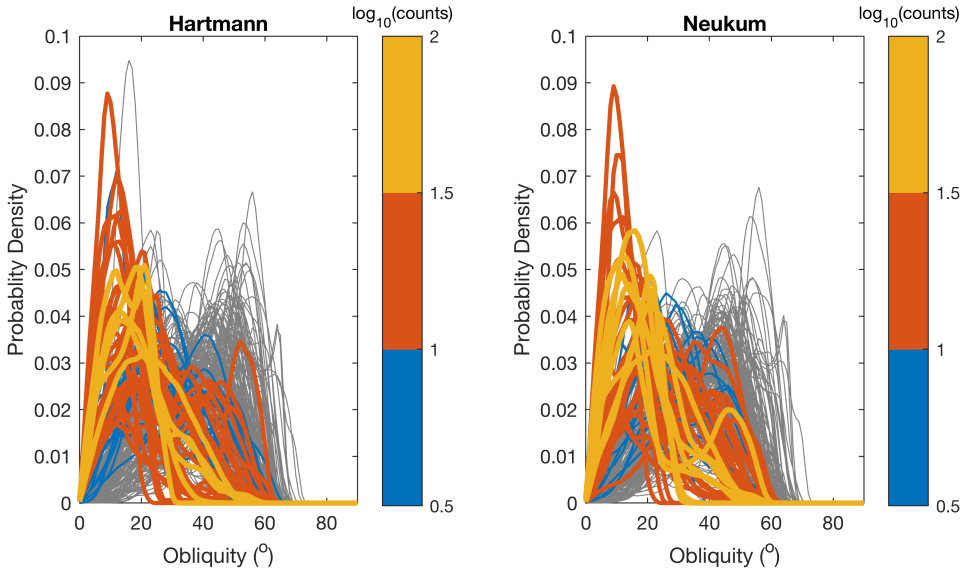

Figure 3.8: Obliquity History Likelihoods. All 250 obliquity PDF's in our ensemble, each colored by the number of times it provides the best fit to a bootstrapped sample of the data (tracks selected fewer than 3 times are shown in grey).

We found that Mars' mean obliquity from late Hesperian onwards was likely low, between $\sim 10°$ and $\sim 30°$, and we reject at the 95% confidence level that mean obliquity was greater than $\sim 33°$ (Figure 3.9). Applying the elliptic crater orientation constraint shifted this 95^{th} percentile upper bound from $\sim 44°$ in our unweighted mean obliquity PDF. Further, we found that the fraction of time spent since the onset of the late Hesperian with obliquity $> 40°$ was also likely low, $\lesssim 20\%$, and we reject at the 95% confidence level that this fraction was $\gtrsim 40\%$. This 95^{th} percentile upper bound shifted from $\sim 70\%$ in our unweighted PDF of fraction of time spent at high obliquities. Our inverted distributions for both mean obliquity and fraction of time spent at high obliquities indicate that the true values are likely lower than the central expectations from our obliquity history ensemble. We failed to reject low obliquity cases that have means of $\sim 10°$ and that spend $\lesssim 10\%$ of time at high obliquity.

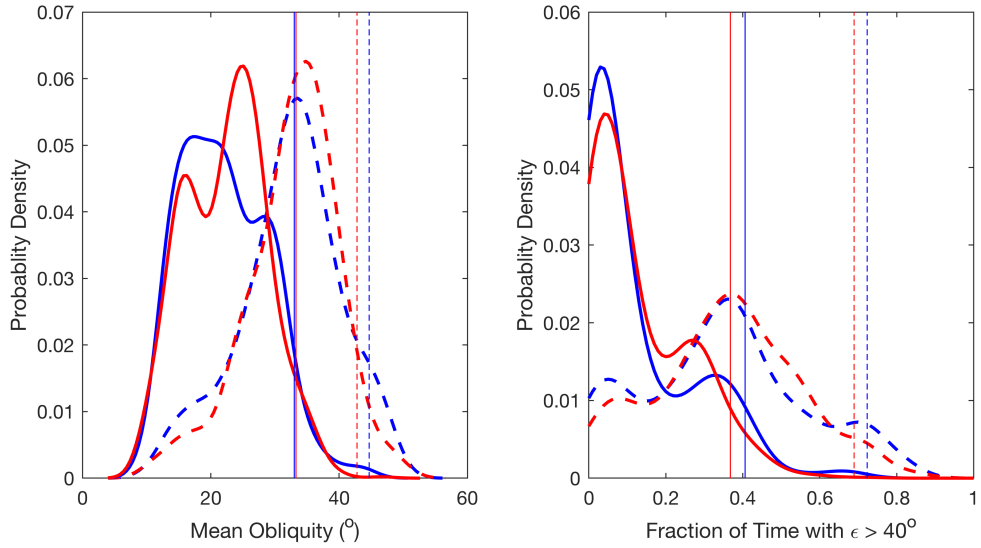

Figure 3.9: Revised Obliquity Summary Statistics PDF's. Gaussian kernel (bandwidth of 2° and 5% in the left and right plots respectively) smoothed PDF's of estimates of the mean obliquity (left) and fraction of the late Hesperian onward history spent at obliquity $> 40°$. Hartmann case estimates are in blue while Neukum case are in red. The dashed lines represent the obliquity history ensemble prior to model application, and the solid lines represent the bootstrapped retrieved value. Vertical lines show 95^{th} percentile locations.

3.5 Discussion

The model relies on the assumption that our simulated encounter inclination-speed ensemble is representative of 3.5 Gyr of Martian history and is unbiased. Increasing the relative abundance or speed of high inclination impactors biases the model to higher obliquity values. Conversely, increasing the abundance or speeds of low inclination impactors shifts the model output to lower obliquity values. However, the Martian impactor flux has likely been stable for over 3 Gyr (Nesvorny et al., 2017 and Robbins, 2014). In addition, we took a conservative cutoff in absolute magnitude of 14 for our impactors, which should be sufficient for preventing biases in the absence/presence of modern high inclination impactors (Bottke et al., 2002; JeongAhn and Malhotra, 2015). An additional source of potential inclination bias in our ensemble arises from the inclusion of high-inclination objects from the Hungaria region, the stability of which (and thus the 3 Gyr history of which) is still debated (Cuk and Nesvorny, 2017; Cuk, 2012; Bottke et al., 2012). However, of the close encounters, only one was an

asteroid sourced from the Hungaria region.

The model is also sensitive to the impactor SFD, as crater diameter scales with impactor diameter (Collins et al., 2011). Although the absolute magnitude cumulative distribution functions for high and low impactors are indistinguishable, there is a potential for an albedo bias in inclination that is offset by a bias in impactor size. We performed a sensitivity test and found that a 10% bias in albedo for high inclination objects biased the model by the equivalent of just a few degrees in obliquity. We concluded that the model can robustly reject high or low obliquity solutions even in the presence of a small albedo bias. Thus, while we suspect any biases that arise from sampling Hungaria derived objects or correlations between albedo, inclination, and speed are minor, this is an assumption that must be interpreted as a caveat for our work.

Uncertainty in the crater database is also responsible for uncertainty in the model inversions. In particular, the small number of craters (~ 1500) is responsible for uncertainties in the true strength of the North–South orientation preference (Figure 3.4). Inclusion of craters with much smaller diameters (soon possible with CTX imagery) would tighten the uncertainties in the true azimuth PDF and allow the model to more precisely constrain properties of the true obliquity history. We note that while we verified that inter-analyst error in ellipticity and azimuth measurements can be attributed to a random process, we did not account for other systematic errors that would affect all analysts (e.g. those that could be attributed to second order projection effects or lighting angles).

Geologic surface processes and crater collapse are in principle capable of modifying crater morphologies (e.g. Weiss and Head, 2015). However, it is unclear whether or not these processes actually produce elliptic craters with a systematic orientation bias. We repeated our analysis with a minimum ellipticity cut-off of 1.2, to test whether our conclusions change with the more conservative dataset. Overall, the results are consistent with our original analysis, supporting a low mean obliquity and $< 40\%$ of the late Hesperian onward time spent at high obliquity (Figure B.1), however, the 95^{th} percentile upper bounds shift to $\sim 40^{\circ}$

and $\sim 55\%$ for mean obliquity and high obliquity time fraction, respectively. We attribute these weaker upper bounds to the fact that only 276 craters meet the 1.2 ellipticity cutoff. As a result, our model-data comparison has a harder time distinguishing between acceptable obliquity PDF's (Figure B.2). Further, it is possible in principle that a thicker atmosphere in the late Hesperian may have biased the population of small elliptic craters, but we note that the global fraction of craters that are elliptic is the same for craters > 4 km in diameter and for craters > 10 km in diameter, which suggests that any such atmospheric filtering effect is negligible.

The model is unable to distinguish obliquity tracks that start low and end high from those that exhibit the opposite behavior. This is largely due to the small number of craters in Amazonian terrains, which possess an azimuth distribution indistinguishable from that of craters on late Hesperian units. In addition, the model selects different obliquity PDF's in the Hartmann and Neukum cases, but the systematic rejection of high obliquity solutions is common to both of them. This implies that our estimated upper bounds on the time spent above 40° and the mean obliquity are robust to uncertainties in age estimates from crater counts. However, we cannot say how much of the total time with $\epsilon > 40^\circ$ occurred in the Amazonian, as opposed to the late Hesperian.

In theory, the model could be applied to understanding the elliptic crater populations from earlier in Mars' history and also on other planetary bodies. However, application to early Mars history would require verification of ellipticity and orientation measurements of more degraded craters on Noachian terrain. In principle, models of late heavy bombardment impactors (e.g. Bottke and Norman, 2017; Nesvorny et al., 2017) could be tested by using Noachian crater orientations. Elliptic crater analysis also has the potential to test hypotheses of true polar wander early in Mars' history. For example, one could forward-model potential changes in true pole and compare the Noachian and post-Noachian crater orientations. We ignored any effects of true polar wander in our model as there is no definitive evidence of significant (more than a few degrees) true polar wander in the late Hesperian or onward

(Kite et al., 2009; Matsuyama and Manga, 2010; Scanlon et al., 2018). However, late stage true polar wander by more than a few degrees could affect the results presented here should definitive evidence for it be found.

3.6 Conclusions

We developed a forward model of the effect of obliquity on the distribution of elliptic crater major axis orientations. Using the model alongside the measured elliptic crater orientation distributions and an ensemble of obliquity histories, we obtained an estimate of the ~ 3.5 Gyr Martian obliquity PDF. We produced weighted estimates of the mean obliquity and compared them to unweighted estimates from our prior distribution of obliquity PDFs. Applying the elliptic-crater orientation constraint decreased the most probable mean obliquity from $\sim 33^\circ$ to between $\sim 10^\circ$ and $\sim 30^\circ$ and moved the 2σ upper bound on mean obliquity from $\sim 44^\circ$ to $\sim 33^\circ$. We also found that applying the geologic constraint reduces our weighted estimate of fraction of time spent above $\sim 40^\circ$ obliquity from $\sim 35\%$ to $\lesssim 20\%$ and moved the 2σ upper bound from $\sim 70\%$ to $\sim 40\%$. The exact values of these estimates are sensitive to the uncertainties in absolute dates of geologic units as well as deviations from a constant crater flux. However, they robustly decrease both the estimates of, and the upper bound on, the fraction of time after the onset of the late Hesperian spent with obliquity $> 40^\circ$. These results are consistent with findings from both Laskar et al. (2004) and Bills (2006). This updated upper bound may be useful when calculating the cumulative effects of obliquity on both insolation driven snow/ice melting (Kite et al., 2013; Irwin et al., 2015; Palucis et al., 2014) and rapid loss of atmospheric water (Grimm et al., 2017).

CHAPTER 4

TIMING THE FORMATION OF YOUNG ALLUVIAL FANS ON MARS

To be submitted as Holo, S.J., Kite, E.S., Morgan, A.M., and Wilson, S.A., Timing the Formation of Young Alluvial Fans on Mars. The research question addressed was conceived collaboratively by S.J.H and E.S.K. Alluvial fan global data was provided by A.M.M., and S.A.W. The study's design, execution, and writing were performed by S.J.H.

Abstract. The history of rivers on Mars is an important constraint on Martian climate evolution. The timing of relatively young, alluvial fan-forming rivers is especially important, as Mars' Amazonian atmosphere is thought to have been too thin to consistently support surface liquid water. Previous regional studies suggested that alluvial fans formed primarily between the Early Hesperian and the Early Amazonian. In this study, we describe how a hand-filtered global impact crater database, a global geologic map, a global alluvial fan database, and statistical models can be used to estimate the timing of alluvial fan formation globally. Using our global approach and improved statistical modeling, we found that alluvial fan formation likely persisted into the last $\sim$ 2.5 Gyr, well into the Amazonian period. However, the data we analyzed was insufficient to place constraints on the duration of alluvial fan formation. Going forward, more crater data will enable tighter constraints on the parameters estimated in our models and thus further inform our understanding of Mars' climate evolution.

4.1 Introduction

River deposits on Mars record past climatic conditions and thus serve as a proxy for Mars' climate evolution towards its current cold and dry state (e.g. Kite 2019). Since the end of the era of formation of regionally-integrated valley networks in the early Hesperian $\sim$ 3.4 Ga (Fassett and Head, 2008), fluvial activity on Mars primarily produced shorter landforms,

including small, 'pollywog', exit breach craters (Wilson et al., 2016; Warren et al., in press), alluvial fans (e.g. Figure 4.1; Moore and Howard, 2005; Kraal et al., 2008; Grant and Wilson 2011; Hauber et al. 2013; Kite et al. 2017a; Morgan and Wilson, 2019), and gullies (which may or may not be fluvial in origin; see Conway et al., 2018). The apparently recent ages of these fluvial features is at odds with the belief that intense atmospheric loss early in Mars' history would have rapidly rendered Mars' surface cold and dry (e.g. Kite et al., 2019). Further, Amazonian/Hesperian catastrophic floods (e.g. Baker and Milton, 1974) are commonly (but not exclusively) believed to require a > 1 km thick cryosphere (and thereby a cold climate) in order to over-pressurize the aquifers that fed these floods (e.g. Carr, 1979). Multiple mechanisms have been proposed to explain the late-forming rivers, including impact-induced snowmelt/precipitation (e.g. Williams and Malin, 2008; Mangold et al. 2012b), transient greenhouse atmospheres (e.g. Kite et al., 2017b), and obliquity-shift induced snowmelt/precipitation (e.g. Irwin et al. 2015). Each of these scenarios predicts transient excursions from an otherwise cold, dry climate state. Different proposed mechanisms have different dependencies on volcanism and/or $p\mathrm{CO}_2$, both of which declined over time (Fassett and Head, 2011). Thus, the timing of young fluvial activity is an important constraint on Martian climate evolution.

In this study, we focus on the alluvial fans (for the purposes of this study, we also include deltas, which are fans formed in standing bodies of water) and how improved statistical methodologies shed light on their formation ages. The alluvial fans are of particular interest because many are precipitation-fed (Kite et al. 2019), at least some fans formed over an extended time span ($>$ 20 - 200 Myr) (Kite et al. 2017b), and some are up to $\sim$ 1 km thick, recording a minimum of 100 years – 1 Myr of intermittent river flow (Irwin et al., 2015; Stucky de Quay et al., 2019). These observations require that at least some of the alluvial fans cannot be explained by localized impact trigger and therefore are more likely to provide true constraints on the Martian climate through time.

The primary method for estimating the absolute age of geologic surfaces on Mars is

through counting the craters in an area and comparing the observed density to a chronology function, which maps crater density to absolute age (e.g. Michael, 2013; Fassett, 2016). Existing estimates of alluvial fan absolute ages were determined using crater counts on the fan surface, averaged over numerous fans to reduce counting uncertainties (Moore and Howard, 2005; Grant and Wilson, 2011; Hauber et al., 2013; Morgan and Wilson, 2019). This methodology implicitly assumes that fan formation concluded simultaneously for each fan, such that their surfaces reflect a single age. This requires that there has not been sufficient, potentially spatially-varying, resurfacing of the fan surfaces to obscure any craters in the considered size range (Palucis et al., 2020). However, counting craters on small areas like fan surfaces requires counting small craters which are, by virtue of their size, more susceptible to survey complications like atmospheric filtering (e.g. Kite et al., 2014) and geologic modification (e.g. erosion, burial; Palucis et al. 2020). This methodology also sets aside the likely possibility that alluvial fans formed intermittently over tens or hundreds of Myr, rather than instantaneously (Kite et al. 2017b; Stucky de Quay et al., 2019). We propose that these shortcomings can be vaulted by a new approach involving careful consideration of the fans' cross-cutting relationships and choice of statistical modeling methodology.

The majority of alluvial fans are hosted on the interior walls of impact craters, where erosional backwasting of crater rims provides alluvium that is transported down-slope and deposited on crater floors (Morgan and Wilson 2019). These fans unambiguously post-date their host-craters, whereas determination of alluvial fan stratigraphic relationships within host crater interiors require more detailed investigation on an individual fan basis. Further, the ages of the impact craters can be estimated via crater counts on their ejecta deposits (where preserved), which provide us order-of-magnitude greater count areas (and thus the ability to count larger craters) than the fan surfaces themselves. In the following sections, we demonstrate how combining a global database of impact craters (Robbins and Hynek 2012), a global geologic map (Tanaka et al. 2014), a global database of alluvial fans (Morgan and Wilson 2019), and a novel statistical model can constrain alluvial fan formation timing to

have persisted until < 3 Ga. Further, we will discuss limitations of our approach and how updated datasets will affect fan-timing inferences.

4.2 Datasets and Methods

To investigate the formation of alluvial fans, we used a recently compiled global database (Morgan and Wilson, 2019). The Morgan and Wilson (2019) database contains fans from previously published compilations (Moore and Howard, 2005; Kraal et al., 2008), as well as newly-identified fans from a global survey of CTX imagery. Fans were identified as semi-conical deposits with adjacent source catchments. In the case of crater-hosted fans, source catchments are alcoves eroded into the bedrock of the host craters' walls and rims. Topographic analysis of fan profiles revealed that they all possess slopes $\lesssim 10^{\circ}$, well below the angle of repose (Morgan and Wilson, 2019). These observations indicate that the crater-hosted fans are likely fluvial in origin, not the result of dry ravel. The March 2020 version of this database used throughout this study (pre-publication dataset, shared with us by A. Morgan and S. Wilson) contains 1043 fans (substantially more than the 46 identified in previous surveys). Although the use of CTX imagery enabled surveying smaller fans than previous studies, we expect that the smallest features are censored from the survey, due to the finite resolution of the images used. For this study, we restricted the fans dataset to those contained within the 212 Amazonian-Hesperian Impact Units (AHi) from the Tanaka et al. (2014) global geologic map of Mars that are fully contained within 40° latitude of the equator (Figure 4.1). These units are impact craters that have well-preserved rims and ejecta (Tanaka et al. 2014). These AHi units provide us a sample of areas that are globally distributed spatially, share similar steep slopes and topography, and record their ages via crater-counts on their ejecta. Because fans on the crater walls must post-date the crater formation, ages obtained from the ejecta provide robust upper bounds on each fan's age. Further, not all AHi units possess fans (66 out of 212 units contain fans), which enables comparison between the formation times of fan-bearing and non-fan-bearing materials.

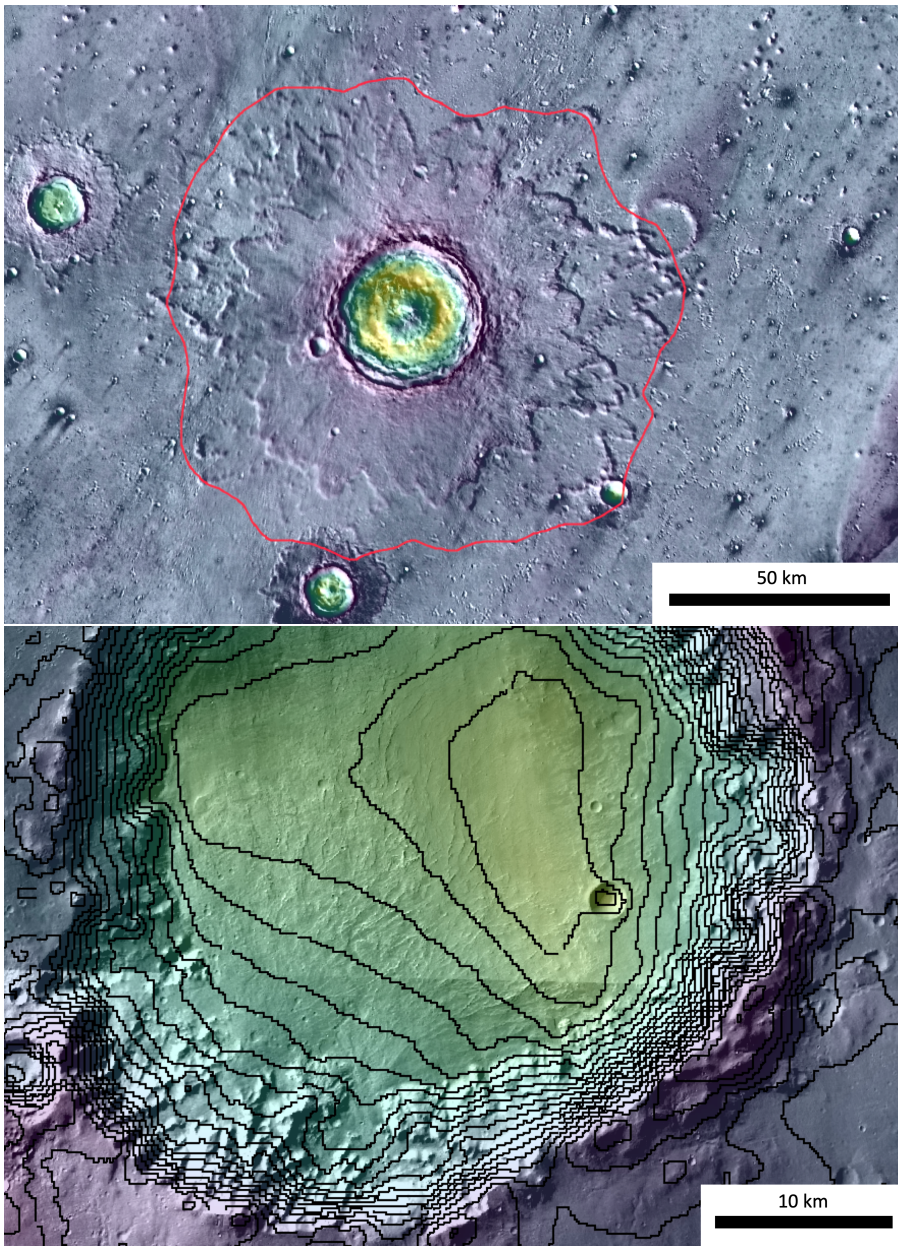

Figure 4.1: Comparison of Pristine and Fan-Bearing Craters (panels also appear in Figures 1.6 and 1.7). Top: HRSC/MOLA 200m colorized elevation over THEMIS daytime IR image of fresh impact crater (321° E, 26° N), with red outline around the ejecta as mapped in Tanaka et al. (2014). Note the preservation of the ejecta, rim, and central peak. Illumination is from SW to NE. Colorized elevation goes from yellow (elevation ~ -5 km) to indigo (elevation ~ -3 km). Bottom: HRSC/MOLA 200m colorized elevation over CTX Global Mosaic (Dickson et al., 2018) image of a large crater-hosted alluvial fan deposit, formed by erosional backwasting of the southwestern crater rim (333° E, 29° S). Contour spacing is 100m. Colorized elevation goes from green (low) to indigo (high). Illumination is approximately from NW to SE. North is towards the top of the page in both panels.

To obtain crater densities for each AHi unit's ejecta, we used a global database of impact craters > 1 km in diameter (Robbins and Hynek 2012). However, due to concerns over survey completeness for small craters (Stuart Robbins, personal communication), we restricted the dataset to craters with diameters of at least 4 km. Manual inspection of craters on the AHi units revealed three additional potential data quality issues. First, ejecta blankets often contain easily-identified chains of secondary craters. Second, some craters mapped on ejecta actually pre-date ejecta, as evidenced by cross-cutting relationships with the central crater's rim, impact ejecta, or secondary craters (Figure 4.2). Finally, craters in the interior of AHi units' central craters are often obscured from surveys due to resurfacing by burial/erosion.

To remedy these data issues, we manually inspected each crater in THEMIS and CTX and removed obvious secondary craters (elongated craters, often in chains extending from the center of large nearby craters) and craters that obviously pre-date crater ejecta based on cross-cutting relationships. In general, we were conservative and did not discard ambiguous craters, preventing us from erroneously under-estimating the age of the units. This procedure, along with removing craters within each AHi unit's central crater's interior, reduced our total crater count from 1768 to 1308. Further, we restricted our count areas on each AHi unit to the annulus extending from the crater rim to twice the unit-forming-crater's radius. In the $< 5\%$ of cases where the AHi unit is defined by the ejecta blankets of 2 large craters, we chose the larger crater as our nominal center. In many cases, the ejecta blankets do not extend to two times the crater radius, in which case we included in our count area only the intersection of the ejecta blanket and our defined annulus. We imposed the outer limit on our count area to accommodate the fact that craters "poking through" (pre-dating ejecta) near the ejecta edges cause densities to increase by a factor of $\sim 2 - 3$ (see Figure C.14) but that unambiguous cross-cutting relationships are increasingly difficult to identify as the ejecta thins radially outward. This indicates that the fraction of craters "poking-through" the ejecta increases near the edges. Thus, the outer limit prevents erroneously biasing our AHi unit ages upward. Imposing the outer limit reduced our total crater count to 498.

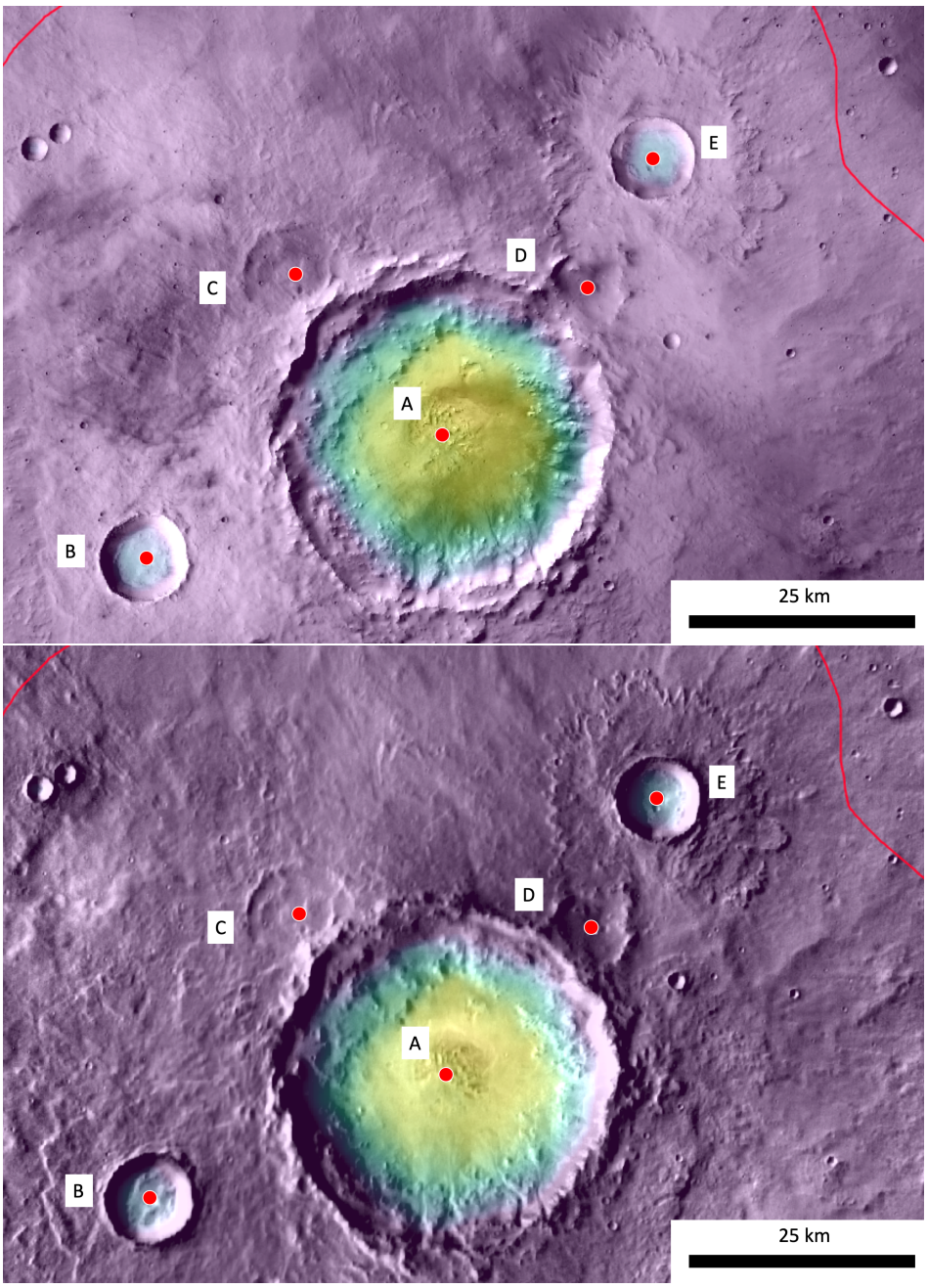

Figure 4.2: Example Ejecta Blanket Crater Counting. Top: HRSC/MOLA 200m colorized elevation over CTX Global Mosaic (Dickson et al., 2018) of an AHi unit (0° E, 15° S). Illumination is approximately from West to East. Bottom: HRSC/MOLA 200m colorized elevation over THEMIS daytime IR image of the same AHi unit. North is towards the top of the page in both images. In this example one can see that Craters C and D pre-date Crater A based on cross-cutting relationships with the Crater A's Northern rim and ejecta deposits. Crater E has well-preserved ejecta that cross-cuts the Crater A's ejecta, indicating that it post-dated the AHi unit formation. Crater B appears fresh and has ambiguous relationships with the terrain around it, so it was included in the count. Elevation ranges from ~ -1.8 km (yellow) to ~ 0 km (indigo).

4.3 Statistical Model and Results

Our goal was to take crater counts on the AHi units' ejecta blankets, note which units host alluvial fans, and make quantitative statements about the timing and duration of alluvial fan formation. We achieved this in two steps. First, we developed a probabilistic understanding of the age of each AHi unit by estimating their posterior age distributions in a Bayesian framework (similar to Michael et al. 2016). Second, we implemented two statistical models that represent hypothetical formation scenarios for the alluvial fans. Parameter estimation for these models enabled inferences about the timing of alluvial fan formation.

4.3.1 Dating the AHi Units

In 2016, Michael et al. described the use of Bayesian posteriors for estimating planetary surface ages, under the name "Poisson Timing Analysis." In this framework, crater counts were assumed to be generated as a Poisson process, with underlying parameter likelihoods, $\mathcal{L}$, given by the standard equation:

$$\mathcal{L}(t|k) = P(k|t) = \frac{(A\lambda_t)^k}{k!}e^{A\lambda_t} \tag{4.1}$$

where k is the observed number of craters, A is the area of the count region, and λ_t is the expected density of craters on a surface with age t. The correspondence between age and expected density is known as the chronology function, and throughout this chapter, we adopt the chronology function of Michael (2013) [based on Hartmann, 2005]:

$$\lambda_t(D) = C(D)[(3.79 \times 10^{-14})(e^{6.93t} - 1) + (5.84 \times 10^{-4})t] \tag{4.2}$$

where $\lambda_t(D)$ is the expected density of craters $> D$ km in diameter, and $C(D)$ is a function that accounts for the size-frequency distribution of craters (Table 1 in Michael 2013). If, a-priori, each candidate age is assumed to be equally likely, the likelihood function can

be normalized and treated as a posterior probability distribution for unit age. From there, Michael et al. (2016) computed median ages, as well as the 25% and 75% age percentiles. These corresponded to their final age estimates and error bounds, respectively.

In our framework, we had strong reason to believe a non-uniform prior in AHi unit formation age. In particular, impact fluxes on Mars were elevated > 3 Ga, relative to today (see among many others, Michael 2013). This implies that the AHi units, which are themselves formed by impact craters, are more likely to have formed early in Mars' history. Thus, for our application, we took the prior cumulative distribution function of AHi unit ages to be given by the chronology function, truncated at 4.5 Ga, and normalized to 1. We then expressed the prior distribution on AHi unit ages to be the derivative of the normalized chronology function (Michael 2013):

$$P(t) \propto \frac{d}{dt}[(3.79 \times 10^{-14})(e^{6.93t} - 1) + (5.84 \times 10^{-4})t] \tag{4.3}$$

Using the likelihood function and prior distribution, we computed posterior age distributions (Figure 4.3) by multiplying and normalizing:

$$P(t|k) \propto \mathcal{L}(t|k)P(t) \tag{4.4}$$

Our estimates are consistent with the method of Michael et al. (2016) in $\sim 90\%$ of cases (Figure 4.4). In every case, our strong prior forces our central estimate to be older than the central estimate from the Michael et al. (2016) method (Figure 4.4). Every AHi unit is consistent at the 5% confidence level with being Hesperian or Amazonian in age, however (considering only crater data and setting aside cross-cutting relationships) at least half of the AHi units are also consistent with being Noachian in age (e.g. Fassett, 2016).

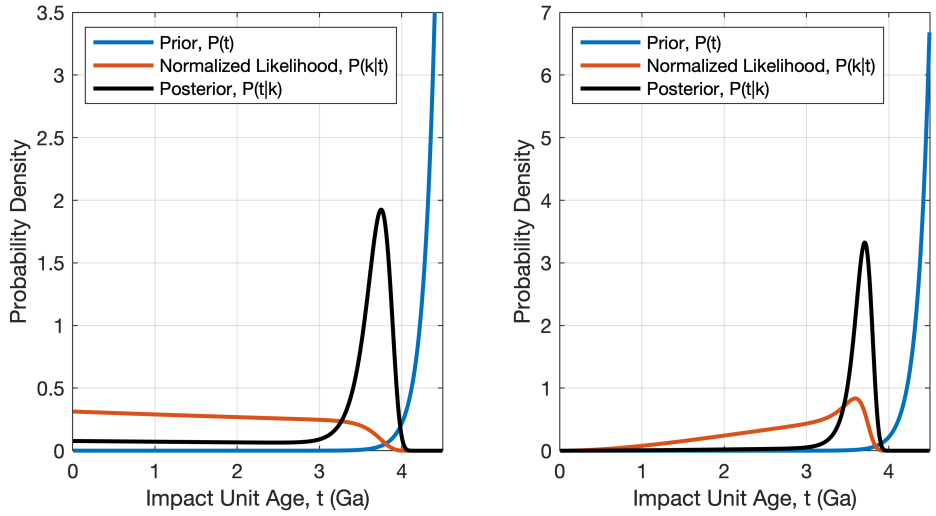

Figure 4.3: Unit Age Determination Examples. Two example likelihood and posterior distributions for the ages of AHi units. For the unit in the left panel, no craters were included in our retrieval (none $>$ 4 km in diameter were found within the count annulus), hence the maximum likelihood (red curve) of 0. For the unit in the right panel, two craters were included in the ejecta blanket crater count. Prior distributions are assumed to be the same for each AHi unit.

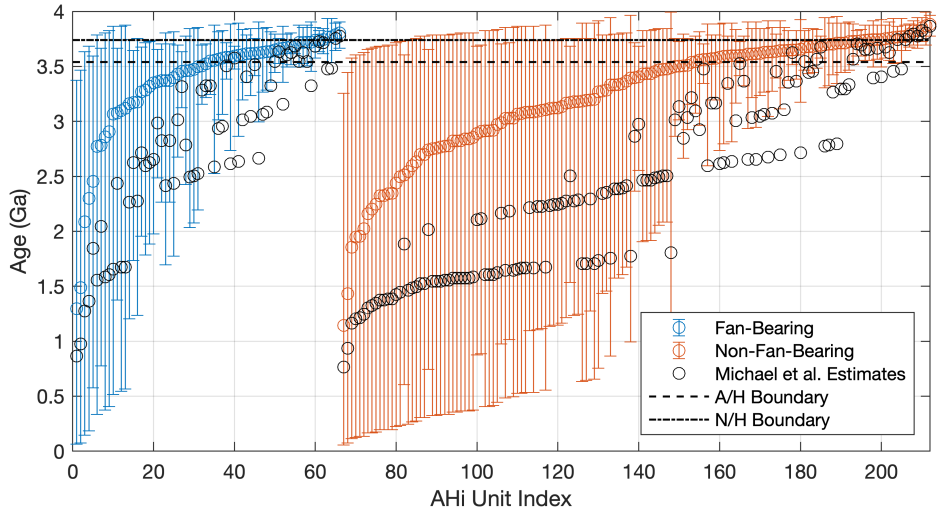

Figure 4.4: Individual Unit Age Estimates. Individual age estimates and 2σ error bars for each AHi unit using our Bayesian posterior method. Central estimates for our method are expected ages marginalized over age posterior distributions, while the Michael et al. (2016) method selects median values from the normalized likelihood function. Our strong prior systematically biases our age estimates upward, relative to Michael et al. (2016).

Using the posterior age distributions for each AHi unit, we derived cumulative distributions for the age of the youngest fan-bearing AHi unit. To do so, we assumed the ages of each AHi unit are independent random variables:

$$P(t_{min} \geq t_{ref}|t_{ref}) = \prod_i P(t_i \geq t_{ref}|k_i, t_{ref}) \tag{4.5}$$

where i is an arbitrary index over the fan-bearing AHi units. We computed this distribution for two populations: (a) all fan-bearing AHi units, and (b) those fan-bearing AHi units where localized impact trigger is excluded as an explanation for alluvial fan formation (Kite et al., 2017b; Kite et al., in review). The results are summarized in Figure 4.5. We found at the 95% confidence level that $t_{min} \leq\sim 1$ Ga if we include all fan-bearing AHi units. Considering only fan-bearing AHi units where localized impact trigger is excluded due to the identification of pre- or syn-fluvial impact craters within the fan-hosting crater (Kite et al., 2017b; Kite et al., in review), we found at the 95% confidence level that $t_{min} \leq\sim 2.5$ Ga.

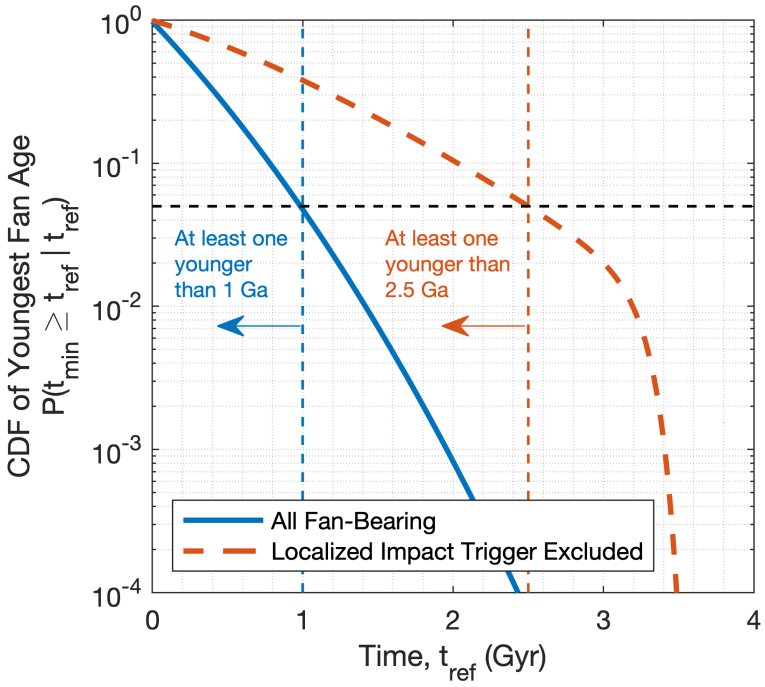

Figure 4.5: Youngest Fan Age CDF (see also Figures C.12 and C.13). Cumulative probability distributions (CDF's) for the age of the youngest alluvial fan, t_{min}, as a function of t_{ref}. Colors/dashes indicate the population considered, and vertical dashed lines indicated 5% confidence levels. Our results indicate that at least one fan occurred in the last 1 Gyr, and at least one fan where localized impact trigger is excluded formed in the last 2.5 Gyr.

4.3.2 Modeling Fan Formation Scenarios

To investigate the formation timing of alluvial fans in a way that incorporates information from crater-counts on non-fan-bearing AHi units, we developed two simple statistical models (Figure 4.6). In the simplest model (pulse-formation model), we assumed that alluvial fans formed at a single moment in history, τ_{form}, and that all AHi units with age $t_i \geq \tau_{form}$, had an equal probability, p_{max}, of acquiring alluvial fans. In the second model (prolonged-formation model), each AHi unit had a constant instantaneous probability, $p_{max}/\Delta\tau$, of acquiring alluvial fans during the $\Delta\tau$-long time period ending at τ_{end}. In both models, the probability of an AHi unit younger than τ_{end} or τ_{form} acquiring fans was assumed to be 0.

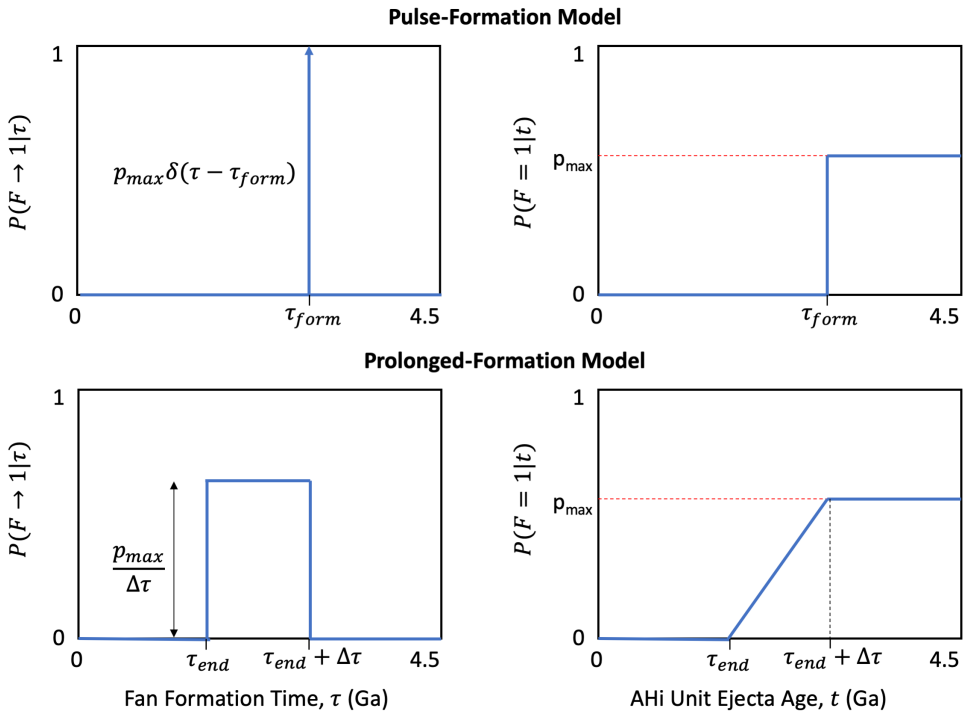

Figure 4.6: Alluvial Fan Formation Model Schematics. Schematic illustrating the two statistical models for fan formation. The pulse-formation model is on the top row and the prolonged-formation model on the bottom. The left column shows the instantaneous view, where the probability of an AHi unit acquiring alluvial fans, $P(F \rightarrow 1)$, is plotted as a function of time, τ. The right column shows the cumulative view, where the probability of an AHi unit having a fan, $P(F = 1|t)$, is shown as a function of AHi unit age, t. Figure is illustrative and not drawn to scale.

For both statistical models, the formation scenarios can be viewed both in an instantaneous framework (left panel, Figure 4.6), and in a cumulative framework (right panel, Figure 4.6). Both viewpoints are instructive, as the instantaneous view relates to a hypothetical climate scenario (e.g. short-lived, global transient greenhouse), while the cumulative view relates fan-acquisition probabilities to AHi unit ages, t_i. The relationship between these two views can be formalized mathematically via simple integrals for both models:

$$\mathcal{L}(\tau_{form}, p_{max}|F_i = 1, t_i) = \int_0^{t_i} P(F \rightarrow 1|\tau_{form}, p_{max}, \tau)d\tau \tag{4.6}$$

$$\mathcal{L}(\tau_{end}, \Delta\tau, p_{max}|F_i = 1, t_i) = \int_0^{t_i} P(F \rightarrow 1|\tau_{end}, \Delta\tau, p_{max}, \tau)d\tau \tag{4.7}$$

where $F_i = 1$ when the i^{th} AHi unit contains fans (0 otherwise), and $P(F \rightarrow 1)$ is the probability of acquiring fans, which varies with time (Figure 4.6). Note, because F_i is a binary variable, $P(F_i = 0) = 1 - P(F_i = 1)$, which defines $\mathcal{L}$ in the case that $F_i = 0$.

Because we only know the AHi unit ages, t_i, probabilistically, we computed expected likelihoods (instead of the likelihoods themselves) as a function of model parameters and crater density data by marginalizing over the age posterior distributions:

$$E(\mathcal{L}(\tau_{form}, p_{max}|F_i, t_i, A_i)) = \int_0^{4.5} \mathcal{L}(\tau_{form}, p_{max}|F_i, t)P(t|k_i, A_i)dt \tag{4.8}$$

$$E(\mathcal{L}(\tau_{end}, \Delta\tau, p_{max}|F_i, t_i, A_i)) = \int_0^{4.5} \mathcal{L}(\tau_{end}, \Delta\tau, p_{max}|F_i, t)P(t|k_i, A_i)dt \tag{4.9}$$

where k_i is the observed crater count and A_i the count region area for the i'th (out of 212) AHi units. Taking the data from every AHi unit together, we can multiply the expected likelihoods together to estimate the overall expected likelihood as a function of model parameters and data:

$$E(\mathcal{L}(\tau_{form}, p_{max}|\vec{F}, \vec{k}, \vec{A})) = \prod_i E(\mathcal{L}(\tau_{form}, p_{max}|F_i, t_i, A_i)) \tag{4.10}$$

$$E(\mathcal{L}(\tau_{end}, \Delta\tau, p_{max}|\vec{F}, \vec{k}, \vec{A})) = \prod_i E(\mathcal{L}(\tau_{end}, \Delta\tau, p_{max}|F_i, t_i, A_i)) \tag{4.11}$$

We computed the expected likelihood for the pulse-formation model as a function of τ_{form} and p_{max}, allowing them to vary in [0 Ga, 4 Ga] and [0,1], respectively (Figure 4.7). The model achieved maximum likelihood at $\tau_{form} = 1.8$ Ga and $p_{max} = 0.35$. Assuming a uniform prior over p_{max}, we marginalized the likelihoods over p_{max} to estimate a posterior distribution for τ_{form} (Figure 4.7). At the 95% confidence level, we found that in the pulse-formation scenario, the data requires fan formation to occur within the last ~ 3 Gyr.

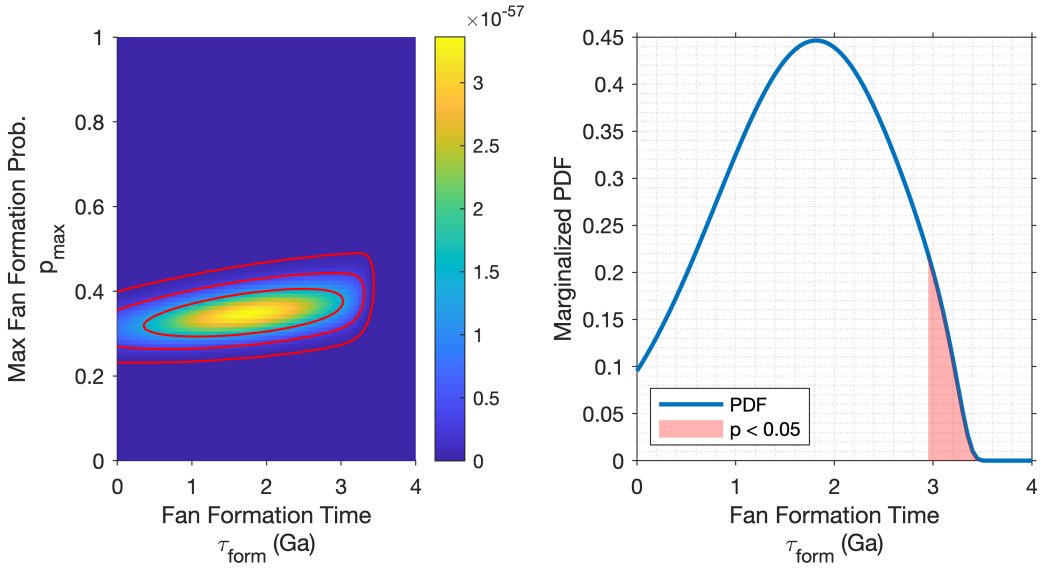

Figure 4.7: Pulse-Formation Model Results. Left: expected likelihood for the pulse-formation model, as a function of τ_{form} and p_{max}. Red contours show 1-, 2-, and 3-σ confidence regions (68, 95, and 99.7 percentile regions). Right: marginalized PDF for τ_{form}, assuming a uniform prior over p_{max}.

We computed the expected likelihood for the prolonged-formation model, as a function of τ_{end}, $\Delta\tau$, and p_{max}, allowing them to vary in [0 Ga, 4 Ga], [0, 4 Ga $-\tau_{end}$], and [0,1], respectively (Figure 4.8). The model achieves maximum likelihood at $\tau_{end} = 0.2$ Ga, $\Delta\tau = 3.1$ Ga, $p_{max} = 0.35$. Despite a maximum likelihood solution with $\Delta\tau > 0$, the difference in maximum likelihoods between the prolonged-formation model and the pulse-formation model (equivalent to the prolonged-formation model when $\Delta\tau = 0$) was not sufficiently large to reject the pulse-formation model via a likelihood-ratio test ($p < 0.75$, where our computed test statistic, $\lambda_{LR} \approx 0.1$, is given by twice the difference in the maximum log-likelihoods for each model and is asymptotically chi-square distributed with 1 degree of freedom). Assuming uniform priors, we marginalized the likelihoods over $\Delta\tau$ and p_{max} to estimate a posterior distribution for τ_{end} (Figure 4.8). At the 95% confidence level, we found that in the prolonged-formation scenario, our dataset requires fan formation to have persisted into the last ~ 2.4 Gyr.

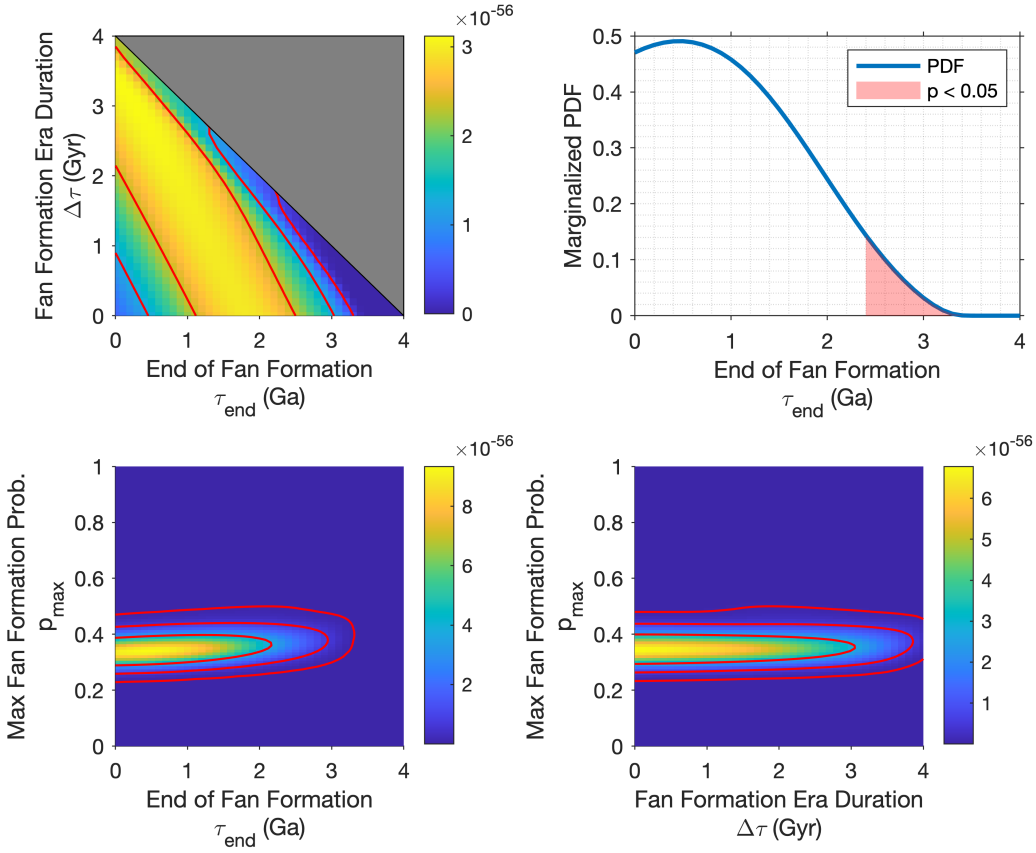

Figure 4.8: Prolonged-Formation Model Results. Top left: expected likelihood for the prolonged-formation model, as a function of τ_{end} and $\Delta\tau$, marginalizing over p_{max}. Greyed-out region was not modeled. Bottom left: expected likelihood for the prolonged-formation model, as a function of τ_{end} and p_{max}, marginalizing over $\Delta\tau$. Top right: estimated posterior distribution for τ_{end}, marginalizing over $\Delta\tau$ and p_{max}. Bottom right: expected likelihood for the prolonged-formation model, as a function of p_{max} and $\Delta\tau$, marginalizing over τ_{end}. Red contours show 1-, 2-, and 3- σ confidence regions in the marginalized, 2-D parameter spaces. Note, this is not equivalent to the projection of confidence regions in 3-D parameter space down to 2-D.

4.4 Discussion

Using the crater counts on AHi units' ejecta blankets, as well as some simple statistical models, we were able to place constraints on the timing of the formation of alluvial fans. Our estimate of the cumulative distribution (CDF) for the age of the youngest fan indicated that at least one fan likely formed by a process other than localized impact trigger in the last $\sim$ 2.5 Gyr. Further, our CDF estimate indicates that at least one fan likely formed in the last $\sim$ 1 Gyr. This is broadly consistent with the results from the pulse-formation model, in which the best-fitting time of fan formation was $\sim$ 1.8 Gyr. This indicates that fan formation likely persisted well into the Amazonian epoch (consistent with Palucis et al. 2020). Although the pulse-formation model does not favor formation occurring in the last 1 Gyr (due to the fact that very young values of τ_{form} force non-fan-bearing AHi units to take on likelihood $1 - p_{max}$ instead of 1 with too high a probability), it does not explicitly reject it. Further, at least some of the young fans can be explained by localized-impact trigger (e.g. Williams and Malin 2008), which is not permitted in the pulse-formation model scenario.

We estimated parameters for a more complex model, the prolonged-formation model, and compared the results with the pulse-formation model. The introduction of a third parameter introduced a large degeneracy between τ_{end} and $\Delta\tau$ in our parameter retrieval (Figure 4.8, top left). Although the model selected $\tau_{end} = 0.2$ Ga with fan-formation lasting several Gyr, a likelihood ratio test revealed that the maximum likelihood is not sufficiently higher in the prolonged-formation model than in the pulse-formation model to definitively justify the addition of the third-parameter. Thus we cannot reject either the pulse-formation or prolonged-formation model. Further, we do not have tight constraints on $\tau_{end} + \Delta\tau$, due to the degeneracy in our prolonged-formation model parameter retrieval. As a result, we cannot conclusively say, using this crater data alone, whether the alluvial fans formed in an era entirely separate from the valley networks (i.e. $\tau_{end} + \Delta\tau \lesssim 3.4$ Ga with high confidence), or if the alluvial fans represent a long-tail of continuous fluvial activity (i.e. $\tau_{end} + \Delta\tau \gtrsim 3.4$ Ga with high confidence).

For both models, we showed marginalized distributions for τ_{form} and τ_{end}, assuming uniform priors over the other parameters, p_{max} and $\Delta\tau$. Unlike the prior distributions for the ages of the AHi units, we had no particular reason to choose these parameter prior distributions. The marginalized distributions should thus be viewed only as condensed data visualizations, rather than true posterior distributions. Despite this, maximum likelihood estimates from both models indicate fan formation continued into the last ~ 2 Gyr. This global age is substantially ($\sim 1.5 - 2$ Gyr) younger than existing quantitative estimates of the age of fan formation from a regional study (Mangold et al. 2012a), which can be explained by the fact that our model allows for spatially patchy fan formation (i.e. $p_{max} < 1$), while the method of Mangold et al. (2012a) assumes uniform fan formation and thus would overestimate the young limit on alluvial fan formation if applied to our dataset. We note that the assumption that $p_{max} = 1$ may be perfectly acceptable within the Mangold et al. (2012a) study area.

In general, data availability limited our parameter retrievals for τ_{form} and τ_{end}, which had large uncertainties associated with them. Indeed, our crater counts were sparse due to our lower diameter cutoff of 4 km, causing our AHi unit age posteriors to be largely influenced by our choice of prior distribution and have high variance (Figures 4.3 and 4.4). We performed a series of sensitivity tests to illustrate how the model performs both with more data and with idealized data. First, we performed the parameter estimation with the same data, but with the outer annulus cutoff removed (Figure 4.9). This had the effect of biasing our retrievals to older ages due to the larger influence of old craters "poking-through" the ejecta blankets near the edges (Figure 4.9). Indeed, the pulse-formation model achieved maximum likelihood at $\tau_{form} = 2.25$ Ga and $p_{max} = 0.35$. Further, the increased quantity of data decreased the variance of our estimates, which is evident in the decreased degeneracy in the prolonged-formation model (Figure 4.9).

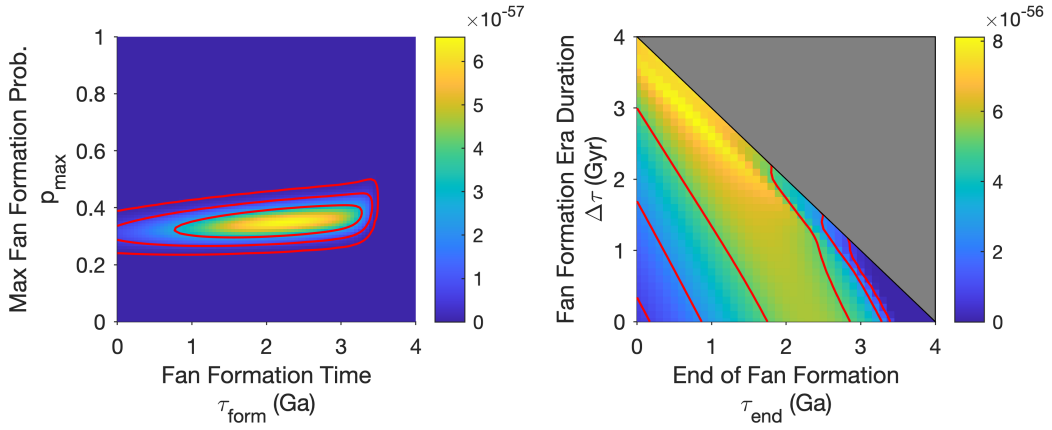

Figure 4.9: Extended Annulus Sensitivity Test. Model retrievals with the outer annulus limit of our count area removed. Left: expected likelihood for the pulse-formation model, as a function of τ_{form} and p_{max}. The results are biased to older ages relative to those in Figure 4.6, as expected given increased contamination by "poke-through" craters. Right: expected likelihood for the prolonged-formation model, as a function of τ_{end} and $\Delta\tau$, marginalizing over p_{max}. Greyed-out region was not modeled.Red contours show 1-, 2-, and 3- σ confidence regions in both panels.

Next, we performed the parameter retrievals using the original count areas (including outer annulus limit), using synthetic data where the alluvial fan flags (i.e. $F = 0$ or $F = 1$) and ejecta crater counts were randomly generated assuming that the pulse-formation model was true, that the fans formed at 1.5 Ga with probability 0.5, and that AHi units have ages drawn from the prior distribution, truncated at 4 Ga. In general, the model performs well and achieves maximum likelihood within 1σ of the correct value (Figures 4.10, C.1, and C.2). However, there is still substantial variance in the results, and the model is unable to substantially break the degeneracy between the end of fan formation and the duration of the fan formation era, although it does achieve maximum likelihood at $\tau_{end} = 2.1$ Ga, $p_{max} = 0.35$ and $\Delta\tau = 100$ Myr (Figure 4.10). We obtained similar results for synthetic data with a fan formation time of 3 Ga (Figures C.5, C.6, C.7). This suggests that more craters are needed to constrain the formation timing.

We repeated the experiment with synthetic data, artificially increasing the AHi count areas by a factor of 10. This had the effect of placing roughly 10 times as many craters on each unit, thereby decreasing the uncertainty in the posterior age distributions. As a result, the

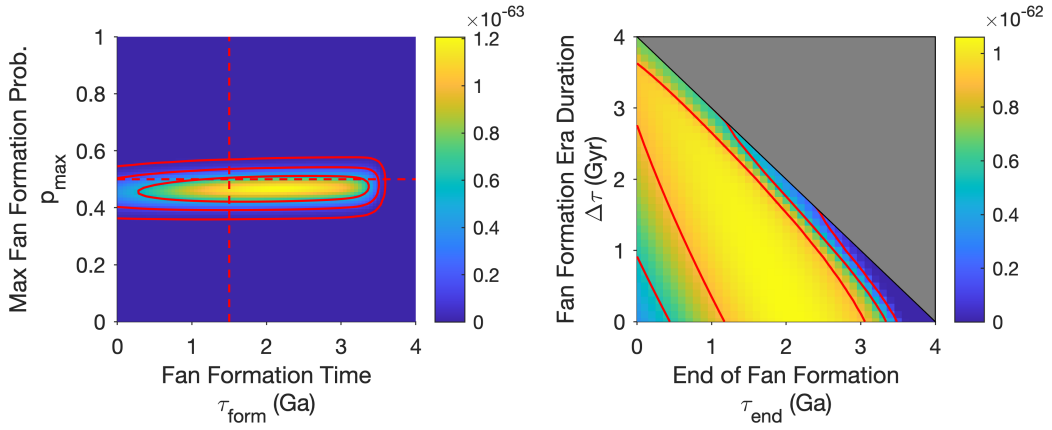

Figure 4.10: Synthetic Data Check. Model retrievals where synthetic data was created assuming the pulse-formation model is correct (i.e. $\Delta\tau = 0$). Left: expected likelihood for the pulse-formation model, as a function of τ_{form} and p_{max}. Dashed red lines show true parameters from the synthetic data generation process. Right: expected likelihood for the prolonged-formation model, as a function of τ_{end} and $\Delta\tau$, marginalizing over p_{max}. Greyed-out region was not modeled. Red contours show 1-, 2-, and 3-σ confidence regions in both panels.

variance in our parameter retrievals shrunk (compare Figure 4.11 with Figure 4.10). Further, the parameter retrieval has a slightly increased ability to discriminate between the prolonged- and pulse-formation models (relative to the synthetic data experiment with uninflated AHi unit areas) and preferentially selects a fan formation era duration of 0 (Figures 4.11, C.3, and C.4). This indicates that in order to obtain better estimates for the timing and duration of alluvial fan formation, one needs substantially more data and must consider craters at smaller diameters (recall our lower cutoff was 4 km). Although we ignored the possibility that surface processes efficiently obliterated 4 km diameter craters in the post-Noachian, one must correct for crater obliteration to avoid underestimating age when smaller craters are considered (e.g. Palucis et al., 2020).

In our methodology, we did not account for uncertainty in the chronology function, which is continually being re-evaluated from a combination of crater counting, geochronology, and solar system dynamics perspectives (e.g. Robbins et al., 2014; Farley et. al 2014; Marchi, 2020). It is certainly possible that all of our age estimates are systematically younger or older than the true ages, which would have biased our fan formation timing estimates. This potential effect

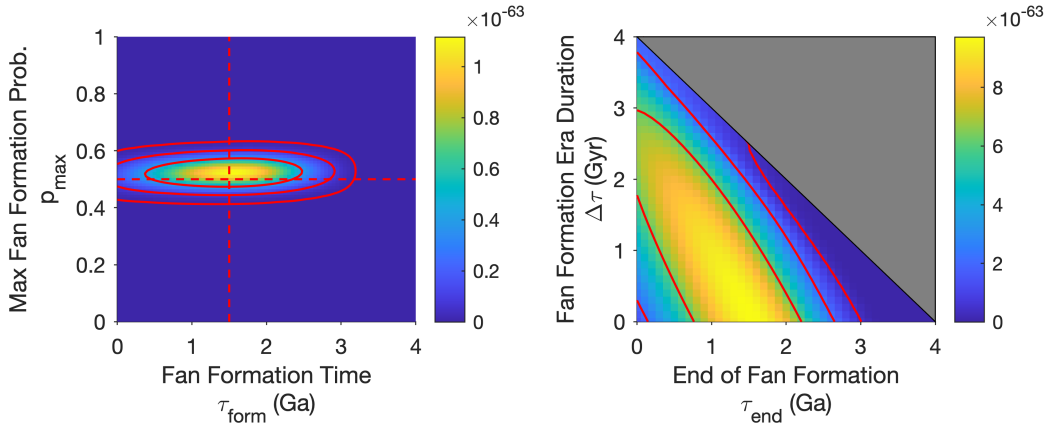

Figure 4.11: Synthetic Data Check with Inflated Count Areas. Model retrievals where synthetic data was created assuming the pulse-formation model is correct (i.e. $\Delta\tau = 0$) and inflating the count area by a factor of 10. Left: expected likelihood for the pulse-formation model, as a function of τ_{form} and p_{max}. Dashed red lines show true parameters from the synthetic data generation process. Right: expected likelihood for the prolonged-formation model, as a function of τ_{end} and $\Delta\tau$, marginalizing over p_{max}. Greyed-out region was not modeled. Inflating the count area had the effect of decreasing the variance in our estimates. Red contours show 1-, 2-, and 3-σ confidence regions in both panels.

is especially important in the data-limited case, where the prior strongly informs posterior age distributions (e.g. if there were ample data, the posterior curves in Figure 4.3 would coincide with the normalized likelihood curves). Further, we assumed a maximum age of 4.5 Ga in our prior age distribution. In principle, one could impose a younger maximum age based on stratigraphy to obtain tighter constraints. We re-performed our parameter retrieval assuming a maximum age of 3.54 Ga (approximately the Noachian/Hesperian boundary; see Figures C.9, C.10, and C.11). However, roughly half of the AHi units achieved maximum posterior probability at 3.54 Ga (Figure C.8), indicating that this prior was too restrictive given the data we had. It is possible that with improved crater surveys, the data would produce maximum a-posteriori ages that are well into the Amazonian.

Finally, we did not account for the possibility that the survey of fans suffers from incompleteness. It is possible that some fans were wrongly identified and that other fans were missed in certain craters in the survey. To explore this effect, we performed a sensitivity test where the probability of an AHi unit acquiring fans after the end of fan formation (or

after the pulse of fan formation) was 0.001, instead of 0. This had a negligible effect on the outcome, and we concluded that survey incompleteness needs to be more severe (e.g. a 10% chance of missing all the fans in a crater) to substantially alter the results. We note that our database of fans is a pre-publication dataset (Morgan and Wilson, 2019) and only reflects surveys completed by March 16^{th}, 2020. As a result, updated fan surveys may alter our inferences.

4.5 Conclusions

We combined a global geologic map (Tanaka et al., 2014), a global database of Martian impact craters (Robbins and Hynek, 2012), a global database of alluvial fans (Morgan and Wilson, 2019), and statistical models to make inferences about the timing and duration of alluvial fan formation. Although differing in detail due to differing assumptions, the results of all our models suggest that fan formation had to have persisted into the last ~ 2.5 Gyr (based on our most conservative estimate, see Figure 4.5), well into the Amazonian time period. Overall, our modeling procedure was not able to constrain the duration of fan formation. As a result, we were unable to determine from this dataset whether the alluvial fans formed in an era entirely separate from the valley networks, or if the alluvial fans represent a long-tail of continuous fluvial activity.

In general, our inferences were limited by a lack of crater count data, and our tests with synthetic data suggest that detailed surveys of smaller craters on AHi unit ejecta blankets will enable much tighter constraints on fan formation. Going forward, we hypothesize that more data and more complex statistical models (i.e. ones with more parameters) for the population of alluvial fans (or other geomorphic features) will enable determination of both (a) their joint temporal and spatial evolution and (b) the relative importance of climate-triggered and localized impact-triggered fan formation. Unraveling the evolution of alluvial fan formation would thereby provide even stronger constraints on the evolution of Mars' climate.

CHAPTER 5

SYNTHESIS

The 'prevailing view' of Mars' climate history is anchored on the belief that fluvial erosion was most intense and widespread before the formation of regionally-integrated valley networks, but very sparse after (Figure 1.3). In this dissertation, we used statistical methods to constrain our global view of the history of Mars' rivers. Although we did not establish a specific model for fluvial erosion through time, we were able to directionally revise the prevailing view (Figure 5.1).

In Chapter 2, we applied angular two-point-correlation statistics to detect crater clustering (on $\sim 10^2 - 10^3$ km spatial scales) on the early- and middle-Noachian highlands. While craters 8-32 km in diameter are significantly clustered on middle-Noachian terrains, craters in the same size range on early-Noachian terrains are consistent with being drawn randomly from a spatially uniform distribution. We interpreted this to indicate that resurfacing on the early-Noachian highlands was shallower than on the middle-Noachian highlands. This indicates that resurfacing could not have been uniform throughout the Noachian. Further, it indicates that previous work (e.g. Robbins et al., 2013; Quantin-Nataf et al., 2019) over-estimated globally-averaged pre-valley network fluvial erosion (Figure 5.1). This is consistent with (but doesn't prove) the increasingly popular view that a climatic optimum caused a global peak in fluvial erosion during the era of regionally-integrated valley network formation (e.g. Howard et al., 2005).

In Chapter 3, we introduced a novel model that relates Mars' obliquity to the distribution of elliptic crater orientations. Comparison of model output with global elliptic crater data allowed us to constrain the frequency of chaotic high-obliquity excursions, which are believed to have enabled recent river-forming climates on Mars (e.g. Jakosky and Carr, 1985). In general, the global preference for North-South orientated craters (which form when Mars is at low obliquities) vs. East-West oriented elliptic craters (which form when Mars is at high obliquities) is $\sim 3:2$. Thus, we found that the frequency of late-Hesperian-onward

high-obliquity ($\gtrsim 40°$) excursions was reduced by $\sim 50\%$ relative to prior expectations from dynamics alone. This indicates that, if high-obliquity excursions are indeed responsible for post-Noachian river-forming climates, then the frequency of river-forming climates was less than previously expected.

In Chapter 4, we used global impact crater and alluvial fan data to constrain the timing of alluvial fan formation. Regional studies have indicated alluvial fan formation had to have persisted into the Hesperian, ~ 3.4 Ga (Mangold et al., 2012a). However, adopting a global view and more sophisticated statistical modeling (i.e. using a more robust treatment of crater-counting-age uncertainty and allowing for spatially-patchy alluvial fan formation), we found that climate-driven fan formation likely persisted into the last ~ 2.5 Gyr, well into the Amazonian period. This provides an important constraint for climate modeling efforts, as greenhouse gas abundances in the atmosphere are believed to have rapidly declined early in Mars' history (e.g. Fassett and Head, 2011).

Together, these results point towards a revised view of Mars' climate history (Figure 5.1). Ancient fluvial erosion was shallower than previously estimated. Further, post-Noachian river-forming climates were less-frequent and more recent than previously expected. Perhaps more significantly, these studies serve as a proof-of-concept for crater statistics as a powerful tool that can be used for purposes beyond dating surfaces. All of our studies were data-limited. Thus, we expect that as new Mars crater data accumulates, our models will provide even tighter constraints on Mars' climate history, simply by re-running them with the new data.

In addition, some of these techniques have the potential to help decipher solar system dynamics beyond Mars. In particular, in chapter 3, we investigated how Mars' obliquity history correlates with the observed distribution of elliptic impact crater orientations. In principle, this method can be extended to see what other chaotic solar system parameters correlate with Mars' crater record. Further, one could in principle estimate the relative likelihoods of proposed ancient solar system evolution scenarios through combined analysis of impact craters on Mars, the Moon, and Mercury.

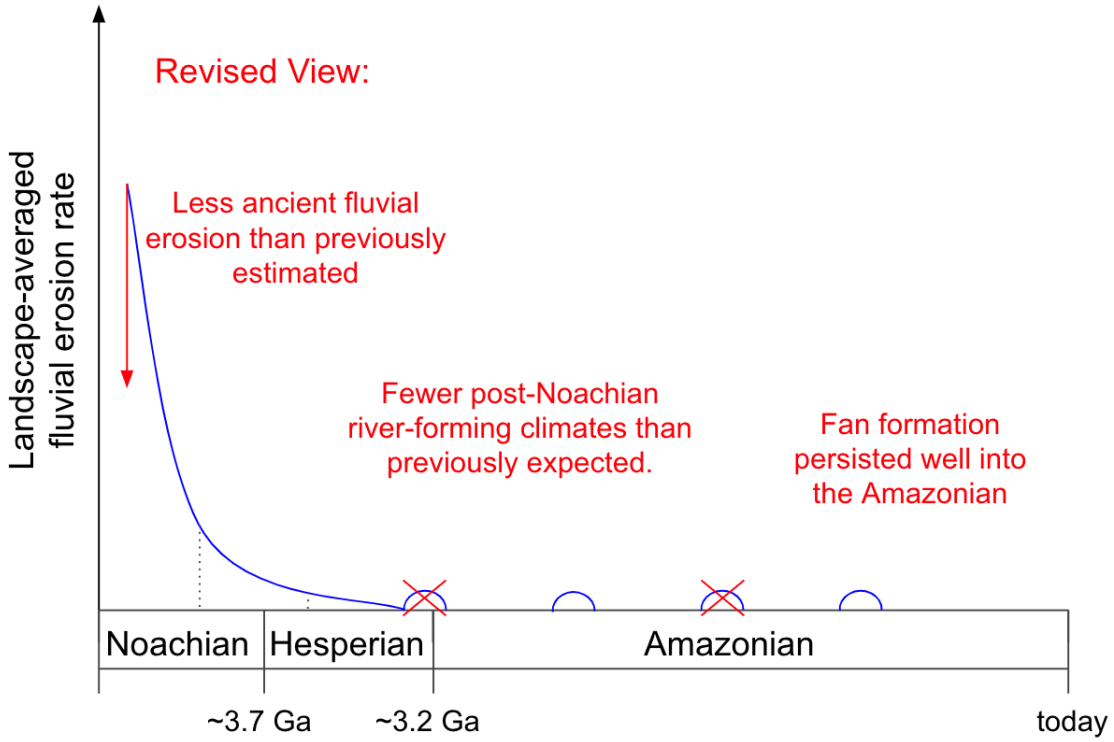

Figure 5.1: Revised View of the History of Fluvial Erosion on Mars. Ancient fluvial erosion inferred from degraded impact craters was shallower than previously expected (Chapter 2). High obliquity excursions in the late-Hesperian and Amazonian were less frequent than previously expected, limiting the potential for young river-forming climates (Chapter 3). Finally, alluvial fan formation had to have persisted well into the Amazonian (Chapter 4).

REFERENCES

J. C. Armstrong, C. B. Leovy, and T. Quinn. A 1 gyr climate model for mars: new orbital statistics and the importance of seasonally resolved polar processes. *Icarus*, 171(2):255 – 271, 2004.

R. E. Arvidson. Aqueous history of mars as inferred from landed mission measurements of rocks, soils, and water ice. *Journal of Geophysical Research: Planets*, 121(9):1602–1626, 2016.

V. R. Baker and D. J. Milton. Erosion by catastrophic floods on mars and earth. *Icarus*, 23 (1):27 – 41, 1974.

N. G. Barlow. Crater size-frequency distributions and a revised martian relative chronology. *Icarus*, 75(2):285 – 305, 1988.

S. P. Bhavsar. Bootstrap, data permuting, and extreme value distributions - getting the most out of small samples. In C. Jaschek and F. Murtagh, editors, *Errors, Bias, and Uncertainty in Astronomy*, pages 107–122. Cambridge University Press, 1990.

B. G. Bills. Non-chaotic obliquity variations of mars. *Lunar and Planetary Science Conference*, 2093, 2006.

C. Blake and J. Wall. Measurement of the angular correlation function of radio galaxies from the NRAO VLA Sky Survey. *Monthly Notices of the Royal Astronomical Society*, 329(2): L37–L41, 01 2002.

W. F. Bottke and M. D. Norman. The late heavy bombardment. *Annual Review of Earth and Planetary Sciences*, 45(1):619–647, 2017.

W. F. Bottke, S. G. Love, D. Tytell, and T. Glotch. Interpreting the elliptical crater populations on mars, venus, and the moon. *Icarus*, 145(1):108 – 121, 2000.

W. F. Bottke, A. Morbidelli, R. Jedicke, J.-M. Petit, H. F. Levison, P. Michel, and T. S. Metcalfe. Debiased orbital and absolute magnitude distribution of the near-earth objects. *Icarus*, 156(2):399 – 433, 2002.

W. F. Bottke, D. D. Durda, D. Nesvorný, R. Jedicke, A. Morbidelli, D. Vokrouhlický, and H. Levison. The fossilized size distribution of the main asteroid belt. *Icarus*, 175(1):111 – 140, 2005.

W. F. Bottke, D. Vokrouhlický, D. Minton, D. Nesvorný, A. Morbidelli, R. Brasser, B. Simonson, and H. F. Levison. An archaean heavy bombardment from a destabilized extension of the asteroid belt. *Nature*, 485(7396):78–81, 2012.

S. Bouley and R. A. Craddock. Age dates of valley network drainage basins and subbasins within sabae and arabia terrae, mars. *Journal of Geophysical Research: Planets*, 119(6): 1302–1310, 2014.

M. H. Carr. Formation of martian flood features by release of water from confined aquifers. *Journal of Geophysical Research: Solid Earth*, 84(B6):2995–3007, 1979.

J. C. Cawley and R. P. Irwin III. Evolution of escarpments, pediments, and plains in the noachian highlands of mars. *Journal of Geophysical Research: Planets*, 123(12):3167–3187, 2018.

J. E. Chambers. A hybrid symplectic integrator that permits close encounters between massive bodies. *Monthly Notices of the Royal Astronomical Society*, 304(4):793–799, 1999.

C. R. Chapman and K. L. Jones. Cratering and obliteration history of mars. *Annual Review of Earth and Planetary Sciences*, 5(1):515–538, 1977.

G. Collins, D. Elbeshausen, T. Davison, S. Robbins, and B. Hynek. The size-frequency distribution of elliptical impact craters. *Earth and Planetary Science Letters*, 310(1):1 – 8, 2011.

S. J. Conway, T. de Haas, T. N. Harrison, P. A. Carling, and J. Carrivick. *Martian gullies and their Earth analogues*. Geological Society of London, 2019.

R. A. Craddock and A. D. Howard. The case for rainfall on a warm, wet early mars. *Journal of Geophysical Research: Planets*, 107(E11):21–1–21–36, 2002.

R. A. Craddock and T. A. Maxwell. Resurfacing of the martian highlands in the amenthes and tyrrhena region. *Journal of Geophysical Research: Solid Earth*, 95(B9):14265–14278, 1990.

R. A. Craddock and T. A. Maxwell. Geomorphic evolution of the martian highlands through ancient fluvial processes. *Journal of Geophysical Research: Planets*, 98(E2):3453–3468, 1993.

M. Ćuk. Chronology and sources of lunar impact bombardment. *Icarus*, 218(1):69 – 79, 2012.

M. Ćuk and D. Nesvorný. Planetary chaos and the (in)stability of hungaria asteroids. *Icarus*, 304:9 – 13, 2018.

M. Ćuk, B. J. Gladman, and S. T. Stewart. Constraints on the source of lunar cataclysm impactors. *Icarus*, 207(2):590 – 594, 2010.

M. Davis and P. J. E. Peebles. A survey of galaxy redshifts. V. The two-point position and velocity correlations. *Astrophysical Journal*, 267:465–482, 1983.

J. L. Dickson, L. A. Kerber, C. I. Fassett, and B. L. Ehlmann. A global, blended CTX mosaic of mars with vectorized seam mapping: A new mosaicking pipeline using principles of non-destructive image editing. *Lunar and Planetary Science Conference*, 2018. Abstract #2480.

W. E. Dietrich, M. C. Palucis, R. M. E. Williams, K. W. Lewis, F. Rivera-Hernandez, and D. Y. Sumner. Fluvial gravels on mars. In D. Tsutsumi and J. B. Laronne, editors, *Gravel-Bed Rivers*, pages 755–783. John Wiley & Sons, Ltd, 2017.

K. A. Farley, C. Malespin, P. Mahaffy, J. P. Grotzinger, P. M. Vasconcelos, R. E. Milliken, M. Malin, K. S. Edgett, A. A. Pavlov, J. A. Hurowitz, J. A. Grant, H. B. Miller, R. Arvidson, L. Beegle, F. Calef, P. G. Conrad, W. E. Dietrich, J. Eigenbrode, R. Gellert, S. Gupta, V. Hamilton, D. M. Hassler, K. Lewis, S. M. McLennan, D. Ming, R. Navarro-González, S. P. Schwenzer, A. Steele, E. M. Stolper, D. Y. Sumner, D. Vaniman, A. Vasavada, K. Williford, and R. F. Wimmer-Schweingruber. In situ radiometric and exposure age dating of the martian surface. *Science*, 343(6169), 2014.

C. I. Fassett. Analysis of impact crater populations and the geochronology of planetary surfaces in the inner solar system. *Journal of Geophysical Research: Planets*, 121(10): 1900–1926, 2016.

C. I. Fassett and J. W. Head. The timing of martian valley network activity: Constraints from buffered crater counting. *Icarus*, 195(1):61 – 89, 2008.

C. I. Fassett, J. W. Head, S. J. Kadish, E. Mazarico, G. A. Neumann, D. E. Smith, and M. T. Zuber. Lunar impact basins: Stratigraphy, sequence and ages from superposed impact crater populations measured from lunar orbiter laser altimeter (lola) data. *Journal of Geophysical Research: Planets*, 117(E12), 2012.

C. I. Fassett, J. S. Levy, J. L. Dickson, and J. W. Head. An extended period of episodic northern mid-latitude glaciation on mars during the middle to late amazonian: Implications for long-term obliquity history. *Geology*, 42(9):763–766, 2014.

J. L. Fastook, J. W. Head, D. R. Marchant, F. Forget, and J.-B. Madeleine. Early mars climate near the noachian-hesperian boundary: Independent evidence for cold conditions from basal melting of the south polar ice sheet (dorsa argentea formation) and implications for valley network formation. *Icarus*, 219(1):25 – 40, 2012.

A. W. Fitzgibbon, M. Pilu, and R. B. Fisher. Direct least squares fitting of ellipses. In *Proceedings of 13th International Conference on Pattern Recognition*, pages 253–257, 1996.

F. Forget, S. Byrne, J. W. Head, M. A. Mischna, and N. Schörghofer. Recent climate variations. In R. M. Haberle, R. T. Clancy, F. Forget, M. D. Smith, and R. W. Zurek, editors, *The Atmosphere and Climate of Mars*, pages 464–496. Cambridge University Press, 2017.

N. K. Forsberg-Taylor, A. D. Howard, and R. A. Craddock. Crater degradation in the martian highlands: Morphometric analysis of the sinus sabaeus region and simulation modeling suggest fluvial processes. *Journal of Geophysical Research: Planets*, 109(E5), 2004.

J. A. Grant and S. A. Wilson. Late alluvial fan formation in southern margaritifer terra, mars. *Geophysical Research Letters*, 38(8), 2011.

J. A. Grant and S. A. Wilson. A possible synoptic source of water for alluvial fan formation in southern margaritifer terra, mars. *Planetary and Space Science*, 72(1):44 – 52, 2012.

R. E. Grimm, K. P. Harrison, D. E. Stillman, and M. R. Kirchoff. On the secular retention of ground water and ice on mars. *Journal of Geophysical Research: Planets*, 122(1):94–109, 2017.

R. M. Haberle, J. R. Murphy, and J. Schaeffer. Orbital change experiments with a mars general circulation model. *Icarus*, 161(1):66 – 89, 2003.

W. K. Hartmann. Martian cratering 8: Isochron refinement and the chronology of mars. *Icarus*, 174(2):294 – 320, 2005.

W. K. Hartmann and G. Neukum. Cratering chronology and the evolution of mars. *Space Science Reviews*, 96(1):165–194, 2001.

E. Hauber, T. Platz, D. Reiss, L. Le Deit, M. G. Kleinhans, W. A. Marra, T. de Haas, and P. Carbonneau. Asynchronous formation of hesperian and amazonian aged deltas on mars and implications for climate. *Journal of Geophysical Research: Planets*, 118(7):1529–1544, 2013.

N. Hoffman. White mars: A new model for mars' surface and atmosphere based on co2. *Icarus*, 146(2):326 – 342, 2000.

S. Holo and E. Kite. The spatial signature of a changing ancient impactor population for mars. *Icarus*, 337:113447, 2020.

S. J. Holo, E. S. Kite, and S. J. Robbins. Mars obliquity history constrained by elliptic crater orientations. *Earth and Planetary Science Letters*, 496:206 – 214, 2018.

A. D. Howard. Simulating the development of martian highland landscapes through the interaction of impact cratering, fluvial erosion, and variable hydrologic forcing. *Geomorphology*, 91(3):332 – 363, 2007.

A. D. Howard, J. M. Moore, and R. P. Irwin III. An intense terminal epoch of widespread fluvial activity on early mars: 1. valley network incision and associated deposits. *Journal of Geophysical Research: Planets*, 110(E12), 2005.

B. Hynek and R. Phillips. Evidence for extensive denudation of the martian highlands. *Geology*, 29:407–410, 2001.

B. M. Hynek, M. Beach, and M. R. T. Hoke. Updated global map of martian valley networks and implications for climate and hydrologic processes. *Journal of Geophysical Research: Planets*, 115(E9), 2010.

R. P. Irwin, R. A. Craddock, and A. D. Howard. Interior channels in martian valley networks: Discharge and runoff production. *Geology*, 33(6):489–492, 2005a.

R. P. Irwin, A. D. Howard, R. A. Craddock, and J. M. Moore. An intense terminal epoch of widespread fluvial activity on early mars: 2. increased runoff and paleolake development. *Journal of Geophysical Research: Planets*, 110(E12), 2005b.

R. P. Irwin, K. L. Tanaka, and S. J. Robbins. Distribution of early, middle, and late

noachian cratered surfaces in the martian highlands: Implications for resurfacing events and processes. *Journal of Geophysical Research: Planets*, 118(2):278–291, 2013.

R. P. Irwin, K. W. Lewis, A. D. Howard, and J. A. Grant. Paleohydrology of eberswalde crater, mars. *Geomorphology*, 240:83 – 101, 2015.

B. A. Ivanov. Mars/moon cratering rate ratio estimates. In R. Kallenbach, J. Geiss, and W. K. Hartmann, editors, *Chronology and Evolution of Mars*, pages 87–104. Springer Netherlands, 2001.

B. A. Ivanov, G. Neukum, W. F. Bottke, and W. K. Hartmann. The comparison of size frequency distributions of impact craters and asteroids and the planetary cratering rate. In W. F. Bottke, A. Cellino, P. Paolicchi, and R. Binzel, editors, *Asteroids III*, pages 89–101. University of Arizona Press, 2002.

B. M. Jakosky and M. H. Carr. Possible precipitation of ice at low latitudes of mars during periods of high obliquity. *Nature*, 315(6020):559–561, 1985.

Y. JeongAhn and R. Malhotra. The current impact flux on mars and its seasonal variation. *Icarus*, 262:140 – 153, 2015.

D. V. Kent, P. E. Olsen, C. Rasmussen, C. Lepre, R. Mundil, R. B. Irmis, G. E. Gehrels, D. Giesler, J. W. Geissman, and W. G. Parker. Empirical evidence for stability of the 405 kiloyear jupiter-venus eccentricity cycle over hundreds of millions of years. *Proceedings of the National Academy of Sciences*, 115(24):6153–6158, 2018.

M. R. Kirchoff. Can spatial statistics help decipher impact crater saturation? *Meteoritics & Planetary Science*, 53(4):874–890, 2018.

E. S. Kite. Geologic constraints on early mars climate. *Space Science Reviews*, 215(1):10, 2019.

E. S. Kite, I. Matsuyama, M. Manga, J. T. Perron, and J. X. Mitrovica. True polar wander driven by late stage volcanism and the distribution of paleopolar deposits on mars. *Earth and Planetary Science Letters*, 280(1):254 – 267, 2009.

E. S. Kite, I. Halevy, M. A. Kahre, M. J. Wolff, and M. Manga. Seasonal melting and the formation of sedimentary rocks on mars, with predictions for the gale crater mound. *Icarus*, 223(1):181 – 210, 2013.

E. S. Kite, J.-P. Williams, A. Lucas, and O. Aharonson. Low palaeopressure of the martian atmosphere estimated from the size distribution of ancient craters. *Nature Geoscience*, 7 (5):335–339, 2014.

E. S. Kite, A. D. Howard, A. S. Lucas, J. C. Armstrong, O. Aharonson, and M. P. Lamb. Stratigraphy of aeolis dorsa, mars: Stratigraphic context of the great river deposits. *Icarus*, 253:223 – 242, 2015.

E. S. Kite, P. Gao, C. Goldblatt, M. A. Mischna, D. P. Mayer, and Y. L. Yung. Methane bursts as a trigger for intermittent lake forming climates on post noachian mars. *Nature Geoscience*, 10(10):737–740, 2017a.

E. S. Kite, J. Sneed, D. P. Mayer, and S. A. Wilson. Persistent or repeated surface habitability on mars during the late hesperian - amazonian. *Geophysical Research Letters*, 44(9):3991–3999, 2017b.

E. S. Kite, D. P. Mayer, S. A. Wilson, J. M. Davis, A. S. Lucas, and G. Stucky de Quay. Persistence of intense, climate driven runoff late in mars history. *Science Advances*, 5(3), 2019.

E. R. Kraal, E. Asphaug, J. M. Moore, A. Howard, and A. Bredt. Catalogue of large alluvial fans in martian impact craters. *Icarus*, 194(1):101 – 110, 2008.

M. A. Kreslavsky. Statistical Characterization of Spatial Distribution of Impact Craters: Implications to Present Day Cratering Rate on Mars. In *Seventh International Conference on Mars*, volume 1353, page 3325, 2007.

M. A. Kreslavsky and J. W. Head. Mars at very low obliquity: Atmospheric collapse and the fate of volatiles. *Geophysical Research Letters*, 32(12), 2005.

M. A. Kreslavsky and J. W. Head. Mars climate history: Insights from impact crater wall slope statistics. *Geophysical Research Letters*, 45(4):1751–1758, 2018.

M. P. Lamb, A. D. Howard, J. Johnson, K. X. Whipple, W. E. Dietrich, and J. T. Perron. Can springs cut canyons into rock? *Journal of Geophysical Research: Planets*, 111(E7), 2006.

S. D. Landy and A. S. Szalay. Bias and Variance of Angular Correlation Functions. *Astrophysical Journal*, 412:64, 1993.

J. Laskar and P. Robutel. The chaotic obliquity of the planets. *Nature*, 361(6413):608–612, 1993.

J. Laskar, A. Correia, M. Gastineau, F. Joutel, B. Levrard, and P. Robutel. Long term evolution and chaotic diffusion of the insolation quantities of mars. *Icarus*, 170(2):343 – 364, 2004.

M. Le Feuvre and M. A. Wieczorek. Nonuniform cratering of the terrestrial planets. *Icarus*, 197(1):291 – 306, 2008.

G. Li and K. Batygin. On the spin-axis dynamics of a moonless earth. *The Astrophysical Journal*, 790(1):69, 2014.

J. J. Lissauer, J. W. Barnes, and J. E. Chambers. Obliquity variations of a moonless earth. *Icarus*, 217(1):77 – 87, 2012.

W. Luo, X. Cang, and A. D. Howard. New martian valley network volume estimate consistent with ancient ocean and warm and wet climate. *Nature Communications*, 8(1):15766, 2017.

C. Ma, S. R. Meyers, and B. B. Sageman. Theory of chaotic orbital variations confirmed by cretaceous geological evidence. *Nature*, 542(7642):468–470, 2017.

N. Mangold, S. Adeli, S. Conway, V. Ansan, and B. Langlais. A chronology of early mars climatic evolution from impact crater degradation. *Journal of Geophysical Research: Planets*, 117(E4), 2012a.

N. Mangold, E. Kite, M. Kleinhans, H. Newsom, V. Ansan, E. Hauber, E. Kraal, C. Quantin, and K. Tanaka. The origin and timing of fluvial activity at eberswalde crater, mars. *Icarus*, 220(2):530 – 551, 2012b.

S. Marchi. A New Crater Chronology for Mars, Implications for Jezero Crater. In *AAS/Division for Planetary Sciences Meeting Abstracts*, volume 52 of *AAS/Division for Planetary Sciences Meeting Abstracts*, page 311.01, 2020.

I. Matsuyama and M. Manga. Mars without the equilibrium rotational figure, tharsis, and the remnant rotational figure. *Journal of Geophysical Research: Planets*, 115(E12), 2010.

G. Michael. Planetary surface dating from crater size–frequency distribution measurements: Multiple resurfacing episodes and differential isochron fitting. *Icarus*, 226(1):885 – 890, 2013.

G. Michael, T. Platz, T. Kneissl, and N. Schmedemann. Planetary surface dating from crater size–frequency distribution measurements: Spatial randomness and clustering. *Icarus*, 218 (1):169 – 177, 2012.

G. Michael, T. Kneissl, and A. Neesemann. Planetary surface dating from crater size-frequency distribution measurements: Poisson timing analysis. *Icarus*, 277:279 – 285, 2016.

J. M. Moore and A. D. Howard. Large alluvial fans on mars. *Journal of Geophysical Research: Planets*, 110(E4), 2005.

A. Morbidelli, D. Nesvorny, V. Laurenz, S. Marchi, D. Rubie, L. Elkins-Tanton, M. Wieczorek, and S. Jacobson. The timeline of the lunar bombardment: Revisited. *Icarus*, 305:262 – 276, 2018.

A. Morgan, A. Howard, D. Hobley, J. Moore, W. Dietrich, R. Williams, D. Burr, J. Grant, S. Wilson, and Y. Matsubara. Sedimentology and climatic environment of alluvial fans in the martian saheki crater and a comparison with terrestrial fans in the atacama desert. *Icarus*, 229:131 – 156, 2014.

A. M. Morgan and S. A. Wilson. Utilizing a global database to explore morphologic trends of martian alluvial fans. *Lunar and Planetary Science Conference*, 2019. Abstract #3256.

D. Nesvorný, F. Roig, and W. F. Bottke. Modeling the historical flux of planetary impactors. *The Astronomical Journal*, 153(3):103, 2017.

D. Nesvorný, D. Vokrouhlický, W. F. Bottke, and H. F. Levison. Evidence for very early migration of the solar system planets from the patroclus–menoetius binary jupiter trojan. *Nature Astronomy*, 2(11):878–882, 2018.

G. Neukum, B. A. Ivanov, and W. K. Hartmann. Cratering records in the inner solar system in relation to the lunar reference system. *Space Science Reviews*, 96(1):55–86, 2001.

E. J. Öpik. The martian surface. *Science*, 153(3733):255, 07 1966.

M. C. Palucis, W. E. Dietrich, A. G. Hayes, R. M. E. Williams, S. Gupta, N. Mangold, H. Newsom, C. Hardgrove, F. Calef III, and D. Y. Sumner. The origin and evolution of the peace vallis fan system that drains to the curiosity landing area, gale crater, mars. *Journal of Geophysical Research: Planets*, 119(4):705–728, 2014.

M. C. Palucis, J. Jasper, B. Garczynski, and W. E. Dietrich. Quantitative assessment of uncertainties in modeled crater retention ages on mars. *Icarus*, 341:113623, 2020.

R. J. Phillips, B. J. Davis, K. L. Tanaka, S. Byrne, M. T. Mellon, N. E. Putzig, R. M. Haberle, M. A. Kahre, B. A. Campbell, L. M. Carter, I. B. Smith, J. W. Holt, S. E. Smrekar, D. C. Nunes, J. J. Plaut, A. F. Egan, T. N. Titus, and R. Seu. Massive CO_2 ice deposits sequestered in the south polar layered deposits of mars. *Science*, 332(6031):838–841, 2011.

C. Quantin-Nataf, R. Craddock, F. Dubuffet, L. Lozac'h, and M. Martinot. Decline of crater obliteration rates during early martian history. *Icarus*, 317:427 – 433, 2019.

J. D. Riggs, S. J. Robbins, M. R. Kirchoff, E. B. Bierhaus, and B. P. Weaver. Understanding Spatial Statistics for Purposes of Identifying Non-Primary and Saturated Impact Crater Populations. In *Issues in Crater Studies and the Dating of Planetary Surfaces*, volume 1841, page 9050, 2015.

S. J. Robbins. New crater calibrations for the lunar crater-age chronology. *Earth and Planetary Science Letters*, 403:188 – 198, 2014.

S. J. Robbins and B. M. Hynek. A new global database of mars impact craters ≥ 1 km: 1. database creation, properties, and parameters. *Journal of Geophysical Research: Planets*, 117(E5), 2012.

S. J. Robbins and B. M. Hynek. The secondary crater population of mars. *Earth and Planetary Science Letters*, 400:66 – 76, 2014.

S. J. Robbins, B. M. Hynek, R. J. Lillis, and W. F. Bottke. Large impact crater histories of mars: The effect of different model crater age techniques. *Icarus*, 225(1):173 – 184, 2013.

S. J. Robbins, I. Antonenko, M. R. Kirchoff, C. R. Chapman, C. I. Fassett, R. R. Herrick, K. Singer, M. Zanetti, C. Lehan, D. Huang, and P. L. Gay. The variability of crater identification among expert and community crater analysts. *Icarus*, 234:109 – 131, 2014.

S. J. Robbins, J. D. Riggs, B. P. Weaver, E. B. Bierhaus, C. R. Chapman, M. R. Kirchoff, K. N. Singer, and L. R. Gaddis. Revised recommended methods for analyzing crater size-frequency distributions. *Meteoritics & Planetary Science*, 53(4):891–931, 2018.

K. Scanlon, J. Head, J. Fastook, and R. Wordsworth. The Dorsa Argentea formation and the Noachian-Hesperian climate transition. *Icarus*, 299:339 – 363, 2018.

A. Soto, M. Mischna, T. Schneider, C. Lee, and M. Richardson. Martian atmospheric collapse: Idealized GCM studies. *Icarus*, 250:553 – 569, 2015.

S. W. Squyres, C. Howell, M. C. Liu, and J. J. Lissauer. Investigation of crater "saturation" using spatial statistics. *Icarus*, 125(1):67 – 82, 1997.

R. G. Strom, R. Malhotra, T. Ito, F. Yoshida, and D. A. Kring. The origin of planetary impactors in the inner solar system. *Science*, 309(5742):1847–1850, 2005.

R. G. Strom, R. Malhotra, Z.-Y. Xiao, T. Ito, F. Yoshida, and L. R. Ostrach. The inner solar system cratering record and the evolution of impactor populations. *Research in Astronomy and Astrophysics*, 15(3):407–434, 2015.

G. Stucky de Quay, E. S. Kite, and D. P. Mayer. Prolonged fluvial activity from channel-fan systems on mars. *Journal of Geophysical Research: Planets*, 124(11):3119–3139, 2019.

K. Tanaka, S. Robbins, C. Fortezzo, J. Skinner, and T. Hare. The digital global geologic map of mars: Chronostratigraphic ages, topographic and crater morphologic characteristics, and updated resurfacing history. *Planetary and Space Science*, 95:11 – 24, 2014.

J. Touma and J. Wisdom. The chaotic obliquity of mars. *Science*, 259(5099):1294–1297, 1993.

M. Turbet, C. Gillmann, F. Forget, B. Baudin, A. Palumbo, J. Head, and O. Karatekin. The environmental effects of very large bolide impacts on early mars explored with a hierarchy of numerical models. *Icarus*, 335:113419, 2020.

J. V. Wall and C. R. Jenkins. *Practical Statistics for Astronomers 2nd Ed.* Cambridge University Press, 2012.

J. V. Wall, G. T. Rixon, and C. R. Benn. The Nature of mJy Radio Sources. In G. L. Chincarini, A. Iovino, T. Maccacaro, and D. Maccagni, editors, *Observational Cosmology*, volume 51 of *Astronomical Society of the Pacific Conference Series*, page 576, 1993.

W. R. Ward. Large-scale variations in the obliquity of mars. *Science*, 181(4096):260–262, 1973.

A. Warren, S. Holo, E. Kite, and S. Wilson. Overspilling small craters on a dry mars: Insights from breach erosion modeling. *Earth and Planetary Science Letters*, page 116671, 2020.

D. K. Weiss and J. W. Head. Crater degradation in the noachian highlands of mars: Assessing the hypothesis of regional snow and ice deposits on a cold and icy early mars. *Planetary and Space Science*, 117:401 – 420, 2015.

R. M. Williams and M. C. Malin. Sub-kilometer fans in mojave crater, mars. *Icarus*, 198(2): 365 – 383, 2008.

S. A. Wilson, A. D. Howard, J. M. Moore, and J. A. Grant. A cold-wet middle-latitude environment on mars during the hesperian-amazonian transition: Evidence from northern arabia valleys and paleolakes. *Journal of Geophysical Research: Planets*, 121(9):1667–1694, 2016.

R. D. Wordsworth. The climate of early mars. *Annual Review of Earth and Planetary Sciences*, 44(1):381–408, 2016.

A. P. Zent. Orbital Drivers of Climate Change on Earth and Mars. In S. J. Mackwell, A. A. Simon-Miller, J. W. Harder, and M. A. Bullock, editors, *Comparative Climatology of Terrestrial Planets*, page 505. University of Arizona Press, 2013.

APPENDIX A

APPENDIX TO CHAPTER 2

A.1 Estimating the Angular Two-Point Correlation Function

We described $w(\theta)$ as an "enhancement factor" of pairwise distances relative to that expected for random points from a spatially-uniform distribution. This interpretation leads to an intuitive method for estimating $w(\theta)$ (Blake and Wall, 2002). First, one generates a random uniformly-distributed set of n_r points and masks it to the same area as the data (which in our case is the geologic unit under investigation). One then computes DD, the counts of pairwise distances (in bins of separation) of craters within our database. One also computes RR, the counts of pairwise distances of craters in the randomly generated catalog. Finally, one computes:

$$w(\theta) = \frac{n_r(n_r-1)}{n_d(n_d-1)}\frac{DD}{RR} - 1 \tag{A.1}$$

where n_d is the number of craters in our data set. This intuitively ratios the probability distribution of measured pairwise distances to that expected in a random catalog. Landy and Szalay (1983) demonstrated that an improved estimator, which involves calculating DR (pairwise distances between points in the data set and in the random catalog), can significantly reduce bias:

$$w(\theta) = \frac{n_r(n_r-1)}{n_d(n_d-1)}\frac{DD}{RR} - 2\frac{DR}{RR}\frac{n_r-1}{n_d} + 1 \tag{A.2}$$

Thus, we use the Landy and Szalay (1983) estimator throughout our study.

A.2 Code and Reproducibility

We present the necessary scripts to reproduce the figures in Chapter 2 in the order that they should be run. Each individual script is annotated with its purpose and instructions for use (text below the code blocks). Some code blocks extend for several pages, as noted by the line numbering. We note that the scripts are specific to the computing environment and directory structure in which they were run, and the code will likely not work "out of the box". We note that Figure 2.2 is a map figure and would be best reproduced using GIS software and the Tanaka et al. (2014) global geologic map.

Code A.1: agu_figs.py

```
1
2  # coding: utf-8
3
4  # In[1]:
5
6
7  import numpy as np
8  import matplotlib.pyplot as plt
9  import pandas as pd
10 from crater_stats import *
11 from sklearn.neighbors import BallTree
12 get_ipython().magic(u'matplotlib inline')
13
14
15 # In[2]:
16
17
18 Nh, marsmap = load_highlands()
19
20
21 # In[3]:
22
23
24 bins = 2.**(np.arange(0,8.5,0.5))
25 Nh_cdf = binned_cdf(Nh.diam,bins)
26
27
28 # In[6]:
29
30
31 fig = plt.figure(figsize=(3.54331,0.75*3.54331))
32 plt.errorbar((2**0.25)*bins[:-1], -np.diff(Nh_cdf)/marsmap.area.sum(),
33              yerr=np.sqrt(-np.diff(Nh_cdf))/marsmap.area.sum(),
34              fmt = '.', c = 'k', markersize = 10, label = 'Noachian
       Highlands')
35
36 plt.xscale('log')
37 plt.yscale('log')
38 plt.grid()
39 plt.xlabel('Diameter (km)')
40 plt.ylabel('Craters/$km^2$')
41 plt.savefig('Nh.tif',dpi=600, bbox_inches="tight")
```

Produces Figure 2.1. It was originally run in a Jupyter notebook using Anaconda2 distributions for numpy, matplotlib, pandas, and SK-Learn.

Code A.2: obliteration.py

```
# coding: utf-8
# In[1]:


import numpy as np
import matplotlib.pyplot as plt
import pandas as pd
from crater_stats import *
from sklearn.neighbors import BallTree


# In[2]:


bins = 10** np.linspace(np.log10(2), np.log10(30), 10)
diambins = 2.**(np.arange(2,6,1))


# In[3]:


bins


# In[4]:


units = ['eNh','mNh','lNh']

# Looping over geologic units
for unit in units:
    # Load the units
    rand = load_random_highlands(num = 10**6,latrange=(-30,0),units=[
    unit])
    Nh, marsmap = load_highlands(latrange=(-30,0),units=[unit])

    # Looping over diameter ranges
    for i in range(len(diambins)-1):
        craters = trim(Nh,'diam',diambins[i],diambins[i+1])
        degd = trim(craters,'deg',0,3)
        fresh = trim(craters,'deg',2,5)

        diterations = len(degd)
        fiterations = len(fresh)

        np.savetxt(unit+'_deg_'+str(int(diambins[i]))+'.csv',
                   boot_angular(format_lat_lon(degd.lat.values,degd.lon
    .values),diterations,bins,
                       x_R = format_lat_lon(rand.lat.values,rand.lon.
    values)),delimiter=',')
```

```
48
49          print(unit+'_deg_'+str(int(diambins[i]))+'.csv')
50
51          np.savetxt(unit+'_fresh_'+str(int(diambins[i]))+'.csv',
52                     boot_angular(format_lat_lon(fresh.lat.values,fresh.
    lon.values),fiterations,bins,
53                          x_R = format_lat_lon(rand.lat.values,rand.lon.
    values)),delimiter=',')
54
55          print(unit+'_fresh_'+str(int(diambins[i]))+'.csv')
56
57
58
59  # In[4]:
60
61
62  Nh, marsmap = load_highlands(latrange=(-30,0),units=['eNh'])
63  len(trim(trim(Nh,'deg',0,3),'diam',8,16))
64
65
66  # In[5]:
67
68
69  x = (bins[1:] + bins[:-1])/2
70  units = ['eNh','mNh','lNh']
71
72  for unit in units:
73
74      for i in range(len(diambins)-1):
75
76          freshy = np.array(np.loadtxt(unit+'_fresh_'+str(int(diambins[i
    ]))+'.csv',delimiter=','))
77          np.savetxt(unit+'_fresh_'+str(int(diambins[i]))+'_linfits.csv',
78                     np.array([linear_model(np.log10(x),np.log10(1+freshy[
    j])).params for j in range(len(freshy))]),
79                     delimiter=',')
80
81          print(unit+'_fresh_'+str(int(diambins[i]))+'_linfits.csv')
82
83
84          degy = np.array(np.loadtxt(unit+'_deg_'+str(int(diambins[i]))+'
    _.csv',delimiter=','))
85          np.savetxt(unit+'_deg_'+str(int(diambins[i]))+'_linfits.csv',
86                     np.array([linear_model(np.log10(x),np.log10(1+degy[j
    ])).params for j in range(len(degy))]),
87                     delimiter=',')
88          print(unit+'_deg_'+str(int(diambins[i]))+'_linfits.csv')
89
90
91
92
```

```
# In[8]:


units = ['eNh','mNh']
plt.figure(figsize=(7.48031,.5*7.48031))

counter = 1
for unit in units:

    for i in range(len(diambins)-1):
        print(i)

        twopoint = np.loadtxt(unit+'_deg_' + str(int(diambins[i]))+'.csv',delimiter=',')
        twopointfr = np.loadtxt(unit+'_fresh_'+str(int(diambins[i]))+'.csv',delimiter=',')
        bins = 10** np.linspace(np.log10(2), np.log10(30), 10)

        means = np.array([np.mean(x) for x in twopoint.T])
        errs = np.array([np.std(x) for x in twopoint.T])

        meansfr = np.array([np.mean(x) for x in twopointfr.T])
        errsfr = np.array([np.std(x) for x in twopointfr.T])

        ax = plt.subplot(230+counter)

        plt.errorbar(.97*(bins[1:] + bins[:-1])/2,1+means,yerr=errs, fmt = '.', c='k',markersize=10)
        plt.errorbar(1.03*(bins[1:] + bins[:-1])/2,1+meansfr,yerr=errsfr, fmt = '.', c='r',markersize=10)
        #plt.axis([1,30,0.9,])


        plt.plot([1,30], [1,1],'-',color='k',label='Uniform')

        plt.legend()
        plt.xscale('log')
        #plt.yscale('log')

        plt.axis([2,30,0.8,1.4])

        plt.xticks([2,10,30],['2','10', '30'])

        if counter < 4:
            plt.title(str(int(diambins[i])) + ' - ' + str(int(diambins[i+1])) + ' km')
        if counter == 1:
            plt.ylabel('1 + w($\Theta$)',fontsize=12)
        if counter==4:
            plt.ylabel('1 + w($\Theta$)',fontsize=12)
        if counter < 4:
```

```
            plt.annotate('eNh',xy=(18,.82))
        if counter >= 4:
            plt.annotate('mNh',xy=(17,.82))
        if counter >= 4:
            plt.xlabel('Angular Distance, $\Theta$ ($^o$)',fontsize=12)
        if counter != 1 and counter != 4:
            ax.get_yaxis().set_visible(False)


        counter+=1

plt.savefig('2CF.tif',dpi=600, bbox_inches="tight")


# In[7]:


units = ['eNh','mNh']
plt.figure(figsize=(7.48031,.5*7.48031))

counter = 1
for unit in units:

    for i in range(len(diambins)-1):
        results = np.loadtxt(unit + '_deg_' + str(int(diambins[i])) +'_linfits.csv',delimiter=',')
        resultsfr = np.loadtxt(unit + '_fresh_' + str(int(diambins[i])) +'_linfits.csv',delimiter=',')

        slopes = results.T[1]
        slopesfr = resultsfr.T[1]

        slopes = slopes[~np.isnan(slopes)]
        slopesfr = slopesfr[~np.isnan(slopesfr)]

        ax = plt.subplot(230+counter)

        frac = max((1.*len(slopes[slopes>0]))/len(slopes), 1./len(slopes))



        if counter == 6:
            slopesfr = slopesfr[slopesfr < 0.5]

        ax.hist(slopesfr,bins=20,alpha = 0.5,color='r')
        ax.hist(slopes,bins=20,alpha = 0.7,color='k',label='p < ' + str(frac))

        #plt.legend()
        plt.annotate('p < ' + str(frac),xy=(0.025,70))
```

```
        plt.axis([-0.15,0.15,0,80])

        if counter == 1:
            plt.ylabel('eNh counts',fontsize=12)
        if counter==4:
            plt.ylabel('mNh counts',fontsize=12)
        if counter >= 4:
            plt.xlabel('Slope',fontsize=12)
            plt.plot([0,0],[0,100],color='k')
        if counter != 1 and counter != 4:
            ax.get_yaxis().set_visible(False)
        if counter < 4:
            plt.title(str(int(diambins[i])) + ' - ' + str(int(diambins[
    i+1])) + ' km')
            plt.plot([0,0],[0,100],color='k')

        counter+=1

plt.savefig('2CF_slopes.tif',dpi=600, bbox_inches="tight")


# In[68]:


test = np.loadtxt('mNh_deg_4_linfits.csv',delimiter=',')
test2 = np.loadtxt('mNh_deg_8_linfits.csv',delimiter=',')
test3 = np.loadtxt('mNh_deg_16_linfits.csv',delimiter=',')

slopes = test.T[1]
slopes2 = test2.T[1]
slopes3 = test3.T[1]

slopes = slopes[~np.isnan(slopes)]
slopes2 = slopes2[~np.isnan(slopes2)]
slopes3 = slopes3[~np.isnan(slopes3)]

plt.hist(slopes3,bins=15, label='16-32 km',alpha=0.5)
plt.hist(slopes,bins=15,label='4-8 km',alpha=0.4)
plt.hist(slopes2,bins=15, label='8-16 km',alpha=0.4)

plt.plot([0,0],[0,80],'r',linewidth=3)
plt.legend()

print((1.*len(slopes[slopes>0]))/len(slopes))
print((1.*len(slopes2[slopes2>0]))/len(slopes2))
print((1.*len(slopes3[slopes3>0]))/len(slopes3))
```

Produces Figures 2.3 and 2.4. It was originally run in a Jupyter notebook using Anaconda2 distributions for numpy, matplotlib, pandas, and SK-Learn.

Code A.3: crater_stats.py

```
import numpy as np
from sklearn.neighbors import BallTree, KNeighborsRegressor,
    RadiusNeighborsRegressor
from sklearn.utils import resample
import statsmodels.api as sm
import pandas as pd
import os

# Generate points uniformly on a sphere
def uniform_sphere(latlim, lonlim, size=1):
    zlim = np.sin(np.pi * np.asarray(latlim)/180.)
    z = zlim[0] + (zlim[1] - zlim[0]) * np.random.random(size)
    lat = (180./np.pi) * np.arcsin(z)
    lon = lonlim[0] + (lonlim[1] - lonlim[0]) * np.random.random(size)
    return np.vstack([lat,lon]).T

def makebins(latrange=(-90,90), lonrange=(-180,180), dx=0.5,dlon=None):
    if dlon == None:
        dlon = dx
    latbins = np.arange(min(latrange),max(latrange) + dx,dx)
    lonbins = np.arange(min(lonrange),max(lonrange) + dlon,dlon)
    return latbins, lonbins

# Trim pandas data frame
def trim(data,value, minval,maxval,abs_=False):
    if abs_:
        return data[(abs(data[value]) > minval) & (abs(data[value]) <
    maxval)]
    else:
        return data[(data[value] > minval) & (data[value] < maxval)]

# Return area for a band of latitude on a sphere
def lat_band_area(lat, ppd = 2, r = 3396):
    return 2*r*r*np.pi*np.abs(np.sin(np.deg2rad(lat+(.5/ppd))) - np.sin
    (np.deg2rad(lat-(.5/ppd))))

# Calculate the number of data points greater than a critical value
def N(data,minval):
    return float(len(data[data>=minval]))

def gridmap(testmap, latbins, lonbins):
    testmap['latbin'] = pd.cut(testmap.lat, latbins)
    testmap['lonbin'] = pd.cut(testmap.lon, lonbins)

    return testmap

# Calculate binned cdf of a value
def binned_cdf(data, vals):
    return np.array([N(data,val) for val in vals])

```

```
48 def get_correlation(x,y):
49     return np.corrcoef(x,y)[0][1]
50
51 def linear_model(x,y):
52     results = sm.OLS(y, sm.add_constant(x)).fit()
53     return results
54
55 def get_hood(testmap, craters, lat, lon, dx):
56     minlon = lon - dx - 0.25
57     maxlon = lon + dx + 0.25
58     minlat = lat - dx - 0.25
59     maxlat = lat + dx + 0.25
60
61     tempmap = trim(testmap,'lat',minlat,maxlat)
62     finmap = trim(tempmap, 'lon',minlon,maxlon)
63
64     tempcrat = trim(craters,'lat',minlat,maxlat)
65     fincrat = trim(tempcrat,'lon',minlon,maxlon)
66
67     if minlon < -180:
68         finmap = pd.concat([finmap,trim(tempmap,'lon',minlon+360.,180)
    ])
69         fincrat = pd.concat([fincrat,trim(tempcrat,'lon',minlon
    +360.,180)])
70     elif maxlon > 180:
71         finmap = pd.concat([finmap,trim(tempmap,'lon',-180,maxlon-360.)
    ])
72         fincrat = pd.concat([fincrat,trim(tempcrat,'lon',-180,maxlon
    -360.)])
73
74     return finmap, fincrat
75
76 def load_marsmap(latrange=(-90,90), lonrange=(-180,180), unit='',
    notstring = None):
77     dx=0.5
78     marsmap = pd.read_csv('marsmap_2ppd.csv').fillna(0).drop(columns= [
    'Unnamed: 0'])
79     marsmap['area'] = lat_band_area(marsmap.lat)/(2.*360)
80     marsmap = trim(marsmap,'lon',lonrange[0],lonrange[1])
81     marsmap = trim(marsmap, 'lat', latrange[0], latrange[1])
82
83     if notstring is None:
84         marsmap = marsmap[(marsmap.unit.str.contains(unit))]
85     else:
86         marsmap = marsmap[(marsmap.unit.str.contains(unit)) &
87                                         ~(marsmap.unit.str.contains(
    notstring))]
88     return marsmap
89
90
91 # Load isolated craters with topographic properties merged from robbins
```

```
    database
def load_isolated(latrange=(-90,90), lonrange=(-180,180), unit='',
    mindiam=1,maxdiam=100000,notstring = None):
    robbins = pd.read_csv('robbins_database.csv',
                usecols = ['CRATER_ID', 'DIAM_CIRCLE_IMAGE','
    DEPTH_RIMFLOOR_TOPOG','DEPTH_RIMHEIGHT_TOPOG','DEGRADATION_STATE'])
    isolated = pd.read_csv('isolated_robbins.csv').drop(columns=['
    Unnamed: 0'])
    isolated_robbins = pd.merge(isolated, robbins, how='left',left_on='
    crater_id',right_on='CRATER_ID')

    marsmap = load_marsmap(latrange, lonrange)

    latbins,lonbins = makebins(latrange, lonrange, dx=.5)

    isolated_robbins = gridmap(isolated_robbins, latbins, lonbins)
    marsmap = gridmap(marsmap, latbins, lonbins)

    isolated_merged = pd.merge(isolated_robbins,marsmap.iloc
    [:,[2,3,5,6]],how='left', on=['latbin','lonbin'])

    if notstring is None:
        isolated_masked = isolated_merged[(isolated_merged.unit.str.
    contains(unit))]
    else:
        isolated_masked = isolated_merged[(isolated_merged.unit.str.
    contains(unit)) &
                                          ~(isolated_merged.unit.str.
    contains(notstring))]

    data = pd.DataFrame({'lat':isolated_masked.lat,
                         'lon':isolated_masked.lon,
                         'mola':isolated_masked.smoothed,
                         'diam':isolated_masked.DIAM_CIRCLE_IMAGE,
                         'diam2':isolated_masked.diam,
                         'depth':isolated_masked.DEPTH_RIMFLOOR_TOPOG,
                         'rim':isolated_masked.DEPTH_RIMHEIGHT_TOPOG,
                         'deg':isolated_masked.DEGRADATION_STATE,
                         'slope':isolated_masked.avmax,
                         'rel_dep2':isolated_masked.rel_dep,
                         'rel_dep':isolated_masked.DEPTH_RIMFLOOR_TOPOG
    .values/(.357* (isolated_masked.DIAM_CIRCLE_IMAGE.values)**0.52)})

    data = trim(data, 'diam', mindiam, maxdiam)
    data = trim(data, 'lat',latrange[0],latrange[1])
    data = trim(data, 'lon',lonrange[0],lonrange[1])
    return data

def load_random_highlands(num=10**4,latrange=(-90,90), lonrange
    =(-180,180),units=['eNh','mNh','lNh']):
    Nh, marsmap = load_highlands(latrange, lonrange,units)
```

```
132
133     latbins,lonbins = makebins(latrange, lonrange, dx=.5)
134
135     uniform = uniform_sphere(latrange, lonrange, size=num)
136     uniform = pd.DataFrame({'lat':uniform.T[0],'lon':uniform.T[1]})
137
138     uniform = gridmap(uniform, latbins, lonbins)
139     marsmap = gridmap(marsmap, latbins, lonbins)
140
141     uniform_merged = pd.merge(uniform, marsmap.loc[:,['unit','latbin','
    lonbin']], how='inner', on = ['latbin','lonbin'])
142
143     return uniform_merged
144
145 # Load the robbins database at desired resolution, locations, units,
    etc.
146 def load_robbins(latrange=(-90,90), lonrange=(-180,180), unit='',
    mindiam=1,maxdiam=100000,notstring = None):
147     robbins = pd.read_csv('robbins_database.csv')
148     robbins = trim(robbins,'LATITUDE_CIRCLE_IMAGE',latrange[0],latrange
    [1])
149     robbins = trim(robbins, 'DIAM_CIRCLE_IMAGE',mindiam,maxdiam)
150     robbins = trim(robbins, 'LONGITUDE_CIRCLE_IMAGE',lonrange[0],
    lonrange[1])
151
152     marsmap = load_marsmap(latrange, lonrange)
153
154     unmasked_robbins = pd.DataFrame({'lat': robbins.
    LATITUDE_CIRCLE_IMAGE.values,
155                          'lon': robbins.LONGITUDE_CIRCLE_IMAGE.values,
156                          'diam': robbins.DIAM_CIRCLE_IMAGE.values,
157                          'rel_dep':robbins.DEPTH_RIMFLOOR_TOPOG.values
    /(.357* (robbins.DIAM_CIRCLE_IMAGE.values)**0.52),
158                          'deg': robbins.DEGRADATION_STATE.values})
159
160     latbins,lonbins = makebins(latrange, lonrange, dx=.5)
161
162     unmasked_robbins = gridmap(unmasked_robbins, latbins, lonbins)
163     marsmap = gridmap(marsmap, latbins, lonbins)
164
165     robbins_merged = pd.merge(unmasked_robbins,marsmap.iloc
    [:,[2,3,5,6]],how='left', on=['latbin','lonbin'])
166
167     if notstring is None:
168         robbins_masked = robbins_merged[(robbins_merged.unit.str.
    contains(unit))]
169     else:
170         robbins_masked = robbins_merged[(robbins_merged.unit.str.
    contains(unit)) &
171                                         ~(robbins_merged.unit.str.
    contains(notstring))]
```

```
172
173     return robbins_masked
174
175 def load_highlands(latrange=(-90,90), lonrange=(-180,180),units=['eNh',
    'mNh','lNh']):
176     Nh = pd.concat([load_robbins(latrange, lonrange, unit = name,
    notstring = 'Nhm') for name in units])
177     marsmap = pd.concat([load_marsmap(latrange, lonrange, unit = name,
    notstring = 'Nhm') for name in units])
178
179     return Nh, marsmap
180
181 def get_binned_densities(Nh, marsmap, diam, bin_width = 2**0.5,
    quantity='lat', bins=np.arange(-90,90,15),latrange=(-90,90),
    lonrange=(-180,180)):
182     Nh = trim(Nh, 'diam', diam, bin_width*diam)
183     Nh = trim(Nh, 'lat', min(latrange), max(latrange))
184     Nh = trim(Nh, 'lon', min(lonrange), max(lonrange))
185
186     marsmap = trim(marsmap, 'lat', min(latrange), max(latrange))
187     marsmap = trim(marsmap, 'lon', min(lonrange), max(lonrange))
188
189     Nh['bin'] = pd.cut(Nh[quantity], bins)
190     marsmap['bin'] = pd.cut(marsmap[quantity],bins)
191
192     grouped_map = marsmap.groupby('bin')
193
194     counts = pd.DataFrame(Nh.bin.value_counts(sort=False))
195     areas = grouped_map.agg({'area':'sum'})
196
197     return counts, areas
198
199
200 def degdens(testmap, craters, dx,latrange=(-90,90), lonrange=(-180,180)
    ,diam=4,bin_width = 4):
201     latbins, lonbins = makebins(latrange, lonrange,dx)
202
203     testmap = trim(testmap,'lat',min(latrange),max(latrange))
204     testmap = trim(testmap,'lon',min(lonrange),max(lonrange))
205
206     craters = trim(craters,'lat',min(latrange),max(latrange))
207     craters = trim(craters,'lon',min(lonrange),max(lonrange))
208     craters = trim(craters,'diam',diam,bin_width*diam)
209
210     testmap = gridmap(testmap,latbins,lonbins)
211     craters = gridmap(craters,latbins,lonbins)
212
213     craters['count'] = 1
214     craters['isdeg'] = craters.deg <= 2
215
216     grp_craters = craters.groupby(['latbin','lonbin'])
```

```
    aggd_craters = grp_craters.agg({'rel_dep':'mean', 'count':'sum', '
    isdeg':'sum'})

    grp_map = testmap.groupby(['latbin','lonbin'])
    aggd_map = grp_map.agg({'area':'sum', 'mola':'mean'})

    data = pd.merge(aggd_map, aggd_craters, how='left', left_index =
    True, right_index = True)
    data['dens'] = data['count'].values/data['area'].values
    data['frac'] = data['isdeg'].values/data['count'].values

    return data


def binned_degdens(testmap, craters, dx,latrange=(-90,90), lonrange
    =(-180,180),bins = (2**(0.5*np.arange(13)))):
    return [degdens(testmap,craters,dx,latrange,lonrange,bins[i],bins[i
    +1]/bins[i]) for i in range(len(bins)-1)]

# Take arrays of lat and long and format it for two-point functions
def format_lat_lon(lat, lon):
    return np.vstack([lat,lon]).T


# Compute the Landy-Szalay estimate of the two point correlation
    function
def angular_two_point(x, x_R, bins):
    KDT_D = BallTree((np.pi/180)*x, metric='haversine') # data tree
    KDT_R = BallTree((np.pi/180)*x_R, metric='haversine') # random tree

    counts_DD = KDT_D.two_point_correlation((np.pi/180)*x, (np.pi/180)*
    bins) # data to data
    counts_RR = KDT_R.two_point_correlation((np.pi/180)*x_R, (np.pi
    /180)*bins) # random to random
    counts_DR = KDT_R.two_point_correlation((np.pi/180)*x, (np.pi/180)*
    bins) # random to data

    # Take differences to get in-bin counts
    DD = np.diff(counts_DD)
    RR = np.diff(counts_RR)
    DR = np.diff(counts_DR)


    r = float(len(x_R))
    n = float(len(x))

    w3 = ( (r*(r-1)*DD) / (n*(n-1)*RR) ) - ( 2*((r-1)*DR) / (n*RR) ) +
    1
    w1 = DD/RR - 1.
    return w3

```

```
259
260 # Compute bootstrapped results from angular_two_point
261 def boot_angular(x,nsamples,bins,x_R = None,nboots=500):
262     results = np.zeros((nboots, len(bins)-1))
263
264     if x_R is None:
265         lat = x.T[0]
266         lon = x.T[1]
267         x_R = uniform_sphere( (min(lat), max(lat)), (min(lon), max(lon)
    ), size = len(x))
268
269     for i in range(nboots):
270         #print i
271         results[i] = angular_two_point(resample(x, n_samples = nsamples
    ),
272                 resample(x_R, n_samples = nsamples), bins=bins)
273
274     return results
275
276 # Summarize results from boot_angular
277 def boot_summarize(x,nsamples,bins,x_R = None,nboots = 100):
278     results = boot_angular(x, nsamples, bins, x_R, nboots)
279     means = np.array([np.mean(x) for x in results.T])
280     errs = np.array([2*np.std(x) for x in results.T])
281
282     return means, errs
283
284 # Extract topographic indices from a particular isolated crater file
285 def extractSlopeStats(filename):
286     # Load all of the radial profiles from csvs
287     profiles = pd.read_csv(filename)
288
289     # Get basic data
290     crater_id = profiles['CRATER_ID'][0]
291     diam = profiles['DIAM_KM'][0]
292     lat = profiles['LAT'][0]
293     lon = profiles['LONG'][0]
294
295
296     # Get the spacing between datapoints (assumed to be constant)
297     dx = profiles['DISTANCE'][1]-profiles['DISTANCE'][0]
298
299     # Group the data by bearing (separating each radial profile)
300     grouped = profiles.groupby('BEARING')
301
302     # Get x coordinate (assumed to be consistent across profiles)
303     x = grouped.get_group(0)['DISTANCE']
304
305     # Get list of unique bearings
306     bearings = profiles['BEARING'].unique()
307
```

```
    # Set initial stats for max wall, min rim slope, and max relief
    max_slopes = np.zeros(len(grouped))
    min_slopes = np.zeros(len(grouped))
    tot_relief = np.zeros(len(grouped))
    surf_elevs = np.zeros(len(grouped))

    # Loop through each profile
    for i in range(len(grouped)):

        # Get slopes from elevations and dx
        elev = np.array(grouped.get_group(bearings[i])['DETRENDED'])
        slope = np.gradient(elev,dx)

        # Calculate max and min slopes (only consider min slopes outside of crater rim) and relief
        max_slope = np.max(slope)
        max_el_loc = np.argmax(elev)
        min_slope = np.min(slope[max_el_loc:])
        relief = np.max(elev)-np.min(elev)
        rim = np.max(elev) - elev[-1]

        # Update slopes to get averages later
        max_slopes[i] = max_slope
        min_slopes[i] = min_slope
        tot_relief[i] = relief
        surf_elevs[i] = np.array(grouped.get_group(bearings[i])['MOLA'])[-1]

    # Get averages
    avmax = np.mean(max_slopes)
    avmin = np.mean(min_slopes)
    avrelief = np.mean(tot_relief)

    maxstd = np.std(max_slopes)
    minstd = np.std(min_slopes)
    reliefstd = np.std(tot_relief)

    # Return the data
    return [crater_id, diam, lat, lon, avmax,maxstd,avmin,minstd, avrelief,reliefstd, np.mean(surf_elevs)]

# Extract topographic indices for all isolated crater files in a folder
def getDataInFolder(foldername='./'):

    # Load file names in folder
    files = os.listdir(foldername)

    # Create list of column labels and initialize empty data frame
    cols = ['crater_id', 'diam', 'lat', 'lon', 'avmax','maxstd','avmin','minstd','avrelief','reliefstd','elev']
    data = pd.DataFrame(columns = cols)
```

```
355
356     # Loop through all the files in the folder
357     for filen in files:
358
359         # Check to make sure you are looking at a profile file, not a
    summary file
360         if filen.find('profiles') >= 0 and filen.find('summary') == -1:
361
362             # Calculate the crater's summary data
363             temp_data = extractSlopeStats(foldername + filen)
364
365             # Append the new data to our dataset
366             data = data.append(pd.DataFrame(data= [temp_data], columns=
    cols),ignore_index=True)
367
368     # Calculate relative depth using Tornabene scaling and return
    result
369     data.insert(1,'rel_dep',np.array(data['avrelief'])/(357*(np.array(
    data['diam']))**0.52))
370     return data
371
372 def smoothmap(maps,name, dist):
373     knn = RadiusNeighborsRegressor((np.pi/180)*dist, algorithm='
    ball_tree',metric='haversine')
374     X = format_lat_lon((np.pi/180)*maps.lat.values,(np.pi/180)*maps.lon
    .values)
375     Y = knn.fit(X,maps.mola.values).predict(X)
376     maps[name] = Y
377     return maps
```

Support file for 'agu_figs.py' and 'obliteration.py'. It does not need to be run on it's own, but it must be in the folder with the other scripts when they are run.

APPENDIX B

APPENDIX TO CHAPTER 3

We present supplementary info and figures, as well as the necessary scripts to reproduce the figures in Chapter 3 in the order that they should be run. Each individual script is annotated with its purpose and instructions for use (text below the code blocks). Some code blocks extend for several pages, as noted by the line numbering. We note that the scripts are specific to the computing environment and directory structure in which they were run, and the code will likely not work "out of the box".

B.1 Supplementary Info

B.1.1 Data Validation

To validate the corrected Robbins database (Robbins and Hynek, 2012), we examined de-projected measurements to search for and identify any systematic inter-analyst error. To do so, we divided the Robbins database into two-dimensional ellipticity-diameter bins, where ellipticity bins had a minimum value of 1.1 and width 0.1, and diameter bins had a minimum value of 5 km and $\sqrt{2}$ scaled widths. We randomly sampled up to 10 craters from each two dimensional ellipticity-diameter bin in the updated database (some bins contained fewer than 10 craters). We compiled a set of 563 craters spanning a wide range of ellipticities, diameters, degradation states, and latitudes. We independently retraced these craters, removed first order projection effects, and fit ellipses to them using a direct non-linear least squares procedure (following Fitzgibbon et al., 1999 and Robbins and Hynek, 2012).

We compared our measured ellipticities and orientations to those measured by Robbins and Hynek (2012) and reported in the correction. The inter-analyst residuals (defined as the difference between the values measured by Robbins and Hynek (2012) and our re-measured values for each crater) had both a non-zero mean and a non-zero skewness, even after filtering out the most degraded class of craters (degradation state 1 in Robbins and Hynek, 2012).

To assess whether these residuals can be attributed to random error, we resampled the residuals with replacement 10,000 times to produce a bootstrapped ensemble of equally likely residual distributions. For each resampled population, we calculated the residual means and skewnesses for both ellipticity and major-axis orientation. Histograms of the bootstrapped means and skewnesses show that the inter-analyst residuals for both ellipticity and orientation have means and skewnesses that are not significantly different from zero (Figure B.3). We concluded that for all craters other than the most degraded class, measurements of ellipticity and major-axis orientation show no systematic inter-analyst error.

Restricting this analysis to craters with modest ellipticities < 1.3 (as this is the region in which most of our final data lies), we found that orientation residual means, orientation residual skewness, and ellipticity residual skewness are still not significantly different from 0. While the ellipticity residuals showed a slight positive skewness, this only affects the acceptance/rejection of a crater for our analysis and does not systematically alter our orientation PDF. For craters with modest ellipticities, we found that the orientation residuals are roughly normally distributed with a standard deviation of 5°. Thus, we conclude that the Robbins database (Robbins and Hynek, 2012) provides a suitable constraint on our model with no systematic inter-analyst error and well quantified random inter-analyst error.

B.1.2 Model Validation

We validated our forward model by injecting artificially simple impactor populations and confirming that the resultant elliptic crater orientations and latitudes were consistent with the expected outcome. In particular, we injected impactors only from the orbit plane and varied the obliquity. At 0° obliquity, all elliptic craters were perfectly E–W oriented and located at the equator. At 90° obliquity, all elliptic craters were perfectly N–S oriented and distributed uniformly in latitude. We performed analogous tests with impactors coming from a plane inclined 90° with respect to the orbit plane and found consistent results. We also injected impactors with isotropic velocity vectors and found that the resultant orientations

were uniformly distributed and invariant with obliquity. Further, in the isotropic case the number of craters dropped off sinusoidally with latitude (uniform crater density in latitude), independent of obliquity choice. We also confirmed that the effects of gravity focusing were properly accounted for by both visual inspection of impactor velocity vectors and checking that impactor angular momentum relative to Mars is conserved. Finally, we confirmed that the fraction of craters in our model, $\sim 5\%$, that are elliptic is consistent with the observed fraction in the Robbins and Hynek (2012) database.

B.2 Supplementary Figures

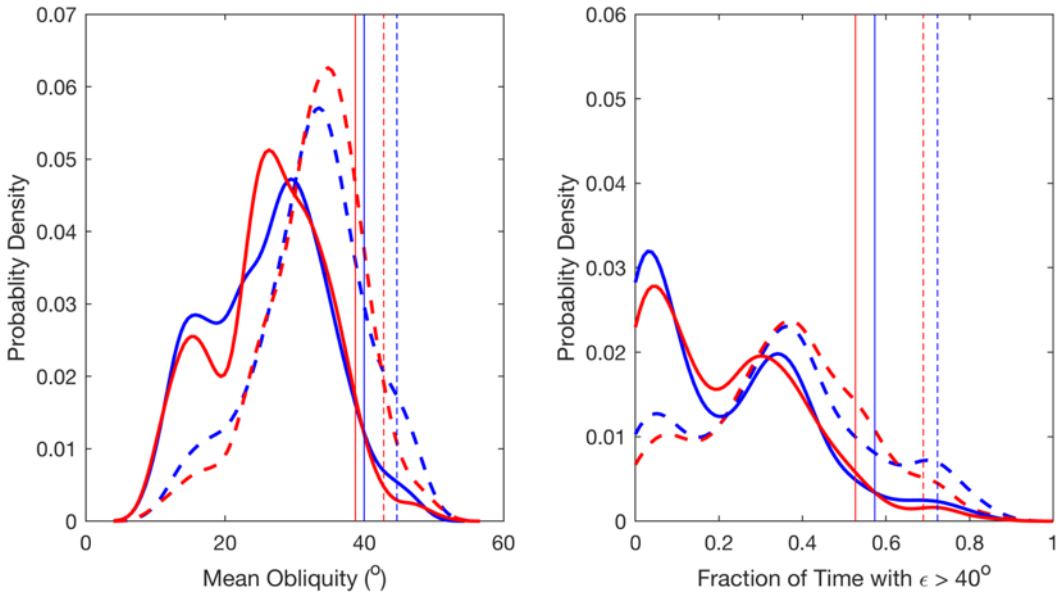

Figure B.1: Ellipticity Sensitivity Test Summary Statistics. Analogous to Figure 3.9 but fitting the model only to craters with ellipticity > 1.2.

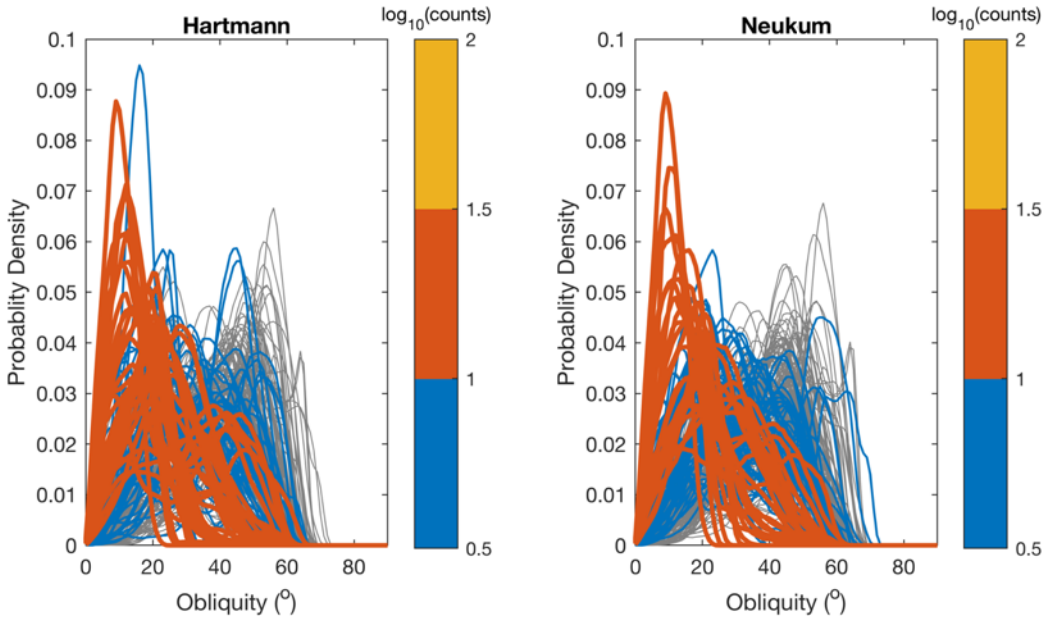

Figure B.2: Ellipticity Sensitivity Test Obliquity History Likelihoods. Analogous to Figure 3.8 but fitting the model only to craters with ellipticity > 1.2.

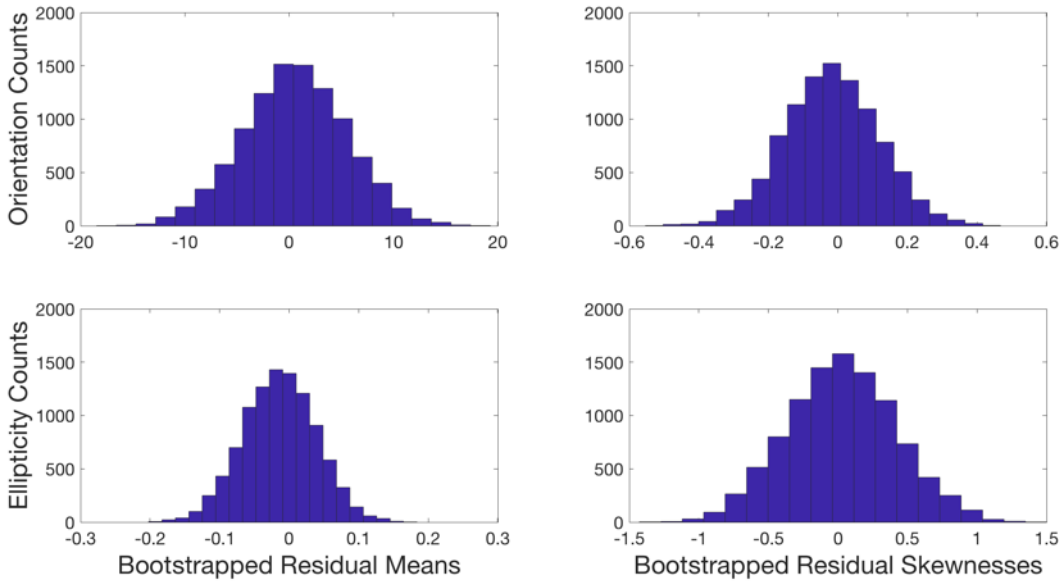

Figure B.3: Ellipticity and Orientation Inter-Analyst Variability. Bootstrapped residual means (left) and skewnesses (right) for major axis orientation (top) and ellipticity (bottom). In all cases, the inter-analyst residuals can be attributed to randomness.

B.3 Code and Reproducibility

Code B.1: make_small_in_no_clones.m

```
load rawmpcdata;

mco = (1+e).*a > 0.85*(1.52366231) & (1-e).*a < 1.15*(1.52366231) & Opp
    >1 & H <16;

orbels = [a(mco) e(mco) Incl(mco) Peri(mco) Node(mco) M(mco) zeros(sum(
    mco),3)];

fid=fopen('mco_small.in','wt');

for l = 1:sum(mco)

    fprintf(fid,'%-10s%s\n%-9.4f%-9.4f%-9.4f%-9.4f%-9.4f%-9.4f %s\n',
    ...
              strcat('mc',num2str(l)), ...
              'ep=2457600.5',orbels(l,1:6),num2str(int8(orbels(l,7:9))))
    ;


end
```

Produces the 'small.in' parameter file for `mercury6` n-body runs from Minor Planet Center data. 'small.in' contains the initial conditions for all the small bodies (asteroids) in the n-body simulation.

Code B.2: mercurypar

```
#!/bin/bash

template=$1
mco_small=$2
b=$3
indexfile=$4  # The function doesn't require this unless we're using the alternative method for extracting orbital elements (see below)
              #  But it is included for convenience
jobindex=$5
# Extract the number from $jobindex
j=$(echo ${jobindex} | awk -F_ '{print $3}')

# If we are going to run a simulation that includes ALL of the bodies in ${mco_small}, we can take advantage of the fact that we have
#  previously extracted the small body index names sequentially from ${indexfile}
#  and copy the orbital elements of those bodies into the small body input file for each job.

# The following command will seem cryptic if you're not used to using AWK so here is some explanation:
# -v j=$j -v b=$b # AWK has its own way of parsing shell variables. We use the -v flag to precede variable assignments for AWK
# The single-quoted section contains the instructions to AWK, separated by semicolons
# NR<6 {print} # The first instruction tells AWK to print row numbers less than 6 (NR is an AWK variable)
# NR> (5+2*((j-1)*b)) && NR<=((5+2*((j-1)*b)+2*b)) # Next, print row numbers that are > the first expression and <= the second expression
#   This looks complicated, but it's actually just stepping through the file 2*$b lines at a time (each body's orbital elements are split over 2 lines)
#   The first expression defines the starting line as a multiple of $j (offset by the assumed number of header rows, 5)
#   The second expression is just the initial expression + 2*$b
# ${mco_small} # The input file
# > ${jobindex}/small.in # Direct the results to the small.in file (required by Mercury) for the current job

awk -v j=$j -v b=$b 'NR<6 {print};NR> (5+2*((j-1)*b)) && NR<=((5+2*((j-1)*b)+(2*b)))' ${mco_small} > ${jobindex}/small.in


# If ${indexfile} contains only a subset of the bodies in ${mco_small} then you should comment out the preceding call to AWK and use the following code block instead
#  in order to extract orbital elements of the small bodies from ${mco_small}
# The following loop is slower than the AWK one-liner above by a factor of ~$b and is less concise but has the advantage of being more
```

```
   general
# Rather than striding through ${mco_small} and gathering orbital
   elements in groups of $b bodies, the following first extracts the
   list of small bodies for job part $j
#  and then searches for each body one at a time in ${mco_small} and
   extracts the corresponding orbital elements to a file

### ALTERNATIVE FOR EXTRACTING ORBITAL ELEMENTS FROM ${mco_small} ###
## Extract the small body index names included in job part $j and write
    them to a file in the corresponding subdirectory
# awk -v j=$j -v b=$b 'NR>((j-1)*b) && NR<=(((j-1)*b)+b)' ${indexfile}
   > ${jobindex}/mcindex
# ## Loop over each line in ${jobindex}/mcindex and search for lines in
    ${mco_small} that match
# for i in $(cat ${jobindex}/mcindex); do
#   ## For any line in the input file that contains a string similar to
    $mcindex, print it and the line immediately following
#   awk -v mcindex=$i 'NR<6 {print}; $0 ~ mcindex {print;getline;print
   }' ${mco_small} > ${jobindex}/small.in
# done



# Copy the contents of the template directory (named "template" in this
    case) to a new subdir named for the index of the current small body
cp ${template}/* ./${jobindex}/
cd ${jobindex}
# Run Mercury (Finally!)
./mercury6 > output_${jobindex}.log
```

Utility script that does not need to be run directly by the user. This script runs `mercury6` and is specific to the UChicago Midway computing environment in which it was run.

Code B.3: holo_parallel.sbatch

```
#!/bin/bash

#SBATCH --exclusive
#SBATCH --job-name=optimized_ellCrtr
#SBATCH --output=output.log
#SBATCH --error=errors.log
#SBATCH --time=99-11:59:59
#SBATCH --partition=kite
#SBATCH --nodes=2

# Send email notifications when job starts and ends
###SBATCH --mail-type=BEGIN,END
###SBATCH --mail-user=holo@uchicago.edu

# Load the module for GNU parallel
module load parallel


# This SBATCH script runs the Mercury6 M Body Simulation software
    across many compute cores in parallel such that the wall time is
    minimized.

### USER SPECIFIED VARIABLES ###
# Name of the file in the current working directory that contains the
    master catalog of orbital elements for the small bodies we wish to
    process
# This can either be an absolute path (safest option) or a path
    relative to the working directory from which this SBATCH script is
    called
mco_small=mco_small.in

# The location of a directory containing a template of the input
    parameters and a copy of the compiled mercury6 executable
# This can either be an absolute path (safest option) or a path
    relative to the working directory from which this SBATCH script is
    called
template=${PWD}/template

# The maximum number of small bodies that Mercury6 can accept in a
    single run
nmax=1899

# Name of file in the current working directory that contains a list of
     index names of the small bodies we wish to process
#indexfile=mcindex
# Alternatively we can generate our own $indexfile based on ALL of the
    bodies in ${mco_small}.
# For example:
#  Assuming the first 5 lines are part of the header and that NONE of
    the subsequent lines are commented out
```

```
awk 'NR>5 && $1 ~ "mc" {print $1}' ${mco_small} > mcindex
indexfile=mcindex
################################

### Determine the optimal number of small bodies to submit to each job based on the available cores and constrained by $nmax above
# Get total number of bodies from the index file
n=$(wc -l ${indexfile} | awk '{print $1}')

# Calculate the total number of cores that have been allocated for this job
c=$((SLURM_NNODES * SLURM_CPUS_ON_NODE))

# ##Debug only
# n=40
# c=2
# nmax=10

# Calculate how many bodies will be submitted to each core
#  Ideally, this is just n/c but if n is not evenly divisible by c, we add 1
if ((n%c > 0)); then
    b=$((n/c + 1))
else
    b=$((n/c))
fi

# Handle situation where $b as calculated above exceed the maxium number of bodies, $nmax, that mercury can handle per run
if ((b > nmax)) ; then
    echo "Number of bodies per core exceeds "$nmax
    b=${nmax}
  # Nested if/then to deal with remainder if n is not evenly divisble by nmax
  if ((n%b > 0 )); then
    c=$((n/b + 1))
  else
    c=$((n/b))
  fi
fi
echo Bodies per core is $b

# Use a C-style FOR loop to create a subdirectory for each job that we will eventually run
for (( j=1; j<=c; j++ )); do
   mkdir mco_part_${j}
   # Create a sort of "Index of an Index" that contains a list of the subdirectories we are creating
   # Store this list in a file that is named based on the SLURM job ID
   echo mco_part_${j} >> mco_jobindex_${SLURM_JOB_ID}
done
```

```
82
83
84 srun="srun --exclusive -N1 -n1"
85
86 parallel="parallel --joblog parallel_mercury.log --delay .2 -j $c"
87
88 $parallel "$srun ./mercurypar ${template} ${mco_small} $b ${indexfile}"
       :::: mco_jobindex_${SLURM_JOB_ID}
```

Script that splits the small bodies from 'small.in' into several, parallelized `mercury6` runs. This script is specific to the UChicago Midway computing environment in which it was run.

Code B.4: concat_imp_data.m

```
1  all_num_data = [];
2  all_name_data = [];
3  for i = 1:32
4      name = strcat('MARS',num2str(i),'.clo');
5      importeddata = importdata(name);
6
7      numdata = importeddata.data;
8      name_data = importeddata.textdata;
9      name_data(1:2,:) = [];
10     %name_data(:,1) = [];
11
12     all_num_data = [all_num_data;numdata];
13     all_name_data = [all_name_data;name_data];
14 end
15 noclones = all_num_data;
16 noclonenames = all_name_data;
17
18 save noclones.mat noclones noclonenames
```

Simple script that concatenates 'MARS.clo' close-encounter files from each of the parallelized runs. It must be run in a directory with all 32 'MARSN.clo' files in the same directory, where N varies between 1 and 32 (in our case on the UChicago Midway Cluster - see line 3).

Code B.5: inclinationsandspeeds.m

```
% Pull the data from the file and find repeats of MCO's
load('noclones.mat');
load('brightnesses.mat');

MARS = noclones;
names = noclonenames;
[~,ia,~] = unique(names(:,2),'legacy');
%Pull out the numerical data
ca = MARS(ia, 1);
x1 = MARS(ia, 2:4);
v1 = MARS(ia, 5:7);
x2 = MARS(ia, 8:10);
v2 = MARS(ia,11:13);
%Set variables for physical constants
G = 6.67408e-11; %grav constant in m^3 kg^-1 s^-2
R = 3.3895e6; %radius of mars in m
M = 6.4171e23; %mass of mars in kg

len = length(x1);
inclinations = zeros(len,1);
speeds = zeros(len,1);
for i = 1:len
    tempname = names{i};
    tempname1 = tempname(3:end-1);
    idnum = str2num(tempname1);

    if strcmp(tempname,'') == 0 && strcmp(tempname,'Object') ==0
        if mags(idnum) <= 14
            r = x1(i,:);
            rdot = v1(i,:);
            h = cross(r,rdot); %get the angular momentum
            hhat = h/norm(h);
            vel = v2(i,:) - v1(i,:); %get deltav
            speeds(i) = 1.731e6*norm(vel);
            vhat = vel/norm(vel);
            theta = acos(dot(hhat,vhat)); %get angle between h and v
            inclinations(i) = theta - pi/2; %save inclination
        else
            speeds(i) = NaN;
            inclinations(i) = NaN;
        end
    end
end
save('14mag_imp_info.mat','inclinations','speeds');
```

Parses the concatenated 'MARS.clo' file and produces the inclinations and speeds of Mars close encounters. The output file, '14_mag_imp_info.mat' is the starting point for the novel portion of our work: the obliquity pipeline.

Code B.6: get_pois.m

```
% This is the first script in Sam Holo's forward model for the effect of
% obliquity on elliptic crater orientations. The input file is name
% '14mag_imp_info' and contains an ensemble of encounter inclinations and
% speeds from n-body output. The output of this script is an ensemble of
% elliptic crater locations and diameters, as well as impactor velocity
% vectors at the time of impact and the impact angle. This output can be
% ingested and processed by apply_obliquity.m

%Set variables for physical constants
G = 6.67408e-11; %grav constant in m^3 kg^-1 s^-2
R = 3.3895e6; %radius of mars in m
M = 6.4171e23; %mass of mars in kg
vesc = 5027; % escape velocity in m/s
g = 3.71; % acceleration due to gravity in m/s^2

% Load impact info file - This needs two values: encounter
% inclinations and speeds from n-body output
load('14mag_imp_info', 'inclinations', 'speeds');

% Set parameters for the size frequency distribution
% NOTE: the SFD parameters have been tuned for a particular impactor
% population, this will NOT immediately translate to different populations
lmin = 21;
alpha = 0.65;
n = 5e4;  %%%%%% NOTE: set sample size here, this is too large %%%%%%

% Pre-assign random numbers and place for impact info
[speeds,id] = datasample(speeds,n);
inclinations = inclinations(id);
impactinfo = zeros(n,9);
randos = rand(n,4);

% Loop through each of the seeded inclination-speed pairs
for i = 1:n
    % set the impact parameters
    speed = speeds(i);
    tau = R*sqrt(1 + (2*G*M)/(R*speed*speed));
    inc = inclinations(i);

    % Sample from our assumed SFD and apply crater diameter scaling prior
    % to correction for impact angle
    prob = randos(i,4);
    imp_diam = lmin*(prob)^(1/(-1*alpha));
    d90 = 1.161*(g^(-0.22))*(speed^(0.44))*(imp_diam^(0.78));
```

```
45
46      % Keep track of progress in the loop
47      if mod(i,10000) == 0
48         disp(i);
49      end
50
51      % Calculate randomly generated parameters as described in Lefeuvre
52      % and Wieczorek (2008)
53
54      % Calculate the critical angle from cratering efficiency
55      % Later we will "flag" if the generated crater is elliptical or not
56      theta_c = 45*(d90/imp_diam)^(-0.52) + 77*(d90/imp_diam)^(-1.85);
57
58
59      % Here we create impacts with angles < 45 degrees
60      bsq = (tau^2)*(0.5 + 0.5*randos(i,1));
61      b = sqrt(bsq);
62      theta = acos(b/tau);
63      del = randos(i,2)*2*pi;
64      phi = randos(i,3)*2*pi;
65
66
67      %semi major axis of hyperbolic orbit
68      a = G*M/(speed^2);
69
70      %eccentricity
71      ecc = sqrt(1 + (b^2)*(speed^4)/ ((G^2)*(M^2)) );
72
73      %cosine and sine of true anomaly at launch point
74      cinf = -1/ecc;
75      sinf = -1*sqrt(1 - (cinf^2));
76
77      %cosine and sine of true anomaly at impact
78      cimp = (((a/R)*(ecc^2 - 1))-1)/ecc;
79      simp = -1*sqrt(1 - (cimp^2));
80
81
82      %calculate impact location in projectile coordinates
83      yi = -R*(cimp*cinf + simp*sinf);
84      xi = R*(simp*cinf - cimp*sinf);
85      zi = 0;
86      pos = [xi;yi;zi];
87      rotangle = pi/2 + theta;
88
89      % Calculate impact velocities from momentum conservation
90      speed = sqrt((speed)^2 + vesc^2);
91      vimp = speed*[cos(rotangle),-1*sin(rotangle),0;
92          sin(rotangle),cos(rotangle),0;
93          0,0,1]*pos/norm(pos);
94
95      % rotatation matrix for the effect of impact argument
```

```
96      cd = cos(del);
97      sd = sin(del);
98      Mdel = [cd,0,-1*sd; 0,1,0; sd, 0, cd];
99
100     % rotatation matrix for the effect of impactor inclination
101     ci = cos(inc);
102     si = sin(inc);
103     Minc = [1,0,0;0,ci,si;0,-1*si,ci];
104
105     % rotatation matrix for the effect of randomized precessional
        season
106     sphi = sin(phi);
107     cphi = cos(phi);
108     Mprec = [cphi,-1*sphi,0;sphi,cphi,0;0,0,1];
109
110     % update position and velocity by applying rotations
111     pos = (Mprec*(Minc*(Mdel*pos)));
112     vimp = (Mprec*(Minc*(Mdel*vimp)));
113
114     % Store position and velocity vectors, along with impact angles
115     impactinfo(i,1:6) = [pos;vimp]';
116 %     if rad2deg(theta) > theta_c
117 %         theta = -1;
118 %     end
119     impactinfo(i,7) = theta;
120     impactinfo(i,9) = deg2rad(theta_c);
121
122     % Correct for the effect of impact angle in crater diameter and
        store
123     crater_diam = d90*(sin(theta)^(1/3))/1000; % Remember scaling is in
        meters!
124     impactinfo(i,8) = crater_diam;
125 end
126
127 impactinfo = impactinfo(impactinfo(:,7) < impactinfo(:,9), :);
128 % Save the data
129 newfile = strcat('14mag_pois');
130 save(newfile, 'impactinfo','-v7.3');
```

Takes close encounter inclinations and speeds from '14_mag_imp_info.mat' and producing an ensemble of 50 thousand elliptic craters on a hypothetical Mars with 0 obliquity. The ensemble is stored in data file '14mag_pois.mat'.

Code B.7: apply_obliquity.m

```
% This is the second script Sam Holo's forward model for the effect of
% obliquity on elliptic crater orientations. It takes the output ensemble
% from get_pois.m (get "pre-obliquity-impacts"), applies each integer
% degree obliquity to the ensemble, and saves the key parameters: latitude,
% diameter, and orientation of the elliptic craters.

% Set the diameter (in km) below which you throw out model craters
diam_cutoff = 4;

% Load the impact data from get_pois.m
load('14mag_pois.mat','impactinfo');

% Filter out craters that are too small for the analysis
R = 3.3895e6;
impactinfo = impactinfo(impactinfo(:,8)>= diam_cutoff,:);
len = length(impactinfo);

% Pre-allocate space for the centers/counts of the model output
latdata = zeros(len,91);
orientationdata = zeros(len,91);
diamdata = zeros(len,91);


% Loop through the possible values for obliquity
for i = 0:90

    % Set the obliquity NOTE: here we are working in degrees
    obl = i;

    % Loop through each elliptic-crater producing impact
    for j = 1:len

        % Define the obliquity rotation matrix
        cobl = cosd(obl);
        sobl = sind(obl);
        Mobl = [1,0,0;0,cobl,sobl;0,-1*sobl,cobl];

        % Apply the obliquity rotation to the position and velocity vectors
        pos = Mobl*impactinfo(j,1:3)';
        vimp = Mobl*impactinfo(j,4:6)';

        % Calculate latitude
        latdata(j,i+1) = abs(asind(pos(3)/norm(pos)));

        % Calculate the impact orientation by projecting northbound and
        % velocity vectors onto the planet's tangent plane
        poshat = pos/norm(pos);
```

```
        north = [0;0;R] - pos;
        northproj = north - dot(north,poshat)*poshat;
        trajectoryproj = vimp - dot(vimp,poshat)*poshat;
        if norm(northproj) ~= 0
            northproj = northproj/norm(northproj); %normalize
        end
        if norm(trajectoryproj) ~= 0
            trajectoryproj = trajectoryproj/norm(trajectoryproj); %
   normalize
        end
        azimuth = acosd(dot(northproj,trajectoryproj));
        azimuth(azimuth > 90) = 180-azimuth;
        orientationdata(j,i+1) = azimuth;
        diamdata(j,i+1) = impactinfo(j,8);

    end

    % Display progress
    disp(i);

end

% Save the data
newfile = 'obliquity_predictions_4.mat';
save(newfile,'latdata','orientationdata','diamdata');
```

Takes ensemble of 50 thousand elliptic craters on a hypothetical Mars with 0 obliquity, from '14mag_pois.mat', and creates 90 copies of that ensemble, each with an obliquity applied, ranging from 1 to 90 degrees. The latitudes, orientations, and diameters of the ensemble craters are stored in 'obliquity_predictions_4.mat'.

Code B.8: debiased_pred.m

```
% This is the third script Sam Holo's forward model for the effect of
% obliquity on elliptic crater orientations. I briefly note that it is
% actually a function file that is designed to be called many times for
% embarrissingly parallel computations on midway. The first parameter, num,
% is an arbitrary label for which of our generated obliquity pdf's the
% function should be sampling from. The second parameter indicates whether
% we are using the Neukem or Hartmann chronologies. This function loads the
% output from the apply_obliquity script, as well as a database of craters
% (these are actual craters on mars whose latitude-diameter distribution we
% want to match in our predictions) and obliquity histograms. NOTE: the
% crater database and obliquity histograms are NOT relevant to noachian
% crater studies. They apply only to late-Hesperian onward terrains.

function [] = debiased_pred(num, ishart)

    % Load the requisite data as described above
    load('obliquity_predictions_4.mat','orientationdata','latdata','diamdata');
    load('latehesperian_4test.mat');
    load('obliquity_hists.mat','neuk','hart');

    % Store the crater database in a list of "reference" values
    reflats = crater_lats;
    refdiams = crater_diams;
    refages = crater_max_age_bins;
    refors = crater_ors;

    % Clear up some memory for good measure
    clear crater_lats crater_diams crater_max_age_bins

    % Get the num'th histogram in either the hartmann or neukem system.
    if ishart==1
        oblhist = hart(num,:,:); %#ok<NODEF>
    else
        oblhist = neuk(num,:,:);%#ok<NODEF>
    end

    iterations = 1000;
    pred_ors = zeros(iterations, length(refors));
    boot_ors = zeros(iterations, length(refors));
    ksstats = zeros(iterations,1);

    for i = 1:iterations
        % Sample the latitude, diameter, and underlying geologic unit
        % age from the "reference" craters
```

```
45          [templat, index] = datasample(reflats,length(reflats));
46          tempdiam = refdiams(index);
47          tempage = refages(index);
48          tempor = refors(index);
49
50          for j = 1:length(reflats)
51              % Randomly sample from the obliquity histograms. The first
52              % line in this chunk of code ensures that you consider the
53              % histogram of obliquities since the emplacement of the
54              % geologic unit on which the reference crater lies.
55              tempoblhist = oblhist(1,:,tempage(j));
56              temphistcumsum = cumsum(tempoblhist);
57              temphistcdf = temphistcumsum./temphistcumsum(end);
58              [~,obl] = min(abs(temphistcdf - rand));
59
60              % Calculate the differences in latitude and diameter
    between
61              % each ensemble model crater and the reference crater
62              laterror = abs(latdata(:,obl) - abs(templat(j)));%#ok<NODEF
    >
63              diamerror = abs(diamdata(:,obl) - tempdiam(j))/tempdiam(j);
     %#ok<NODEF>
64
65              % Restrict the data to the ensemble with the obliquity
    sampled
66              % above (to within 1 degree)
67              data = orientationdata(:,obl); %#ok<NODEF>
68
69              % Find the ensemble model craters that are "close" to the
70              % reference crater
71              restricted_data = data(laterror < 2.5 & diamerror < .05);
72
73              % Sample from the "close" craters randomly
74              pred_ors(i,j) = datasample(restricted_data, 1);
75          end
76
77          boot_ors(i,:) = tempor;
78          [~, ~, teststat] = kstest2(pred_ors(i,:),tempor);
79          ksstats(i) = teststat;
80      end
81
82      % Find the minimum ksstat (this is our "best fit") and save the
83      % data/predictions associated with it
84      [~,ind] = min(ksstats);
85      best_pred = pred_ors(ind,:);
86      best_data = boot_ors(ind,:);
87
88      % Save the data. The if statements are just for maintaining
    conventions
89      % in file names. Presumably in any applications of this model, this
90      % section will need to be modified.
```

```
    if ishart == 1
        newfile = strcat('4hartpred_',num2str(num),'.mat');
    else
        newfile = strcat('4neukpred_',num2str(num),'.mat');
    end

    disp(num);
    save(newfile,'ksstats', 'best_pred','best_data');
end
```

Takes the obliquity-applied impacts from 'obliquity_predictions_4.mat' and performs the fitting algorithm and determines the frequency with which each obliquity history fits the data best. Must be run for $num \in [1, ..., 250]$ and $ishart \in [0, 1]$.

Code B.9: elliptic_final_plots.m

```
hart_stats = zeros(1000,250);
hart_preds = zeros(1502,250);
hart_data = zeros(1502,250);

neuk_stats = zeros(1000,250);
neuk_preds = zeros(1502,250);
neuk_data = zeros(1502,250);

load('obliquity_hists.mat')
hart_hists = hart(:,:,5);
neuk_hists = neuk(:,:,5);

hart_means = zeros(1,250);
hart_fracs = zeros(1,250);

neuk_means = zeros(1,250);
neuk_fracs = zeros(1,250);

for i = 1:250
    load(strcat('4hartpred_',num2str(i),'.mat'), 'best_data',...
        'best_pred', 'ksstats');
    hart_stats(:,i) = ksstats;
    hart_preds(:,i) = best_pred';
    hart_data(:,i) = best_data';

    temp_hist = hart_hists(i,:);
    hart_means(i) = sum(temp_hist.*(0:90)/sum(temp_hist));
    hart_fracs(i) = sum(temp_hist(41:end)/sum(temp_hist));

    load(strcat('4neukpred_',num2str(i),'.mat'), 'best_data',...
        'best_pred', 'ksstats');
    neuk_stats(:,i) = ksstats;
    neuk_preds(:,i) = best_pred';
    neuk_data(:,i) = best_data';

    temp_hist = neuk_hists(i,:);
    neuk_means(i) = sum(temp_hist.*(0:90)/sum(temp_hist));
    neuk_fracs(i) = sum(temp_hist(41:end)/sum(temp_hist));
end

%%%%% HEAT MAPS %%%%%
load('latehesperian_4test.mat');
diams = log10(crater_diams);
ors = crater_ors;
lats = crater_lats;

D = log10(4):.1:log10(32);
O = 5:1:85;
L = floor(min(lats)):(max(lats));
L = -90:90;
```

```
51
52 [dd, oo] = meshgrid(D,O);
53
54 fig1 = figure('color',[1 1 1]);
55 subplot(1,2,1);
56 [f, xi, bwd] = ksdensity([ors diams], [oo(:),dd(:)]);
57 contourf(oo, dd, reshape(log10(f/sum(f)),[length(O), length(D)]));
58 yticks(log10([4 8 16 32 64]));
59 yticklabels({'4','8','16','32', '64'});
60 set(gca,'fontsize',9);
61 xlabel('Azimuth (^o from due North)');
62 ylabel('Diameter (km)');
63 c = colorbar;
64 title(c,'log_{10}(PDF)');
65 axis([0 90 log10(4) log10(32)]);
66
67 subplot(1,2,2);
68 [oo, ll] = meshgrid(O,L);
69 [f, xi, bw] = ksdensity([ors lats], [oo(:),ll(:)]);
70 contourf(oo,ll,reshape(log10(f/sum(f)), [length(L), length(O)]));
71 set(gca,'fontsize',9);
72 xlabel('Azimuth (^o from due North)');
73 ylabel('Latitude (^o)');
74 c = colorbar;
75 title(c,'log_{10}(PDF)');
76 axis([0 90 -90 90]);
77
78 fig1.PaperUnits = 'centimeters';
79 fig1.PaperPosition = [0 0 19 9.5];
80 print(fig1,'FIG3','-dtiffn','-r500');
81
82 %%%%% OBLIQUITY PDFS %%%%%%
83 fig2 = figure('color',[1 1 1]);
84 [~,I] = min(hart_stats, [], 2);
85 hartI = I;
86 sub1 = subplot(1,2,1);
87 Colors = lines(3);
88 set(fig2,'colormap',Colors);
89 [N, ~] = histcounts(I,.5:250.5);
90 [~,sorted] = sort(N);
91 for i = sorted
92     temppdf = hart_hists(i,:)./sum(hart_hists(i,:));
93     counts = sum(I == i);
94     if counts >= 10^1.5
95         plot(0:90,temppdf,'color',Colors(floor(2*log10(counts)),:),'
    linewidth',2.5);
96     elseif counts >= 10
97         plot(0:90,temppdf,'color',Colors(floor(2*log10(counts)),:),'
    linewidth',2);
98     elseif counts >= 10^.5
99         plot(0:90,temppdf,'color',Colors(floor(2*log10(counts)),:),'
```

```
    linewidth',1);
    else
        plot(0:90,temppdf,'color',[.5 .5 .5]);
    end
    hold on
end
c = colorbar;
caxis([0.5, 2]);
set(gca,'fontsize', 9);
xlabel('Obliquity (^o)');
ylabel('Probablity Density');
title(c,'log_{10}(counts)');
title(sub1, 'Hartmann');
axis([0 90 0 .1]);

[~,I] = min(neuk_stats, [], 2);
neukI = I;
sub2 = subplot(1,2,2);
Colors = lines(3);
set(fig2,'colormap',Colors);
[N, ~] = histcounts(I,.5:250.5);
[~,sorted] = sort(N);
for i = sorted
    temppdf = neuk_hists(i,:)./sum(neuk_hists(i,:));
    counts = sum(I == i);
    if counts >= 10^1.5
        plot(0:90,temppdf,'color',Colors(floor(2*log10(counts)),:),'
    linewidth',2.5);
    elseif counts >= 10
        plot(0:90,temppdf,'color',Colors(floor(2*log10(counts)),:),'
    linewidth',2);
    elseif counts >= 10^.5
        plot(0:90,temppdf,'color',Colors(floor(2*log10(counts)),:),'
    linewidth',1);
    else
        plot(0:90,temppdf,'color',[.5 .5 .5]);
    end
    hold on
end
c = colorbar;
caxis([0.5, 2]);
set(gca,'fontsize', 9);
xlabel('Obliquity (^o)');
ylabel('Probablity Density');
title(c,'log_{10}(counts)');
title(sub2, 'Neukum');
axis([0 90 0 .1]);

fig2.PaperUnits = 'centimeters';
fig2.PaperPosition = [0 0 19 9.5];
print(fig2,'FIG8','-dtiffn','-r500');
```

```
147
148 %%% MEANS AND OVER 40 %%%
149 fig3 = figure('color',[1 1 1]);
150 sub1 = subplot(1,2,1);
151 [f, xi] = ksdensity(hart_means,'BandWidth', 2);
152 plot(xi,f,'b--','linewidth',1.5);
153 hold on
154 [f, xi] = ksdensity(neuk_means,'BandWidth', 2);
155 plot(xi,f,'r--','linewidth',1.5);
156 [f, xi] = ksdensity(hart_means(hartI),'BandWidth', 2);
157 plot(xi,f,'b','linewidth',1.5);
158 [f, xi] = ksdensity(neuk_means(neukI),'BandWidth', 2);
159 plot(xi,f,'r','linewidth',1.5);
160
161 sortedpriorharts = sort(hart_means);
162 hartconfbound = sortedpriorharts(floor(length(sortedpriorharts)*.95));
163 plot([hartconfbound hartconfbound], [0 .07], 'b--');
164
165 sortedpriorneuks = sort(neuk_means);
166 neukconfbound = sortedpriorneuks(floor(length(sortedpriorneuks)*.95));
167 plot([neukconfbound neukconfbound], [0 .07], 'r--');
168
169 sortedpriorharts = sort(hart_means(hartI));
170 hartconfbound = sortedpriorharts(floor(length(sortedpriorharts)*.95));
171 plot([hartconfbound hartconfbound], [0 .07], 'b');
172
173 sortedpriorneuks = sort(neuk_means(neukI));
174 neukconfbound = sortedpriorneuks(floor(length(sortedpriorneuks)*.95));
175 plot([neukconfbound neukconfbound], [0 .07], 'r');
176 set(gca,'fontsize', 9);
177 xlabel('Mean Obliquity (^o)');
178 ylabel('Probablity Density');
179
180 sub2 = subplot(1,2,2);
181 [f, xi] = ksdensity(hart_fracs,0:.01:1,'BandWidth', .05);
182 plot(xi,f/sum(f),'b--','linewidth',1.5);
183 hold on
184 [f, xi] = ksdensity(neuk_fracs,0:.01:1,'BandWidth', .05);
185 plot(xi,f/sum(f),'r--','linewidth',1.5);
186 [f, xi] = ksdensity(hart_fracs(hartI),0:.01:1,'BandWidth', .05);
187 plot(xi,f/sum(f),'b','linewidth',1.5);
188 [f, xi] = ksdensity(neuk_fracs(neukI),0:.01:1,'BandWidth', .05);
189 plot(xi,f/sum(f),'r','linewidth',1.5);
190
191 sortedpriorharts = sort(hart_fracs);
192 hartconfbound = sortedpriorharts(floor(length(sortedpriorharts)*.95));
193 plot([hartconfbound hartconfbound], [0 .06], 'b--');
194
195 sortedpriorneuks = sort(neuk_fracs);
196 neukconfbound = sortedpriorneuks(floor(length(sortedpriorneuks)*.95));
197 plot([neukconfbound neukconfbound], [0 .06], 'r--');
```

```

sortedpriorharts = sort(hart_fracs(hartI));
hartconfbound = sortedpriorharts(floor(length(sortedpriorharts)*.95));
plot([hartconfbound hartconfbound], [0 .06], 'b');

sortedpriorneuks = sort(neuk_fracs(neukI));
neukconfbound = sortedpriorneuks(floor(length(sortedpriorneuks)*.95));
plot([neukconfbound neukconfbound], [0 .06], 'r');
set(gca,'fontsize', 9);
xlabel('Fraction of Time with \epsilon > 40^o');
ylabel('Probablity Density');

fig3.PaperUnits = 'centimeters';
fig3.PaperPosition = [0 0 10 9.5];
print(fig3,'FIG9','-dtiffn','-r500');

%%% DATA PLOT %%%
bootstraps = zeros(1000,81);
for i = 1:1000
    temp = datasample(crater_ors, length(crater_ors));
    [f, xi] = ksdensity(temp, (5:85),'BandWidth',5);
    bootstraps(i,:) = f/sum(f);
end

fig4 = figure('color', [1 1 1]);
sortedboots = sort(bootstraps, 1);
xx = [(5:85),fliplr(5:85)];
yy = [sortedboots(1,:),fliplr(sortedboots(end,:) )]';
patch(xx,yy,0,'FaceAlpha',0.3,'EdgeAlpha',0.3);
hold on
[f, xi] = ksdensity(crater_ors, (5:85),'BandWidth',5);
plot(5:85, f/sum(f),'LineWidth',1.5);
xlabel('Azimuth (^o from due North)');
set(gca,'fontsize',9);
ylabel('Probability Density');
axis([0 90 .002 0.025]);

box on
[f, xi] = ksdensity(hart_preds(:,245), (5:85),'BandWidth',5);
plot(5:85, f/sum(f),'k--','LineWidth',1.5);

legend('Full Bootstrapped Range','Raw Data','Example Fit');

fig4.PaperUnits = 'centimeters';
fig4.PaperPosition = [0 0 19 9.5];
print(fig4,'FIG4','-dtiffn','-r500');
```

Plots the results from the data-fitting procedure, producing Figures 3.3, 3.3, 3.8, and 3.9. Plotting scripts can be run in any order, as long as the 'debiased_pred.m' script has been run.

Code B.10: plot_ob_preds.m

```
fig1 = figure('color',[1 1 1]);
load('obliquity_predictions_4.mat')

for i = 15:15:75
    tempdata = orientationdata(:,i+1);
    [f, xi] = ksdensity(tempdata, [5 85], 'BandWidth',5);
    plot(xi, f, 'LineWidth', 1.5);
    hold on
end
set(gca, 'fontsize',9);
xlabel('Azimuth (^o from due North)');
ylabel('Probability Density');

legend('\epsilon = 15^o','\epsilon = 30^o','\epsilon = 45^o','\epsilon
   = 60^o','\epsilon = 75^o');

fig1.PaperUnits = 'centimeters';
fig1.PaperPosition = [0 0 14 9.5];
print(fig1,'FIG7','-dtiffn','-r500');
```

Plots Figure 3.7, showing predicted elliptic crater orientation PDF's as a function of a single obliquity. Plotting scripts can be run in any order, as long as the 'debiased_pred.m' script has been run.

Code B.11: impactor_plots.m

```
load('14mag_imp_info.mat');
load rawmpcdata;

mco = (1+e).*a > 0.85*(1.52366231) & (1-e).*a < 1.15*(1.52366231) & Opp
    >1 & H <16;

fig1 = figure('color',[1 1 1]);
subplot(1,2,1);
plot(a(mco),Incl(mco),'.');
hold on
axis([1 4 0 40]);
plot([1 4], [15 15], 'color','r','LineWidth',1.5);
set(gca,'FontSize',9)
xlabel('Semi-Major Axis (AU)');
ylabel('Orbital Inclination (^o)');

subplot(1,2,2);
[f, xi] = ecdf(rad2deg(abs(inclinations(orb_incs <= 15))));
plot(f, xi,'LineWidth',1.5);
hold on
[f, xi] = ecdf(rad2deg(abs(inclinations(orb_incs > 15))));
plot(f,xi,'LineWidth',1.5);
set(gca,'FontSize',9)
ylabel('Encounter Inclination (^o)');
xlabel('Cumulative Probability');
axis([0 1 0 90]);
legend('Orbital Inc. \leq 15^o', 'Orbital Inc. > 15^o','Location','
    southeast');

fig1.PaperUnits = 'centimeters';
fig1.PaperPosition = [0 0 19 9.5];
print(fig1,'FIG5','-dtiffn','-r500');
```

Plots the impactor orbital and encounter inclinations and velocities, producing Figure 3.5.

Plotting scripts can be run in any order, as long as the 'debiased_pred.m' script has been run.

APPENDIX C

APPENDIX TO CHAPTER 4

We present supplementary figures, as well as the necessary scripts to reproduce the figures in Chapter 4 in the order that they should be run. Each individual script is annotated with its purpose and instructions for use (text below the code blocks). Some code blocks extend for several pages, as noted by the line numbering. We note that the scripts are specific to the computing environment and directory structure in which they were run, and the code will likely not work "out of the box".

C.1 Code and Reproducibility

Code C.1: reduce.m

```
clear

centers = readmatrix('centers_2.csv');
centers = centers(:,1:3);
center_lons = centers(:,1);
center_lons(center_lons > 180) = center_lons(center_lons > 180) - 360;
centers(:,1) = center_lons;

craters = readmatrix('craters_2.csv');
craters = craters(:,1:3);
crater_lons = craters(:,1);
crater_lons(crater_lons > 180) = crater_lons(crater_lons > 180) - 360;
craters(:,1) = crater_lons;

embedded_craters = readmatrix('embedded_craters.xlsx');
embedded_craters = embedded_craters(:,1:2);

climate_fans = readmatrix('climate_fan_bearing_craters.xlsx');
climate_fan_lons = climate_fans(:,1);
climate_fan_lons(climate_fan_lons > 180) = ...
    climate_fan_lons(climate_fan_lons > 180) - 360;
climate_fans(:,1) = climate_fan_lons;


a = shaperead('yellows.shp');
fans = shaperead('fan_apices_mar16_craters.shp');
edwinlakes = shaperead('edwin_lakes.shp');
lakeslon = extractfield(edwinlakes,'CenterLong');
```

```
lakeslon(lakeslon > 180) = lakeslon(lakeslon > 180) - 360;
lakeslat = extractfield(edwinlakes,'CenterLati');

hascenter = zeros(length(a),1);
hasfans = zeros(length(a),1);
haslakes = zeros(length(a),1);
hasclimatefans = zeros(length(a),1);
hasembed = zeros(length(a),1);
areas = zeros(length(a),1);
counts = zeros(length(a),1);
ids = extractfield(a,'OBJECTID')';

for i = 1:length(a)
    % Determine the center crater for the unit and if it has fans
    dx = 1:(length(a(i).X)-1);
    centers_in = inpolygon(centers(:,1),centers(:,2),a(i).X(dx),a(i).Y(dx));
    if sum(centers_in) == 0
       center_distances = distance(centers(:,1),centers(:,2),...
           mean(a(i).X(dx),'omitnan'),mean(a(i).Y(dx),'omitnan'));
       [~,idx] = min(center_distances);
       centers_in(idx) = 1;
    end
    hascenter(i) = min(1,sum(centers_in));
    hasfans(i) = min(1,sum(inpolygon(extractfield(fans,'longitude'),...
        extractfield(fans,'latitude'),a(i).X(dx),a(i).Y(dx))));
    haslakes(i) = min(1,sum(inpolygon(lakeslon,...
        lakeslat,a(i).X(dx),a(i).Y(dx))));
    hasclimatefans(i) = min(1,sum(inpolygon(climate_fans(:,1),climate_fans(:,2),...
        a(i).X(dx),a(i).Y(dx))));
    hasembed(i) = min(1,sum(inpolygon(embedded_craters(:,1),embedded_craters(:,2),...
        a(i).X(dx),a(i).Y(dx))));


    % Store the lats/lons of the outline and make a grid
    outline_lons = a(i).X(dx);
    outline_lats = a(i).Y(dx);

    lon_grid_vals = linspace(min(outline_lons),max(outline_lons),100);
    lat_grid_vals = linspace(min(outline_lats),max(outline_lats),100);

    [finelon, finelat] = meshgrid(lon_grid_vals, lat_grid_vals);
    finelon = finelon(:);
    finelat = finelat(:);
    fine_in = inpolygon(finelon,finelat,a(i).X(dx),a(i).Y(dx));
    fineweight = cosd(finelat);


    % Determine which craters are on the unit
```

```
77      % centers_in==1 bug corrected in "clean" folder version 9/18/20
78      craters_in = inpolygon(craters(:,1),craters(:,2),a(i).X(dx),a(i).Y(
        dx));
79      temp_craters = craters(craters_in==1,:);
80
81      % Calculate r/R values for both the pixels and the craters
82      centerval = centers(centers_in == 1,:);
83      centerlon = centerval(1,1);
84      centerlat = centerval(1,2);
85      center_diam = centerval(1,3);
86
87      fine_rr = (3389.5)*(pi/180)*(2000/center_diam)*distance(finelon,...
88          finelat,centerlon,centerlat);
89      crater_rr = (3389.5)*(pi/180)*(2000/center_diam)*distance(
        temp_craters(:,1),...
90          temp_craters(:,2),centerlon,centerlat);
91
92      % ANNULUS CHECKS EDITED IN NEXT 3 LINES ONLY 10/7/20 - O.G. is
        fine_rr <= 2
93      areas(i) = a(i).SphArea_km*sum(fineweight(fine_rr >= 1 & fine_rr <=
        20 & fine_in == 1))/...
94          sum(fineweight(fine_in == 1));
95      counts(i) = length(crater_rr(crater_rr >= 1 & crater_rr <= 20));
96
97      % Plot results for sanity checks
98      plot(centerlon,centerlat,'ko','markersize',5);
99      hold on
100     scatter(finelon,finelat,[],fine_rr);
101     scatter(temp_craters(:,1),temp_craters(:,2),10,crater_rr,'filled');
102     colorbar
103
104     disp(i/length(a))
105 end
106
107  save data_annulus_check areas counts hascenter hasfans hasclimatefans
       hasembed haslakes ids
```

Parses crater counts, AHi unit shapefiles, and the global fans database. Stores final data for each AHi unit (number of craters on ejecta, whether or not it has fans or embedded craters, etc.). Currently, lines 93, 95, and 107 are set for the "annulus check" sensitivity test, in which we consider the full extent of the ejecta blanket. To restrict the data to within 2 times the radius of the central crater, replace the 20 with 2 on lines 93 and 95, and delete '_annulus_check' on line 107.

Code C.2: reduce_spatial_2.m

```
clear

centers = readmatrix('centers_2.csv');
centers = centers(:,1:3);
center_lons = centers(:,1);
center_lons(center_lons > 180) = center_lons(center_lons > 180) - 360;
centers(:,1) = center_lons;

craters = readmatrix('craters_2.csv');
craters = craters(:,1:3);
crater_lons = craters(:,1);
crater_lons(crater_lons > 180) = crater_lons(crater_lons > 180) - 360;
craters(:,1) = crater_lons;

embedded_craters = readmatrix('embedded_craters.xlsx');
embedded_craters = embedded_craters(:,1:2);

climate_fans = readmatrix('climate_fan_bearing_craters.xlsx');
climate_fan_lons = climate_fans(:,1);
climate_fan_lons(climate_fan_lons > 180) = ...
    climate_fan_lons(climate_fan_lons > 180) - 360;
climate_fans(:,1) = climate_fan_lons;


a = shaperead('yellows.shp');
fans = shaperead('may2020_fan_apices_foredwin.shp');
fan_elevs = extractfield(fans,'apex_eleva')';
edwinlakes = shaperead('edwin_lakes.shp');
lakeslon = extractfield(edwinlakes,'CenterLong');
lakeslon(lakeslon > 180) = lakeslon(lakeslon > 180) - 360;
lakeslat = extractfield(edwinlakes,'CenterLati');

hascenter = zeros(length(a),1);
unitlats = zeros(length(a),1);
mean_unit_fan_elev = zeros(length(a),1);
hasfans = zeros(length(a),1);
haslakes = zeros(length(a),1);
hasclimatefans = zeros(length(a),1);
hasembed = zeros(length(a),1);
areas = zeros(length(a),1);
counts = zeros(length(a),1);
ids = extractfield(a,'OBJECTID')';

for i = 1:length(a)
    % Determine the center crater for the unit and if it has fans
    dx = 1:(length(a(i).X)-1);
    centers_in = inpolygon(centers(:,1),centers(:,2),a(i).X(dx),a(i).Y(
   dx));
    if sum(centers_in) == 0
        center_distances = distance(centers(:,1),centers(:,2),...
```

```
50            mean(a(i).X(dx),'omitnan'),mean(a(i).Y(dx),'omitnan'));
51        [~,idx] = min(center_distances);
52        centers_in(idx) = 1;
53     end
54     hascenter(i) = min(1,sum(centers_in));
55     hasfans_temp = inpolygon(extractfield(fans,'longitude'),...
56         extractfield(fans,'latitude'),a(i).X(dx),a(i).Y(dx));
57     mean_unit_fan_elev(i) = mean(fan_elevs(hasfans_temp==1));
58     hasfans(i) = min(1,sum(hasfans_temp));
59     haslakes(i) = min(1,sum(inpolygon(lakeslon,...
60         lakeslat,a(i).X(dx),a(i).Y(dx))));
61     hasclimatefans(i) = min(1,sum(inpolygon(climate_fans(:,1),
   climate_fans(:,2),...
62         a(i).X(dx),a(i).Y(dx))));
63     hasembed(i) = min(1,sum(inpolygon(embedded_craters(:,1),
   embedded_craters(:,2),...
64         a(i).X(dx),a(i).Y(dx))));
65
66
67     % Store the lats/lons of the outline and make a grid
68     outline_lons = a(i).X(dx);
69     outline_lats = a(i).Y(dx);
70
71     unitlats(i) = mean(outline_lats);
72
73     lon_grid_vals = linspace(min(outline_lons),max(outline_lons),100);
74     lat_grid_vals = linspace(min(outline_lats),max(outline_lats),100);
75
76     [finelon, finelat] = meshgrid(lon_grid_vals, lat_grid_vals);
77     finelon = finelon(:);
78     finelat = finelat(:);
79     fine_in = inpolygon(finelon,finelat,a(i).X(dx),a(i).Y(dx));
80     fineweight = cosd(finelat);
81
82
83     % Determine which craters are on the unit
84     % centers_in==1 bug corrected in "clean" folder version 9/18/20
85     craters_in = inpolygon(craters(:,1),craters(:,2),a(i).X(dx),a(i).Y(
   dx));
86     temp_craters = craters(craters_in==1,:);
87
88     % Calculate r/R values for both the pixels and the craters
89     centerval = centers(centers_in == 1,:);
90     centerlon = centerval(1,1);
91     centerlat = centerval(1,2);
92     center_diam = centerval(1,3);
93
94     fine_rr = (3389.5)*(pi/180)*(2000/center_diam)*distance(finelon,...
95         finelat,centerlon,centerlat);
96     crater_rr = (3389.5)*(pi/180)*(2000/center_diam)*distance(
   temp_craters(:,1),...
```

```
97          temp_craters(:,2),centerlon,centerlat);
98
99      % ANNULUS CHECKS EDITED IN NEXT 3 LINES ONLY 10/7/20 - O.G. is
        fine_rr <= 2
100     areas(i) = a(i).SphArea_km*sum(fineweight(fine_rr >= 1 & fine_rr <=
        2 & fine_in == 1))/...
101         sum(fineweight(fine_in == 1));
102     counts(i) = length(crater_rr(crater_rr >= 1 & crater_rr <= 2));
103
104     % Plot results for sanity checks
105     plot(centerlon,centerlat,'ko','markersize',5);
106     hold on
107     scatter(finelon,finelat,[],fine_rr);
108     scatter(temp_craters(:,1),temp_craters(:,2),10,crater_rr,'filled');
109     colorbar
110
111     disp(i/length(a))
112 end
113
114  save data_spatial_2 areas counts hascenter hasfans hasclimatefans
       hasembed haslakes ids unitlats mean_unit_fan_elev
```

Analogous to 'reduce.m', but calls a newer version of the global fans database and stores information related to the latitude and and elevation of AHi units/fans.

Code C.3: infer.m

```
function [] = infer()
    % Load Data
    clear
    load human_to_reduced_data/data.mat areas counts hascenter hasfans ...
        hasclimatefans hasembed haslakes ids;

    % Set Constants
    max_time = 4;
    num_units = length(areas);
    t = (0:0.05:max_time);
    p = (0:0.01:1);
    exp_likelihood = zeros(length(p), length(t));
    [t_, p_] = meshgrid(t,p);

    for i = 1:length(p)
        for j = 1:length(t)
            log_likelihood_sum = 0;
            for k = 1:num_units
                [posterior, tc] = age_posterior(counts(k),areas(k),4.5);
                log_likelihood_sum = log_likelihood_sum +...
                    log10(sum(posterior.*step_likely(t(j),p(i),tc, hasfans(k))));

            end
            exp_likelihood(i,j) = log_likelihood_sum;
        end
        disp(i)
    end

    exp_likelihood(exp_likelihood == 0) = NaN;
    save stepdata_test t_ p_ exp_likelihood
end

function likelihood = step_likely(t_spike, p_max, x,hasfan)
    likelihood = 0.001 + (p_max-0.001)*(x >= t_spike);
    if hasfan == 0
       likelihood = 1-likelihood;
    end
end

function likelihood = slope_likely(t1,t2,p_max,x,hasfan)
    likelihood = interp1([-0.1,t1,t2,100], [0.001,0.001,p_max,p_max],x);
    if hasfan == 0
       likelihood = 1-likelihood;
    end
end

```

```
47 function [posterior, tc] = age_posterior(N,A,max_time)
48     % Set some constants
49     N1_ref = 5.84e-4;
50     N4_ref = 4.25e-5;
51 
52     % Define the prior and posterior functions
53     t = (0:0.01:max_time)';
54     tc = 0.5*(t(1:end-1) + t(2:end));
55     dens_t = (N4_ref/N1_ref)*(N1_ref*t + (3.79e-14)*(exp(6.93*t)-1));
56     prior = diff(dens_t);
57     likelihood = poisspdf(N,0.5*(dens_t(1:end-1) + dens_t(2:end))*A);
58 
59     % Define and renormalize the posterior
60     posterior = prior.*likelihood;
61     posterior = posterior./sum(posterior);
62 end
```

Computes the likelihoods for the pulse-formation model given data from each AHi unit. The data input can be changed on line 4 (e.g. to 'data_annulus_check.mat') to perform the sensitivity tests. If the input data is changed, one should remember to change the output data file name on line 30.

Code C.4: infer3.m

```
function [] = infer3()
    % Load Data
    clear
    load human_to_reduced_data/data.mat areas counts hascenter hasfans
    ...
        hasclimatefans hasembed haslakes ids;

    % Set Constants
    max_time = 4;
    num_units = length(areas);
    t = (0:0.1:max_time);
    dur = (0.001:0.1:max_time+0.001);
    p = (0:0.01:1);
    exp_likelihood = zeros(length(p), length(t),length(dur));
    [tt, pp, dd] = meshgrid(t,p,dur);

    for i = 1:length(p)
        for j = 1:length(t)
            for l = 1:length(dur)
                if t(j)+dur(l) <= max_time + 0.001
                    log_likelihood_sum = 0;
                    for k = 1:num_units
                        [posterior, tc] = age_posterior(counts(k),areas
    (k),4.5);
                        log_likelihood_sum = log_likelihood_sum +...
                            log10(sum(posterior.*slope_likely(t(j),t(j)
    +dur(l),p(i),tc,hasfans(k))));

                    end
                    exp_likelihood(i,j,l) = log_likelihood_sum;
                else
                    exp_likelihood(i,j,l) = NaN;
                end
            end
        end
        disp(i)
    end

    exp_likelihood(exp_likelihood == 0) = NaN;
    save slopedata_3 tt dd pp exp_likelihood
end

function likelihood = step_likely(t_spike, p_max, x,hasfan)
    likelihood = 0.001 + (p_max-0.001)*(x >= t_spike);
    if hasfan == 0
       likelihood = 1-likelihood;
    end
end

function likelihood = slope_likely(t1,t2,p_max,x,hasfan)
```

```
48      likelihood = interp1([-0.1,t1,t2,1000], [0.001,0.001,p_max,p_max],x
        );
49      if hasfan == 0
50         likelihood = 1-likelihood;
51      end
52  end
53
54  function [posterior, tc] = age_posterior(N,A,max_time)
55      % Set some constants
56      N1_ref = 5.84e-4;
57      N4_ref = 4.25e-5;
58
59      % Define the prior and posterior functions
60      t = (0:0.01:max_time)';
61      tc = 0.5*(t(1:end-1) + t(2:end));
62      dens_t = (N4_ref/N1_ref)*(N1_ref*t + (3.79e-14)*(exp(6.93*t)-1));
63      prior = diff(dens_t);
64      likelihood = poisspdf(N,0.5*(dens_t(1:end-1) + dens_t(2:end))*A);
65
66      % Define and renormalize the posterior
67      posterior = prior.*likelihood;
68      posterior = posterior./sum(posterior);
69  end
```

Computes the likelihoods for the prolonged-formation model given data from each AHi unit. The data input can be changed on line 4 (e.g. to 'data_annulus_check.mat') to perform the sensitivity tests. If the input data is changed, one should remember to change the output data file name on line 37.

Code C.5: infer_inject.m

```
function [] = infer_inject()
    % Load Data
    clear
    load human_to_reduced_data/data.mat areas counts hascenter hasfans ...
        hasclimatefans hasembed haslakes ids;

    % p = 0.5 for all cases.
    % 10xA has areas = 10*areas to simulate getting more data
    %areas = 10*areas;
    [counts,hasfans,sampletimes] = trunc_prior_sample(areas,1.5,3.54,0.5);

    % Set Constants
    max_time = 4;
    num_units = length(areas);
    t = (0:0.05:max_time);
    p = (0:0.01:1);
    exp_likelihood = zeros(length(p), length(t));
    [t_, p_] = meshgrid(t,p);

    for i = 1:length(p)
        for j = 1:length(t)
            log_likelihood_sum = 0;
            for k = 1:num_units
                [posterior, tc] = age_posterior(counts(k),areas(k),4.5);
                log_likelihood_sum = log_likelihood_sum +...
                    log10(sum(posterior.*step_likely(t(j),p(i),tc,hasfans(k))));

            end
            exp_likelihood(i,j) = log_likelihood_sum;
        end
        disp(i)
    end

    exp_likelihood(exp_likelihood == 0) = NaN;
    save stepdata_inject_15Ga_354trunc t_ p_ exp_likelihood sampletimes counts areas hasfans
end

function [samples,fans,sampletimes] = trunc_prior_sample(A,fan_time,max_time,p)
    % Set some constants
    N1_ref = 5.84e-4;
    N4_ref = 4.25e-5;

    % Define the prior
    t = (0:0.01:max_time)';
```

```
    tc = 0.5*(t(1:end-1) + t(2:end));
    dens_t = (N4_ref/N1_ref)*(N1_ref*t + (3.79e-14)*(exp(6.93*t)-1));
    prior = diff(dens_t);
    prior = prior/sum(prior);

    % Sample from prior for each yellow - truncate for hasfans == 1
    randos = rand(length(A), 2);
    samples = zeros(length(A), 1);
    sampletimes = zeros(length(A), 1);
    fans = zeros(length(A),1);
    for i = 1:length(A)
        cdf = cumsum(prior);
        temptime = min(tc(cdf >= randos(i,1)));
        sampletimes(i) = temptime;
        tempdens = (N4_ref/N1_ref)*(N1_ref*temptime + (3.79e-14)*(exp
   (6.93*temptime)-1));
        samples(i) = poissrnd(A(i)*tempdens);
        if temptime >= fan_time
            if randos(i,2) <= p
               fans(i) = 1;
            end
        end
    end
end

function likelihood = step_likely(t_spike, p_max, x,hasfan)
    likelihood = 0.001 + (p_max-0.001)*(x >= t_spike);
    if hasfan == 0
       likelihood = 1-likelihood;
    end
end

function [posterior, tc] = age_posterior(N,A,max_time)
    % Set some constants
    N1_ref = 5.84e-4;
    N4_ref = 4.25e-5;

    % Define the prior and posterior functions
    t = (0:0.01:max_time)';
    tc = 0.5*(t(1:end-1) + t(2:end));
    dens_t = (N4_ref/N1_ref)*(N1_ref*t + (3.79e-14)*(exp(6.93*t)-1));
    prior = diff(dens_t);
    likelihood = poisspdf(N,0.5*(dens_t(1:end-1) + dens_t(2:end))*A);

    % Define and renormalize the posterior
    posterior = prior.*likelihood;
    posterior = posterior./sum(posterior);
end
```

Computes the likelihoods for the pulse-formation model using synthetic data that is created

to the users specification. One can set p_{max} and τ_{form} on line 10. To perform the sensitivity test with large areas, one can simply un-comment line 9. One should remember to change the output data file name on line 30 to reflect the input parameters. Unlike 'infer.m', this script saves the randomly-generated data so it can be read by the prolonged-formation model inference script.

Code C.6: infer3_inject.m

```
function [] = infer3_inject()
    % Load Data
    clear

    load stepdata_inject_15Ga_4trunc_10xA areas counts hasfans
   sampletimes;

    % Set Constants
    max_time = 4;
    num_units = length(areas);
    t = (0:0.1:max_time);
    dur = (0.001:0.1:max_time+0.001);
    p = (0:0.01:1);
    exp_likelihood = zeros(length(p), length(t),length(dur));
    [tt, pp, dd] = meshgrid(t,p,dur);

    for i = 1:length(p)
        for j = 1:length(t)
            for l = 1:length(dur)
                if t(j)+dur(l) <= max_time + 0.001
                    log_likelihood_sum = 0;
                    for k = 1:num_units
                        [posterior, tc] = age_posterior(counts(k),areas
   (k),4.5);

                        log_likelihood_sum = log_likelihood_sum +...
                            log10(sum(posterior.*slope_likely(t(j),t(j)
   +dur(l),p(i),tc,hasfans(k))));

                    end
                    exp_likelihood(i,j,l) = log_likelihood_sum;
                else
                    exp_likelihood(i,j,l) = NaN;
                end
            end
        end
        disp(i)
    end

    exp_likelihood(exp_likelihood == 0) = NaN;
    save slopedata_3_inject_15Ga_4trunc_10xA tt dd pp exp_likelihood
   sampletimes counts areas hasfans
end

function likelihood = slope_likely(t1,t2,p_max,x,hasfan)
    likelihood = interp1([-0.1,t1,t2,1000], [0.001,0.001,p_max,p_max],x
   );
    if hasfan == 0
       likelihood = 1-likelihood;
    end
```

```
46 end
47
48 function [posterior, tc] = age_posterior(N,A,max_time)
49     % Set some constants
50     N1_ref = 5.84e-4;
51     N4_ref = 4.25e-5;
52
53     % Define the prior and posterior functions
54     t = (0:0.01:max_time)';
55     tc = 0.5*(t(1:end-1) + t(2:end));
56     dens_t = (N4_ref/N1_ref)*(N1_ref*t + (3.79e-14)*(exp(6.93*t)-1));
57     prior = diff(dens_t);
58     likelihood = poisspdf(N,0.5*(dens_t(1:end-1) + dens_t(2:end))*A);
59
60     % Define and renormalize the posterior
61     posterior = prior.*likelihood;
62     posterior = posterior./sum(posterior);
63 end
```

Computes the likelihoods for the pulse-formation model using synthetic data that is created to the users specification. Line 5 loads data output from 'infer_inject.m' in order to use the same randomly-generated synthetic data. One should remember to change the output data file name on lines 5 and 37 to reflect the input parameters.

Code C.7: fan_plots.m

```
clear all
load human_to_reduced_data/data.mat areas  hasembed hasclimatefans
    counts hasfans


load slopedata_3_inject_3Ga_4trunc

slope_like = 10.^exp_likelihood;

load stepdata_inject_3Ga_4trunc

step_like = 10.^exp_likelihood;
step_like(isnan(step_like)) = 0;
dt = 0.01;
dt2 = 0.05;
dt3 = 0.1;

form_times = 0:0.01:4.5;
posts = zeros(length(counts), length(form_times)-1);
posts2 = zeros(length(counts), length(form_times)-1);
likelihoods = zeros(length(counts), length(form_times)-1);

for i = 1:length(counts)
   [posterior, tc] = age_posterior(counts(i),areas(i),max(form_times));
   [~,likelihood,~] = age_prior(counts(i),areas(i),max(form_times));
   likelihoods(i,:) = cumsum(likelihood)/sum(likelihood);
   posts(i,:) = 1 - cumsum(posterior');
   posts2(i,:) = posterior';
end

fan_posts = posts(hasfans == 1,:);
fan_posts2 = posts2(hasfans == 1, :);
non_fan_posts = posts2(hasfans == 0, :);

fan_likelihoods = likelihoods(hasfans == 1,:);
non_fan_likelihoods = likelihoods(hasfans == 0,:);

embed_posts = posts(hasfans == 1 & (hasembed ==1 | hasclimatefans == 1)
    , :);

%%%%%%%%%%%%%%%%%%%%%%%%%%%%%%%%%%%%%%%%%%%%%%%%%%%%%%%%%%%%%%%%%%%%%%%
fig1 = figure('color',[1 1 1]);
sub_n0 = subplot(1,2,1);
[prior1, like1, tc1] = age_prior(counts(1),areas(1),4.5);
prior1 = prior1/sum(prior1);
like1 = like1/sum(like1);
post1 = prior1.*like1;
post1 = post1/sum(post1);
plot(tc1, prior1/dt,'linewidth',2);
hold on
```

```
plot(tc1,like1/dt,'linewidth',2);
plot(tc1,post1/dt,'k','linewidth',2);
axis([0 4.5 0 0.035/dt]);
xlabel({'Impact Unit Age, t (Ga)'});
ylabel({'Probability Density'});
grid on
legend('Prior, P(t)','Normalized Likelihood, P(k|t)','Posterior, P(t|k)
    ','location','northwest');

sub_n1 = subplot(1,2,2);
[prior2, like2, tc2] = age_prior(counts(3),areas(3),4.5);
prior2 = prior2/sum(prior2);
like2 = like2/sum(like2);
post2 = prior2.*like2;
post2 = post2/sum(post2);
plot(tc2, prior2/dt,'linewidth',2);
hold on
plot(tc2,like2/dt,'linewidth',2);
plot(tc2,post2/dt,'k','linewidth',2);
axis([0 4.5 0 0.07/dt]);
xlabel({'Impact Unit Age, t (Ga)'});
ylabel({'Probability Density'});
grid on

legend('Prior, P(t)','Normalized Likelihood, P(k|t)','Posterior, P(t|k)
    ','location','northwest');

fig1.PaperUnits = 'centimeters';
fig1.PaperPosition = [0 0 19.5 9.5];
print(fig1,'FIG1_inject_3Ga_4trunc','-dtiffn','-r500');

%%%%%%%%%%%%%%%%%%%%%%%%%%%%%%%%%%%%%%%%%%%%%%%%%%%%%%%%%%%%%%%%%%%%%%%
fig2 = figure('color',[1 1 1]);
semilogy(form_times(1:end-1),prod(fan_posts,1),'linewidth',2,'Color'
    ,[0, 0.4470, 0.7410]);
hold on
semilogy(form_times(1:end-1),prod(embed_posts,1),'linewidth',2,'
    linestyle','--','Color',[0.8500, 0.3250, 0.0980]);
plot([0 4],[0.05 0.05],'color','k','linestyle','--','linewidth',1);
plot([1 1],[0.0001 1], 'color',[0, 0.4470, 0.7410],'linestyle','--','
    linewidth',1);
plot([2.5 2.5],[0.0001 1], 'color',[0.8500, 0.3250, 0.0980],'linestyle'
    ,'--','linewidth',1);
text(0.15,0.02,{'At least one', 'younger', 'than 1 Ga'},'Color',[0,
    0.4470, 0.7410],'fontsize',8);
text(1.55,0.02,{'At least one', 'younger than', '2.5 Ga'},'Color'
    ,[0.8500, 0.3250, 0.0980],'fontsize',8);
annotation('arrow',[0.36 0.26],[0.5 0.5],'Color',[0, 0.4470, 0.7410]);
annotation('arrow',[0.63 0.53],[0.5 0.5],'Color',[0.8500, 0.3250,
    0.0980]);
axis([0 4 0.0001 1]);
```

```
legend('All Fan-Bearing','Localized Impact Trigger Excluded','location'
    ,'southwest');
set(gca,'fontsize',10);
xlabel('Time, t_{ref} (Gyr)');
ylabel({'CDF of Youngest Fan Age','P(t_{min} \geq t_{ref} | t_{ref})'})
    ;
grid minor
fig2.PaperUnits = 'centimeters';
fig2.PaperPosition = [0 0 11 9.5];
print(fig2,'FIG2_inject_3Ga_4trunc','-dtiffn','-r500');


%%%%%%%%%%%%%%%%%%%%%%%%%%%%%%%%%%%%%%%%%%%%%%%%%%%%%%%%%%%%%%%%%%%%%%%
fig3 = figure('color',[1 1 1]);
set(gca,'fontsize',10);
sub1 = subplot(1,2,1);
imagesc('XData',[0 4],'YData',[0 1],'CData',step_like) %CHANGED FOR LF2
hold on
step_sorted = sort(step_like(:));
step_cdf = 1 - cumsum(step_sorted)/sum(step_sorted);
step_val1 = min(step_sorted(step_cdf <= .997));
step_val2 = min(step_sorted(step_cdf <= .95));
step_val3 = min(step_sorted(step_cdf <= .68));
contour(t_,p_,step_like,[step_val1 step_val2 step_val3],'color','r','
    linewidth',1,'linestyle','-')

axis([0 4 0 1]);
c2 = colorbar;
xlabel({'Fan Formation Time','\tau_{form} (Ga)'});
ylabel({'Max Fan Formation Prob.','p_{max}'});
set(gca,'tickdir','out');
% plot([1.5 1.5],[0 1],'color','r','linewidth',1,'linestyle','--');
% plot([0 4],[0.5 0.5],'color','r','linewidth',1,'linestyle','--');

sub2 = subplot(1,2,2);
step_marg_pdf = sum(step_like,1)/sum(step_like,'all');
step_marg_cdf = cumsum(step_marg_pdf);
step_marg_p5 = min(t_(1,step_marg_cdf >= 0.95));
plot(t_(1,:),step_marg_pdf/dt2,'linewidth',2)
hold on
patch([step_marg_p5 t_(1,t_(1,:) >= step_marg_p5)],...
    [0 step_marg_pdf(t_(1,:) >= step_marg_p5)]/dt2, [1 0 0],...
    'FaceAlpha',.3,'EdgeAlpha',0);
legend('PDF','p < 0.05','location','southwest');
grid minor
xlabel({'Fan Formation Time','\tau_{form} (Ga)'});
ylabel('Marginalized PDF');
disp(sum(step_marg_pdf(t_(1,:) >= 3)));
set(gca,'tickdir','out');

fig3.PaperUnits = 'centimeters';
```

```
fig3.PaperPosition = [0 0 19.5 9.5];
print(fig3,'FIG3_inject_3Ga_4trunc','-dtiffn','-r500');



%%%%%%%%%%%%%%%%%%%%%%%%%%%%%%%%%%%%%%%%%%%%%%%%%%%%%%%%%%%%%%%%%%%%%%%%%%%%
fig4 = figure('color',[1 1 1]);
maximum = max(slope_like,[],'all');
[x,y,z] = find(slope_like == maximum);
set(gca,'fontsize',10);

sub3 = subplot(2,2,3);
axis([0,4,0,1]);
tau_p_marg = sum(slope_like,3,'omitnan');
imagesc('XData',[0 4],'YData',[0 1],'CData',tau_p_marg);
hold on
tau_p_sort = sort(tau_p_marg(:));
tau_p_cdf = 1-cumsum(tau_p_sort)/sum(tau_p_sort);
tau_p_val1 = min(tau_p_sort(tau_p_cdf <= .997));
tau_p_val2 = min(tau_p_sort(tau_p_cdf <= .95));
tau_p_val3 = min(tau_p_sort(tau_p_cdf <= .68));
contour(tt(:,:,1),pp(:,:,1),tau_p_marg,[tau_p_val1 tau_p_val2
    tau_p_val3],...
    'color','r','linewidth',1,'linestyle','-')
c3 = colorbar;
xlabel({'End of Fan Formation','\tau_{end} (Ga)'});
ylabel({'Max Fan Formation Prob.','p_{max}'});
set(gca,'tickdir','out');

sub4 = subplot(2,2,4);
dur_p_marg = squeeze(sum(slope_like,2,'omitnan'));
imagesc('XData',[0 4],'YData',[0 1],'CData',dur_p_marg);
hold on
dur_p_sort = sort(dur_p_marg(:));
dur_p_cdf = 1-cumsum(dur_p_sort)/sum(dur_p_sort);
dur_p_val1 = min(dur_p_sort(dur_p_cdf <= .997));
dur_p_val2 = min(dur_p_sort(dur_p_cdf <= .95));
dur_p_val3 = min(dur_p_sort(dur_p_cdf <= .68));
contour(squeeze(dd(:,1,:)),squeeze(pp(:,1,:)),dur_p_marg,[dur_p_val1
    dur_p_val2 dur_p_val3],...
    'color','r','linewidth',1,'linestyle','-')

xlabel({'Fan Formation Era Duration','\Delta\tau (Gyr)'});
ylabel({'Max Fan Formation Prob.','p_{max}'});
set(gca,'tickdir','out');
axis([0 4 0 1]);
c4 = colorbar;

sub5 = subplot(2,2,1);
tau_dur_marg = squeeze(sum(slope_like,1,'omitnan'))';
imagesc('XData',[0 4],'YData',[0 4],'CData',tau_dur_marg);
```

```
hold on
tau_dur_sort = sort(tau_dur_marg(:));
tau_dur_cdf = 1-cumsum(tau_dur_sort)/sum(tau_dur_sort);
tau_dur_val1 = min(tau_dur_sort(tau_dur_cdf <= .997));
tau_dur_val2 = min(tau_dur_sort(tau_dur_cdf <= .95));
tau_dur_val3 = min(tau_dur_sort(tau_dur_cdf <= .68));
contour(squeeze(dd(1,:,:)),squeeze(tt(1,:,:)),tau_dur_marg,[
    tau_dur_val1 tau_dur_val2 tau_dur_val3],...
    'color','r','linewidth',1,'linestyle','-')
v = [0 4; 4 4; 4 0];
f = [1 2 3];
patch('Faces',f,'Vertices',v,'FaceColor',[0.5 0.5 0.5])
ylabel({'Fan Formation Era Duration','\Delta\tau (Gyr)'});
xlabel({'End of Fan Formation','\tau_{end} (Ga)'});
set(gca,'tickdir','out');
axis([0 4 0 4]);
c5 = colorbar;

sub6 = subplot(2,2,2);
latest_prob = sum(slope_like,[1,3],'omitnan');
latest_prob = latest_prob/sum(latest_prob);
times = 0:0.1:4;
plot(times,latest_prob/dt3,'linewidth',2);
latest_cdf = cumsum(latest_prob);
cutoff = min(times(latest_cdf >= 0.95));
patch([cutoff times(times >= cutoff)],[0 latest_prob(times >= cutoff)]/
    dt3, [1 0 0],...
    'FaceAlpha',.3,'EdgeAlpha',0);
legend('PDF','p < 0.05');

grid minor
xlabel({'End of Fan Formation','\tau_{end} (Ga)'});
ylabel('Marginalized PDF');
set(gca,'tickdir','out');

fig4.PaperUnits = 'centimeters';
fig4.PaperPosition = [0 0 19.5 15];
print(fig4,'FIG4_inject_3Ga_4trunc','-dtiffn','-r500');

%%%%%%%%%%%%%%%%%%%%%%%%%%%%%%%%%%%%%%%%%%%%%%%%%%%%%%%%%%%%%%%%%%%%%%%%%%%
fig5 = figure('color',[1 1 1]);
maximum = max(slope_like,[],'all');
[x,y,z] = find(slope_like == maximum);
set(gca,'fontsize',10);

sub7 = subplot(1,2,2);
axis([0,4,0,1]);
tau_dur_marg = squeeze(sum(slope_like,1,'omitnan'))';
imagesc('XData',[0 4],'YData',[0 4],'CData',tau_dur_marg);
hold on
tau_dur_sort = sort(tau_dur_marg(:));
```

```
tau_dur_cdf = 1-cumsum(tau_dur_sort)/sum(tau_dur_sort);
tau_dur_val1 = min(tau_dur_sort(tau_dur_cdf <= .997));
tau_dur_val2 = min(tau_dur_sort(tau_dur_cdf <= .95));
tau_dur_val3 = min(tau_dur_sort(tau_dur_cdf <= .68));
contour(squeeze(dd(1,:,:)),squeeze(tt(1,:,:)),tau_dur_marg,[
    tau_dur_val1 tau_dur_val2 tau_dur_val3],...
    'color','r','linewidth',1,'linestyle','-')
v = [0 4; 4 4; 4 0];
f = [1 2 3];
patch('Faces',f,'Vertices',v,'FaceColor',[0.5 0.5 0.5])
xticks([0 1 2 3 4]);
ylabel({'Fan Formation Era Duration','\Delta\tau (Gyr)'});
xlabel({'End of Fan Formation','\tau_{end} (Ga)'});
set(gca,'tickdir','out');
axis([0 4 0 4]);
c5 = colorbar;

sub8 = subplot(1,2,1);
set(gca,'fontsize',10);
imagesc('XData',[0 4],'YData',[0 1],'CData',step_like) %CHANGED FOR LF2
hold on
step_sorted = sort(step_like(:));
step_cdf = 1 - cumsum(step_sorted)/sum(step_sorted);
step_val1 = min(step_sorted(step_cdf <= .997));
step_val2 = min(step_sorted(step_cdf <= .95));
step_val3 = min(step_sorted(step_cdf <= .68));
contour(t_,p_,step_like,[step_val1 step_val2 step_val3],'color','r','
    linewidth',1,'linestyle','-')

axis([0 4 0 1]);
c2 = colorbar;
xticks([0 1 2 3 4]);
xlabel({'Fan Formation Time','\tau_{form} (Ga)'});
ylabel({'Max Fan Formation Prob.','p_{max}'});
set(gca,'tickdir','out');
plot([3 3],[0 1],'color','r','linewidth',1,'linestyle','--');
plot([0 4],[0.5 0.5],'color','r','linewidth',1,'linestyle','--');

fig5.PaperUnits = 'centimeters';
fig5.PaperPosition = [0 0 19.5 7];
print(fig5,'FIG5_inject_3Ga_4trunc','-dtiffn','-r500');

%%%%%%%%%%%%%%%%%%%%%%%%%%%%%%%%%%%%%%%%%%%%%%%%%%%%%%%%%%%%%%%%%%%%%%%%%%%
fig6 = figure('color',[1 1 1]);
sortedposts = [fan_posts2;non_fan_posts];
sortedlikes = [fan_likelihoods;non_fan_likelihoods];

sort_exp_ages = sortedposts*tc;
sortedcums = cumsum(sortedposts,2);

olderror = zeros(212,1);
```

```
youngerror = zeros(212,1);
michael_est = zeros(212,1);

for k = 1:212
    temp_posts = cumsum(sortedposts(k,:));
    temp_like = sortedlikes(k,:);

    upper_bound = min(tc(temp_posts' >= 0.95));
    lower_bound = max(tc(temp_posts' <= 0.05));

    olderror(k) = upper_bound - sort_exp_ages(k);
    youngerror(k) = sort_exp_ages(k) - lower_bound;
    michael_est(k) = min(tc(temp_like' >= 0.5));
end

% errorbar(1:212,sort_exp_ages, youngerror, olderror,'o');
numfans = sum(hasfans);
[sorted_fan_exp_ages, idx] = sort(sort_exp_ages(1:numfans));
fan_upper = olderror(1:numfans);
fan_lower = youngerror(1:numfans);
sorted_fan_upper = fan_upper(idx);
sorted_fan_lower = fan_lower(idx);

errorbar(1:numfans,sorted_fan_exp_ages,sorted_fan_lower,
   sorted_fan_upper,'o')
hold on

[sorted_nonfan_exp_ages, idx2] = sort(sort_exp_ages(numfans+1:end));
nonfan_upper = olderror(numfans+1:end);
nonfan_lower = youngerror(numfans+1:end);
sorted_nonfan_upper = nonfan_upper(idx2);
sorted_nonfan_lower = nonfan_lower(idx2);

fan_michael = michael_est(1:numfans);
nonfan_michael = michael_est(numfans+1:end);

sort_fan_michael = fan_michael(idx);
sort_nonfan_michael = nonfan_michael(idx2);

errorbar(numfans+1:212,sorted_nonfan_exp_ages,sorted_nonfan_lower,
   sorted_nonfan_upper,'o')
plot(1:212,[sort_fan_michael;sort_nonfan_michael],'o','color','k');
axis([0 212 0 4]);

plot([0 212],[3.54 3.54],'--','color','k','linewidth',1);
plot([0 212],[3.74 3.74],'-.','color','k','linewidth',1);

legend({'Fan-Bearing','Non-Fan-Bearing','Michael et al. Estimates','A/H
    Boundary',...
    'N/H Boundary'},'location','southeast');

```

```
334 grid on
335 xlabel('AHi Unit Index');
336 ylabel('Age (Ga)');
337
338 fig6.PaperUnits = 'centimeters';
339 fig6.PaperPosition = [0 0 19.5 9.5];
340 print(fig6,'FIG6_inject_3Ga_4trunc','-dtiffn','-r500');
341
342 %%%%%%%%%%%%%%%%%%%%%%%%%%%%%%%%%%%%%%%%%%%%%%%%%%%%%%%%%%%%%%%%%%%%%%%
343 function [posterior, tc] = age_posterior(N,A,max_time)
344     % Set some constants
345     N1_ref = 5.84e-4;
346     N4_ref = 4.25e-5;
347
348     % Define the prior and posterior functions
349     t = (0:0.01:max_time)';
350     tc = 0.5*(t(1:end-1) + t(2:end));
351     dens_t = (N4_ref/N1_ref)*(N1_ref*t + (3.79e-14)*(exp(6.93*t)-1));
352     prior = diff(dens_t);
353     likelihood = poisspdf(N,0.5*(dens_t(1:end-1) + dens_t(2:end))*A);
354
355     % Define and renormalize the posterior
356     posterior = prior.*likelihood;
357     posterior = posterior./sum(posterior);
358 end
359
360 function [prior, likelihood,tc] = age_prior(N,A,max_time)
361     % Set some constants
362     N1_ref = 5.84e-4;
363     N4_ref = 4.25e-5;
364
365     % Define the prior and posterior functions
366     t = (0:0.01:max_time)';
367     tc = 0.5*(t(1:end-1) + t(2:end));
368     dens_t = (N4_ref/N1_ref)*(N1_ref*t + (3.79e-14)*(exp(6.93*t)-1));
369     prior = diff(dens_t);
370     likelihood = poisspdf(N,0.5*(dens_t(1:end-1) + dens_t(2:end))*A);
371
372     % Define and renormalize the posterior
373     posterior = prior.*likelihood;
374     posterior = posterior./sum(posterior);
375 end
```

Creates all the quantitative plots for Chapter 4. Lines 2, 5, and 9 should be changed to reflect desired input data (e.g. from the annulus check, the synthetic data, etc.). If the synthetic data is called on lines 5 or 9, it will override certain variables called in line 2. Remember to also change output filenames for each figure on lines 76, 98, 140, 223, 275, and 340.

Code C.8: fan_plots_young.m

```
clear all
load human_to_reduced_data/data.mat areas  hasembed hasclimatefans
    counts hasfans


load slopedata_3_young

slope_like = 10.^exp_likelihood;

load stepdata_young

step_like = 10.^exp_likelihood;
step_like(isnan(step_like)) = 0;
dt = 0.01;
dt2 = 0.05;
dt3 = 0.1;

form_times = 0:0.01:3.54;
posts = zeros(length(counts), length(form_times)-1);
posts2 = zeros(length(counts), length(form_times)-1);
likelihoods = zeros(length(counts), length(form_times)-1);

for i = 1:length(counts)
    [posterior, tc] = age_posterior(counts(i),areas(i),max(form_times));
    [~,likelihood,~] = age_prior(counts(i),areas(i),max(form_times));
    likelihoods(i,:) = cumsum(likelihood)/sum(likelihood);
    posts(i,:) = 1 - cumsum(posterior');
    posts2(i,:) = posterior';
end

fan_posts = posts(hasfans == 1,:);
fan_posts2 = posts2(hasfans == 1, :);
non_fan_posts = posts2(hasfans == 0, :);

fan_likelihoods = likelihoods(hasfans == 1,:);
non_fan_likelihoods = likelihoods(hasfans == 0,:);

embed_posts = posts(hasfans == 1 & (hasembed ==1 | hasclimatefans == 1)
    , :);

%%%%%%%%%%%%%%%%%%%%%%%%%%%%%%%%%%%%%%%%%%%%%%%%%%%%%%%%%%%%%%%%%%%%%%%
fig1 = figure('color',[1 1 1]);
sub_n0 = subplot(1,2,1);
[prior1, like1, tc1] = age_prior(counts(1),areas(1),3.54);
prior1 = prior1/sum(prior1);
like1 = like1/sum(like1);
post1 = prior1.*like1;
post1 = post1/sum(post1);
plot(tc1, prior1/dt,'linewidth',2);
hold on
```

```
plot(tc1,like1/dt,'linewidth',2);
plot(tc1,post1/dt,'k','linewidth',2);
axis([0 4.5 0 0.035/dt]);
xlabel({'Impact Unit Age, t (Ga)'});
ylabel({'Probability Density'});
grid on
legend('Prior, P(t)','Normalized Likelihood, P(k|t)','Posterior, P(t|k)
    ','location','northwest');

sub_n1 = subplot(1,2,2);
[prior2, like2, tc2] = age_prior(counts(3),areas(3),3.54);
prior2 = prior2/sum(prior2);
like2 = like2/sum(like2);
post2 = prior2.*like2;
post2 = post2/sum(post2);
plot(tc2, prior2/dt,'linewidth',2);
hold on
plot(tc2,like2/dt,'linewidth',2);
plot(tc2,post2/dt,'k','linewidth',2);
axis([0 4.5 0 0.07/dt]);
xlabel({'Impact Unit Age, t (Ga)'});
ylabel({'Probability Density'});
grid on

legend('Prior, P(t)','Normalized Likelihood, P(k|t)','Posterior, P(t|k)
    ','location','northwest');

fig1.PaperUnits = 'centimeters';
fig1.PaperPosition = [0 0 19.5 9.5];
print(fig1,'FIG1_young','-dtiffn','-r500');

%%%%%%%%%%%%%%%%%%%%%%%%%%%%%%%%%%%%%%%%%%%%%%%%%%%%%%%%%%%%%%%%%%%%%%%
fig2 = figure('color',[1 1 1]);
semilogy(form_times(1:end-1),prod(fan_posts,1),'linewidth',2,'Color'
    ,[0, 0.4470, 0.7410]);
hold on
semilogy(form_times(1:end-1),prod(embed_posts,1),'linewidth',2,'
    linestyle','--','Color',[0.8500, 0.3250, 0.0980]);
plot([0 4],[0.05 0.05],'color','k','linestyle','--','linewidth',1);
plot([1 1],[0.0001 1], 'color',[0, 0.4470, 0.7410],'linestyle','--','
    linewidth',1);
plot([2.5 2.5],[0.0001 1], 'color',[0.8500, 0.3250, 0.0980],'linestyle'
    ,'--','linewidth',1);
text(0.15,0.02,{'At least one', 'younger', 'than 1 Ga'},'Color',[0,
    0.4470, 0.7410],'fontsize',8);
text(1.55,0.02,{'At least one', 'younger than', '2.5 Ga'},'Color'
    ,[0.8500, 0.3250, 0.0980],'fontsize',8);
annotation('arrow',[0.36 0.26],[0.5 0.5],'Color',[0, 0.4470, 0.7410]);
annotation('arrow',[0.63 0.53],[0.5 0.5],'Color',[0.8500, 0.3250,
    0.0980]);
axis([0 4 0.0001 1]);
```

```
legend('All Fan-Bearing','Localized Impact Trigger Excluded','location','southwest');
set(gca,'fontsize',10);
xlabel('Time, t_{ref} (Gyr)');
ylabel({'CDF of Youngest Fan Age','P(t_{min} \geq t_{ref} | t_{ref})'});
grid minor
fig2.PaperUnits = 'centimeters';
fig2.PaperPosition = [0 0 11 9.5];
print(fig2,'FIG2_young','-dtiffn','-r500');


%%%%%%%%%%%%%%%%%%%%%%%%%%%%%%%%%%%%%%%%%%%%%%%%%%%%%%%%%%%%%%%%%%%%%%%%%%%%
fig3 = figure('color',[1 1 1]);
set(gca,'fontsize',10);
sub1 = subplot(1,2,1);
imagesc('XData',[0 3.54],'YData',[0 1],'CData',step_like) %CHANGED FOR LF2
hold on
step_sorted = sort(step_like(:));
step_cdf = 1 - cumsum(step_sorted)/sum(step_sorted);
step_val1 = min(step_sorted(step_cdf <= .997));
step_val2 = min(step_sorted(step_cdf <= .95));
step_val3 = min(step_sorted(step_cdf <= .68));
contour(t_,p_,step_like,[step_val1 step_val2 step_val3],'color','r','linewidth',1,'linestyle','-')

axis([0 3.54 0 1]);
c2 = colorbar;
xlabel({'Fan Formation Time','\tau_{form} (Ga)'});
ylabel({'Max Fan Formation Prob.','p_{max}'});
set(gca,'tickdir','out');
% plot([1.5 1.5],[0 1],'color','r','linewidth',1,'linestyle','--');
% plot([0 4],[0.5 0.5],'color','r','linewidth',1,'linestyle','--');

sub2 = subplot(1,2,2);
step_marg_pdf = sum(step_like,1)/sum(step_like,'all');
step_marg_cdf = cumsum(step_marg_pdf);
step_marg_p5 = min(t_(1,step_marg_cdf >= 0.95));
plot(t_(1,:),step_marg_pdf/dt2,'linewidth',2)
hold on
patch([step_marg_p5 t_(1,t_(1,:) >= step_marg_p5)],...
    [0 step_marg_pdf(t_(1,:) >= step_marg_p5)]/dt2, [1 0 0],...
    'FaceAlpha',.3,'EdgeAlpha',0);
legend('PDF','p < 0.05','location','northwest');
grid minor
xlabel({'Fan Formation Time','\tau_{form} (Ga)'});
ylabel('Marginalized PDF');
disp(sum(step_marg_pdf(t_(1,:) >= 3)));
set(gca,'tickdir','out');

```

```
fig3.PaperUnits = 'centimeters';
fig3.PaperPosition = [0 0 19.5 9.5];
print(fig3,'FIG3_young','-dtiffn','-r500');



%%%%%%%%%%%%%%%%%%%%%%%%%%%%%%%%%%%%%%%%%%%%%%%%%%%%%%%%%%%%%%%%%%%%%%%%%%%%
fig4 = figure('color',[1 1 1]);
maximum = max(slope_like,[],'all');
[x,y,z] = find(slope_like == maximum);
set(gca,'fontsize',10);

sub3 = subplot(2,2,3);
axis([0,3.54,0,1]);
tau_p_marg = sum(slope_like,3,'omitnan');
imagesc('XData',[0 3.54],'YData',[0 1],'CData',tau_p_marg);
hold on
tau_p_sort = sort(tau_p_marg(:));
tau_p_cdf = 1-cumsum(tau_p_sort)/sum(tau_p_sort);
tau_p_val1 = min(tau_p_sort(tau_p_cdf <= .997));
tau_p_val2 = min(tau_p_sort(tau_p_cdf <= .95));
tau_p_val3 = min(tau_p_sort(tau_p_cdf <= .68));
contour(tt(:,:,1),pp(:,:,1),tau_p_marg,[tau_p_val1 tau_p_val2
    tau_p_val3],...
    'color','r','linewidth',1,'linestyle','-')
c3 = colorbar;
xlabel({'End of Fan Formation','\tau_{end} (Ga)'});
ylabel({'Max Fan Formation Prob.','p_{max}'});
set(gca,'tickdir','out');

sub4 = subplot(2,2,4);
dur_p_marg = squeeze(sum(slope_like,2,'omitnan'));
imagesc('XData',[0 3.54],'YData',[0 1],'CData',dur_p_marg);
hold on
dur_p_sort = sort(dur_p_marg(:));
dur_p_cdf = 1-cumsum(dur_p_sort)/sum(dur_p_sort);
dur_p_val1 = min(dur_p_sort(dur_p_cdf <= .997));
dur_p_val2 = min(dur_p_sort(dur_p_cdf <= .95));
dur_p_val3 = min(dur_p_sort(dur_p_cdf <= .68));
contour(squeeze(dd(:,1,:)),squeeze(pp(:,1,:)),dur_p_marg,[dur_p_val1
    dur_p_val2 dur_p_val3],...
    'color','r','linewidth',1,'linestyle','-')

xlabel({'Fan Formation Era Duration','\Delta\tau (Gyr)'});
ylabel({'Max Fan Formation Prob.','p_{max}'});
set(gca,'tickdir','out');
axis([0 3.54 0 1]);
c4 = colorbar;

sub5 = subplot(2,2,1);
tau_dur_marg = squeeze(sum(slope_like,1,'omitnan'))';
```

```
imagesc('XData',[0 3.54],'YData',[0 3.54],'CData',tau_dur_marg);
hold on
tau_dur_sort = sort(tau_dur_marg(:));
tau_dur_cdf = 1-cumsum(tau_dur_sort)/sum(tau_dur_sort);
tau_dur_val1 = min(tau_dur_sort(tau_dur_cdf <= .997));
tau_dur_val2 = min(tau_dur_sort(tau_dur_cdf <= .95));
tau_dur_val3 = min(tau_dur_sort(tau_dur_cdf <= .68));
contour(squeeze(dd(1,:,:)),squeeze(tt(1,:,:)),tau_dur_marg,[
    tau_dur_val1 tau_dur_val2 tau_dur_val3],...
    'color','r','linewidth',1,'linestyle','-')
v = [0 3.54; 3.54 3.54; 3.54 0];
f = [1 2 3];
patch('Faces',f,'Vertices',v,'FaceColor',[0.5 0.5 0.5])
ylabel({'Fan Formation Era Duration','\Delta\tau (Gyr)'});
xlabel({'End of Fan Formation','\tau_{end} (Ga)'});
set(gca,'tickdir','out');
axis([0 3.54 0 3.54]);
c5 = colorbar;

sub6 = subplot(2,2,2);
latest_prob = sum(slope_like,[1,3],'omitnan');
latest_prob = latest_prob/sum(latest_prob);
times = 0:0.1:3.54;
plot(times,latest_prob/dt3,'linewidth',2);
latest_cdf = cumsum(latest_prob);
cutoff = min(times(latest_cdf >= 0.95));
patch([cutoff times(times >= cutoff)],[0 latest_prob(times >= cutoff)]/
    dt3, [1 0 0],...
    'FaceAlpha',.3,'EdgeAlpha',0);
legend('PDF','p < 0.05');

grid minor
xlabel({'End of Fan Formation','\tau_{end} (Ga)'});
ylabel('Marginalized PDF');
set(gca,'tickdir','out');

fig4.PaperUnits = 'centimeters';
fig4.PaperPosition = [0 0 19.5 15];
print(fig4,'FIG4_young','-dtiffn','-r500');

%%%%%%%%%%%%%%%%%%%%%%%%%%%%%%%%%%%%%%%%%%%%%%%%%%%%%%%%%%%%%%%%%%%%%%%%%%%%
fig5 = figure('color',[1 1 1]);
maximum = max(slope_like,[],'all');
[x,y,z] = find(slope_like == maximum);
set(gca,'fontsize',10);

sub7 = subplot(1,2,2);
axis([0,3.54,0,1]);
tau_dur_marg = squeeze(sum(slope_like,1,'omitnan'))';
imagesc('XData',[0 3.54],'YData',[0 3.54],'CData',tau_dur_marg);
hold on
```

```
tau_dur_sort = sort(tau_dur_marg(:));
tau_dur_cdf = 1-cumsum(tau_dur_sort)/sum(tau_dur_sort);
tau_dur_val1 = min(tau_dur_sort(tau_dur_cdf <= .997));
tau_dur_val2 = min(tau_dur_sort(tau_dur_cdf <= .95));
tau_dur_val3 = min(tau_dur_sort(tau_dur_cdf <= .68));
contour(squeeze(dd(1,:,:)),squeeze(tt(1,:,:)),tau_dur_marg,[
    tau_dur_val1 tau_dur_val2 tau_dur_val3],...
    'color','r','linewidth',1,'linestyle','-')
v = [0 3.54; 3.54 3.54; 3.54 0];
f = [1 2 3];
patch('Faces',f,'Vertices',v,'FaceColor',[0.5 0.5 0.5])
xticks([0 1 2 3 4]);
ylabel({'Fan Formation Era Duration','\Delta\tau (Gyr)'});
xlabel({'End of Fan Formation','\tau_{end} (Ga)'});
set(gca,'tickdir','out');
axis([0 3.54 0 3.54]);
c5 = colorbar;

sub8 = subplot(1,2,1);
set(gca,'fontsize',10);
imagesc('XData',[0 3.54],'YData',[0 1],'CData',step_like)
hold on
step_sorted = sort(step_like(:));
step_cdf = 1 - cumsum(step_sorted)/sum(step_sorted);
step_val1 = min(step_sorted(step_cdf <= .997));
step_val2 = min(step_sorted(step_cdf <= .95));
step_val3 = min(step_sorted(step_cdf <= .68));
contour(t_,p_,step_like,[step_val1 step_val2 step_val3],'color','r','
    linewidth',1,'linestyle','-')

axis([0 4 0 1]);
c2 = colorbar;
xticks([0 1 2 3 4]);
xlabel({'Fan Formation Time','\tau_{form} (Ga)'});
ylabel({'Max Fan Formation Prob.','p_{max}'});
set(gca,'tickdir','out');
plot([3 3],[0 1],'color','r','linewidth',1,'linestyle','--');
plot([0 4],[0.5 0.5],'color','r','linewidth',1,'linestyle','--');

fig5.PaperUnits = 'centimeters';
fig5.PaperPosition = [0 0 19.5 7];
print(fig5,'FIG5_young','-dtiffn','-r500');

%%%%%%%%%%%%%%%%%%%%%%%%%%%%%%%%%%%%%%%%%%%%%%%%%%%%%%%%%%%%%%%%%%%%%%%%%%%
fig6 = figure('color',[1 1 1]);
sortedposts = [fan_posts2;non_fan_posts];
sortedlikes = [fan_likelihoods;non_fan_likelihoods];

sort_exp_ages = sortedposts*tc;
sortedcums = cumsum(sortedposts,2);

```

```
olderror = zeros(212,1);
youngerror = zeros(212,1);
michael_est = zeros(212,1);

for k = 1:212
    temp_posts = cumsum(sortedposts(k,:));
    temp_like = sortedlikes(k,:);

    upper_bound = min(tc(temp_posts' >= 0.95));
    lower_bound = max(tc(temp_posts' <= 0.05));

    olderror(k) = upper_bound - sort_exp_ages(k);
    youngerror(k) = sort_exp_ages(k) - lower_bound;
    michael_est(k) = min(tc(temp_like' >= 0.5));
end

% errorbar(1:212,sort_exp_ages, youngerror, olderror,'o');
numfans = sum(hasfans);
[sorted_fan_exp_ages, idx] = sort(sort_exp_ages(1:numfans));
fan_upper = olderror(1:numfans);
fan_lower = youngerror(1:numfans);
sorted_fan_upper = fan_upper(idx);
sorted_fan_lower = fan_lower(idx);

errorbar(1:numfans,sorted_fan_exp_ages,sorted_fan_lower,
   sorted_fan_upper,'o')
hold on

[sorted_nonfan_exp_ages, idx2] = sort(sort_exp_ages(numfans+1:end));
nonfan_upper = olderror(numfans+1:end);
nonfan_lower = youngerror(numfans+1:end);
sorted_nonfan_upper = nonfan_upper(idx2);
sorted_nonfan_lower = nonfan_lower(idx2);

fan_michael = michael_est(1:numfans);
nonfan_michael = michael_est(numfans+1:end);

sort_fan_michael = fan_michael(idx);
sort_nonfan_michael = nonfan_michael(idx2);

errorbar(numfans+1:212,sorted_nonfan_exp_ages,sorted_nonfan_lower,
   sorted_nonfan_upper,'o')
plot(1:212,[sort_fan_michael;sort_nonfan_michael],'o','color','k');
axis([0 212 0 4]);

plot([0 212],[3.54 3.54],'--','color','k','linewidth',1);
plot([0 212],[3.74 3.74],'-.','color','k','linewidth',1);

legend({'Fan-Bearing','Non-Fan-Bearing','Michael et al. Estimates','A/H
    Boundary',...
    'N/H Boundary'},'location','southeast');
```

```
333
334 grid on
335 xlabel('AHi Unit Index');
336 ylabel('Age (Ga)');
337
338 fig6.PaperUnits = 'centimeters';
339 fig6.PaperPosition = [0 0 19.5 9.5];
340 print(fig6,'FIG6_young','-dtiffn','-r500');
341
342 %%%%%%%%%%%%%%%%%%%%%%%%%%%%%%%%%%%%%%%%%%%%%%%%%%%%%%%%%%%%%%%%%%%%%%%%%%%
343 function [posterior, tc] = age_posterior(N,A,max_time)
344     % Set some constants
345     N1_ref = 5.84e-4;
346     N4_ref = 4.25e-5;
347
348     % Define the prior and posterior functions
349     t = (0:0.01:max_time)';
350     tc = 0.5*(t(1:end-1) + t(2:end));
351     dens_t = (N4_ref/N1_ref)*(N1_ref*t + (3.79e-14)*(exp(6.93*t)-1));
352     prior = diff(dens_t);
353     likelihood = poisspdf(N,0.5*(dens_t(1:end-1) + dens_t(2:end))*A);
354
355     % Define and renormalize the posterior
356     posterior = prior.*likelihood;
357     posterior = posterior./sum(posterior);
358 end
359
360 function [prior, likelihood,tc] = age_prior(N,A,max_time)
361     % Set some constants
362     N1_ref = 5.84e-4;
363     N4_ref = 4.25e-5;
364
365     % Define the prior and posterior functions
366     t = (0:0.01:max_time)';
367     tc = 0.5*(t(1:end-1) + t(2:end));
368     dens_t = (N4_ref/N1_ref)*(N1_ref*t + (3.79e-14)*(exp(6.93*t)-1));
369     prior = diff(dens_t);
370     likelihood = poisspdf(N,0.5*(dens_t(1:end-1) + dens_t(2:end))*A);
371
372     % Define and renormalize the posterior
373     posterior = prior.*likelihood;
374     posterior = posterior./sum(posterior);
375 end
```

Analogous to 'fan_plots.m', but with plotting dimensions changed to produce the same plots for data where posterior AHi units were assumed to be truncated at 3.54 Ga. See Supplementary Figures to Chapter 4 above.

Code C.9: fan_plot_spatial_appendix_2.m

```
clear all
load human_to_reduced_data/data_spatial_2.mat

form_times = 0:0.01:4.5;
posts = zeros(length(counts), length(form_times)-1);
posts2 = zeros(length(counts), length(form_times)-1);
likelihoods = zeros(length(counts), length(form_times)-1);

for i = 1:length(counts)
   [posterior, tc] = age_posterior(counts(i),areas(i),max(form_times));
   [~,likelihood,~] = age_prior(counts(i),areas(i),max(form_times));
   likelihoods(i,:) = cumsum(likelihood)/sum(likelihood);
   posts(i,:) = 1 - cumsum(posterior');
   posts2(i,:) = posterior';
end

iseqlatfan = ((unitlats > -10) & (unitlats <= 10) & (hasfans == 1));
posts = posts(hasfans == 1,:);
fanunitlats = unitlats(hasfans == 1);
lowlats = posts(fanunitlats <= -10,:);
eqlats = posts((fanunitlats > -10) & (fanunitlats <= 10),:);
highlats = posts(abs(fanunitlats) > 10,:);
islowelev = mean_unit_fan_elev(hasfans ==1)<= -1500;
lowelevs = posts(islowelev==1,:);
ishighelev = mean_unit_fan_elev(hasfans ==1)> -1500;
highelevs = posts(ishighelev==1,:);

fig2 = figure('color',[1 1 1]);
semilogy(form_times(1:end-1),prod(lowlats,1),'linewidth',2,'Color',[0,
   0.4470, 0.7410]);
hold on
semilogy(form_times(1:end-1),prod(eqlats,1),'linewidth',2,'Color'
   ,[0.8500, 0.3250, 0.0980]);
semilogy(form_times(1:end-1),prod(highlats,1),'linewidth',2,'Color'
   ,[0.9290, 0.6940, 0.1250]);
semilogy(form_times(1:end-1),...
    prod(lowlats(hasembed(fanunitlats <= -10) ==1 | hasclimatefans(
   fanunitlats <= -10) ==1,...
    :),1),'linewidth',2,'linestyle','--','Color',[0, 0.4470, 0.7410]);
semilogy(form_times(1:end-1), prod(eqlats(hasembed(iseqlatfan,:)==1 |
   hasclimatefans(iseqlatfan,:)==1 ,:),1),...
    'linewidth',2,'linestyle','--','Color',[0.8500, 0.3250, 0.0980]);
semilogy(form_times(1:end-1),...
    prod(highlats(hasembed(fanunitlats > 10) ==1 | hasclimatefans(
   fanunitlats > 10) ==1,...
    :),1),'linewidth',2,'linestyle','--','Color',[0.9290, 0.6940,
   0.1250]);
plot([0 4],[0.05 0.05],'color','k','linestyle','--','linewidth',1);

axis([0 4 0.0001 1]);
```

```
legend('All Latitude < -10^o','Equatorial','All Latitude > 10^o','Low Lat. Local Impact excluded',...
    'Equatorial Local Impact Excluded','High Lat. Local Impact Excluded','location','southwest');
set(gca,'fontsize',10);
xlabel('Time, t_{ref} (Gyr)');
ylabel({'CDF of Youngest Fan Age','P(t_{min} \geq t_{ref} | t_{ref})'});
grid minor
fig2.PaperUnits = 'centimeters';
fig2.PaperPosition = [0 0 11 9.5];
print(fig2,'SPATIAL2','-dtiffn','-r500');

fig3 = figure('color',[1 1 1]);
semilogy(form_times(1:end-1),prod(lowelevs,1),'linewidth',2,'Color',[0, 0.4470, 0.7410]);
hold on
semilogy(form_times(1:end-1),prod(highelevs,1),'linewidth',2,'Color',[0.8500, 0.3250, 0.0980]);

embed2 = hasembed(hasfans == 1);
climate2 = hasclimatefans(hasfans == 1);
semilogy(form_times(1:end-1),...
    prod(lowelevs(embed2(islowelev==1) ==1 | climate2(islowelev)==1,...
    :),1),'linewidth',2,'linestyle','--','Color',[0, 0.4470, 0.7410]);
semilogy(form_times(1:end-1),...
    prod(highelevs(embed2(ishighelev==1) ==1 | climate2(ishighelev)==1,...
    :),1),'linewidth',2,'linestyle','--','Color',[0.8500, 0.3250, 0.0980]);
plot([0 4],[0.05 0.05],'color','k','linestyle','--','linewidth',1);

legend('All Elevation < -1500m','All Elevation > 1500m',...
    'Low Elev. Local Impact Excluded','High Elev. Local Impact Excluded',...
    'location','southwest');


grid minor
axis([0 4 0.0001 1]);
fig3.PaperUnits = 'centimeters';
fig3.PaperPosition = [0 0 11 9.5];
print(fig3,'SPATIAL3','-dtiffn','-r500');



%%%%%%%%%%%%%%%%%%%%%%%%%%%%%%%%%%%%%%%%%%%%%%%%%%%%%%%%%%%%%%%%%%%%%%%%%%%%
function [posterior, tc] = age_posterior(N,A,max_time)
    % Set some constants
    N1_ref = 5.84e-4;
```

```
    N4_ref = 4.25e-5;

    % Define the prior and posterior functions
    t = (0:0.01:max_time)';
    tc = 0.5*(t(1:end-1) + t(2:end));
    dens_t = (N4_ref/N1_ref)*(N1_ref*t + (3.79e-14)*(exp(6.93*t)-1));
    prior = diff(dens_t);
    likelihood = poisspdf(N,0.5*(dens_t(1:end-1) + dens_t(2:end))*A);

    % Define and renormalize the posterior
    posterior = prior.*likelihood;
    posterior = posterior./sum(posterior);
end

function [prior, likelihood,tc] = age_prior(N,A,max_time)
    % Set some constants
    N1_ref = 5.84e-4;
    N4_ref = 4.25e-5;

    % Define the prior and posterior functions
    t = (0:0.01:max_time)';
    tc = 0.5*(t(1:end-1) + t(2:end));
    dens_t = (N4_ref/N1_ref)*(N1_ref*t + (3.79e-14)*(exp(6.93*t)-1));
    prior = diff(dens_t);
    likelihood = poisspdf(N,0.5*(dens_t(1:end-1) + dens_t(2:end))*A);

    % Define and renormalize the posterior
    posterior = prior.*likelihood;
    posterior = posterior./sum(posterior);
end
```

Parses data output from 'reduce_spatial_2.m' and plots latitude and elevation splits of the CDF of the youngest fan age. See Supplementary Figures to Chapter 4 above.

C.2 Supplementary Figures

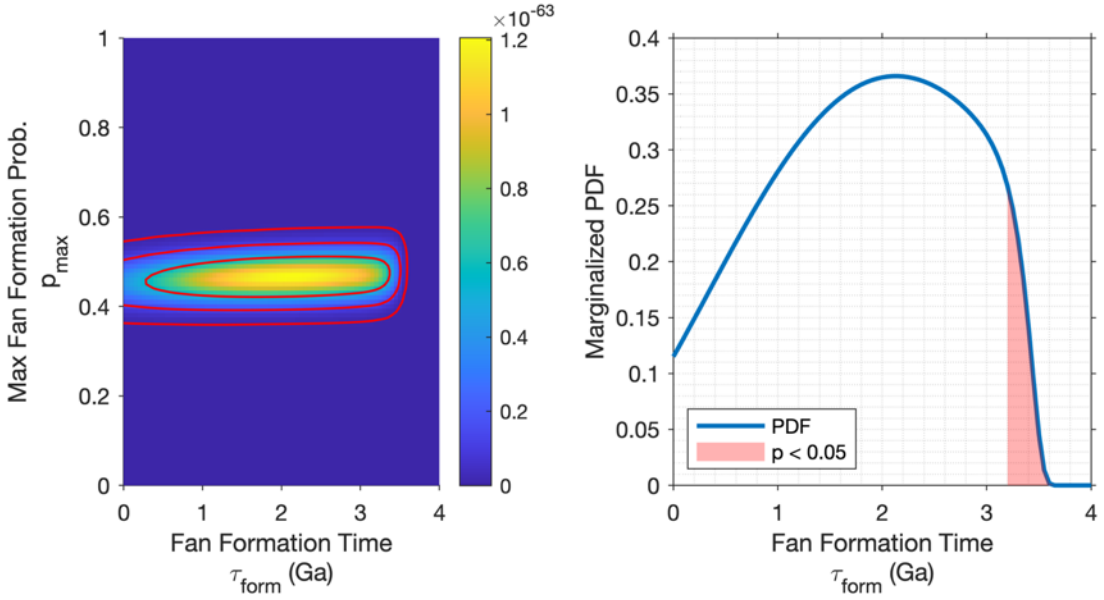

Figure C.1: Synthetic Data 1.5 Ga Pulse-Formation Model Parameter Retrieval. Pulse-model parameter retrievals where synthetic data was created assuming the pulse-formation model is correct (i.e. $\Delta\tau = 0$) with $\tau_{form} = 1.5$Ga and $p_{max} = 0.5$. Left: expected likelihood for the pulse-formation model, as a function of τ_{form} and at p_{max}. Red contours show 1-, 2-, and 3-σ confidence regions. Right: marginalized PDF for τ_{form}, assuming a uniform prior over p_{max}.

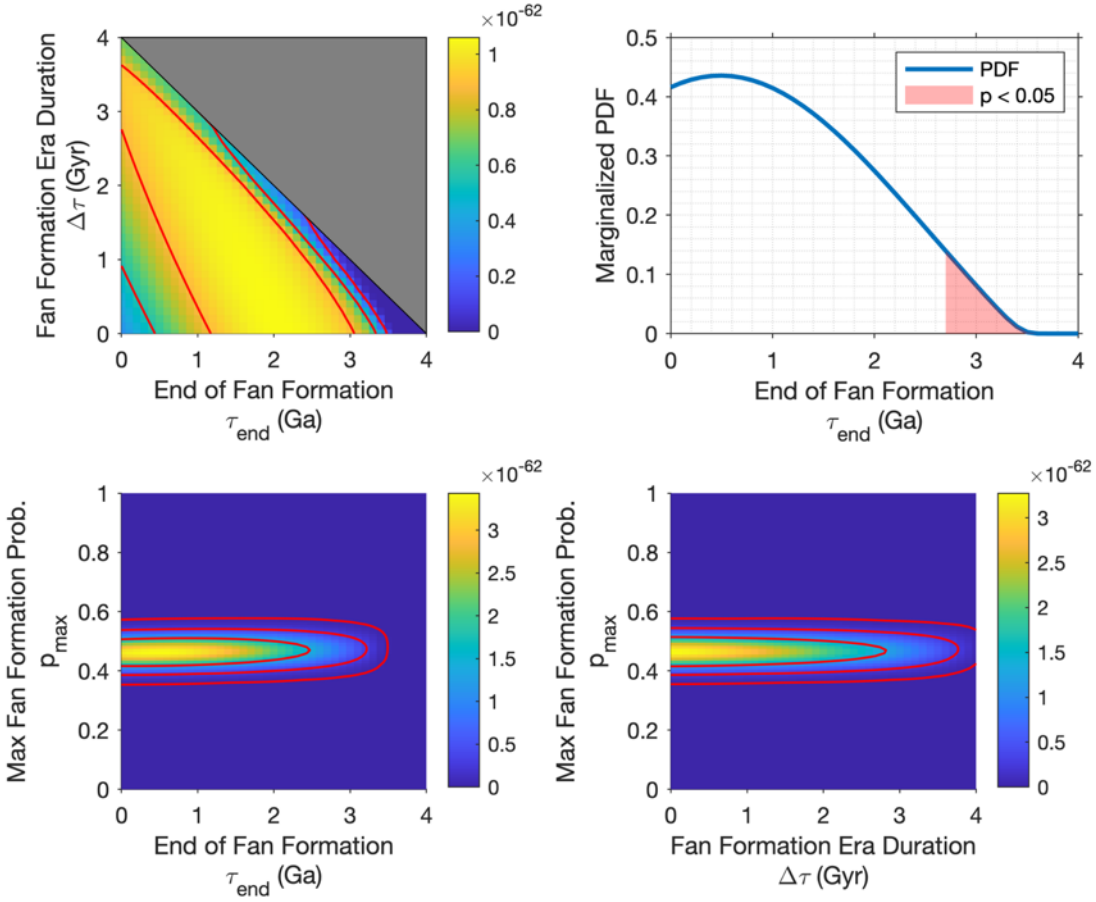

Figure C.2: Synthetic Data 1.5 Ga Prolonged-Formation Model Parameter Retrieval. Prolonged-model parameter retrievals where synthetic data was created assuming the pulse-formation model is correct (i.e. $\Delta\tau = 0$) with $\tau_{form} = 1.5$ Ga and $p_{max} = 0.5$. Top left: expected likelihood for the prolonged-formation model, as a function of τ_{end} and $\Delta\tau$, marginalizing over p_{max}. Greyed-out region was not modeled. Bottom left: expected likelihood for the prolonged-formation model, as a function of τ_{end} and at p_{max}, marginalizing over $\Delta\tau$. Top right: estimated posterior distribution for τ_{end}, marginalizing over $\Delta\tau$ and p_{max}. Bottom right: expected likelihood for the prolonged-formation model, as a function of p_{max} and $\Delta\tau$, marginalizing over τ_{end}. Red contours show 1-, 2-, and 3-σ confidence regions in the marginalized, 2-D parameter spaces. Note, this is not equivalent to the projection of confidence regions in 3-D parameter space down to 2-D.

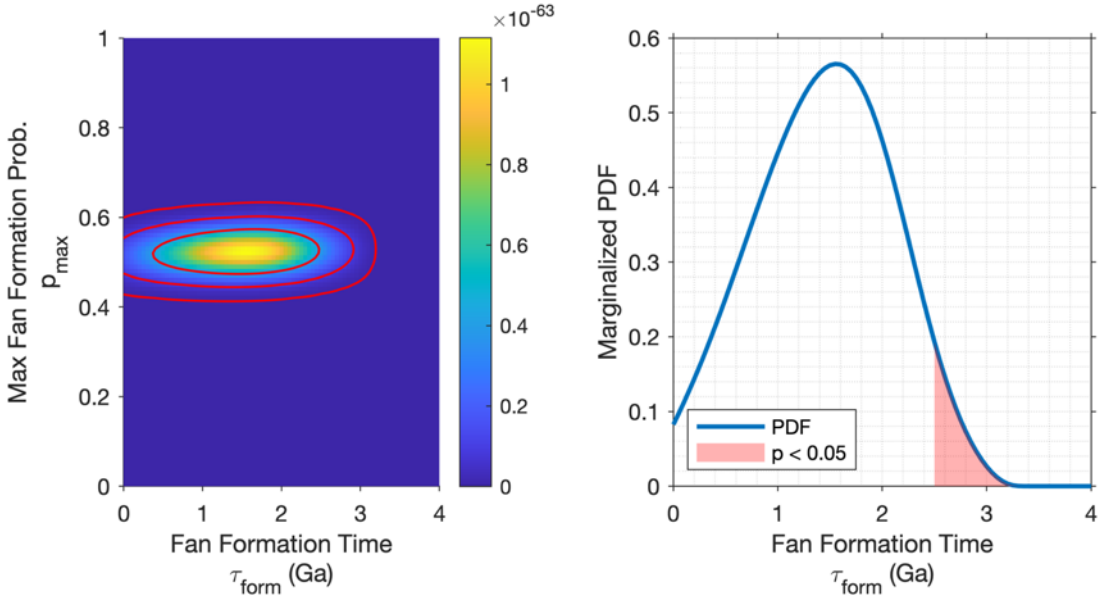

Figure C.3: Synthetic Data Inflated Area Pulse-Formation Model Parameter Retrieval. Pulse-model parameter retrievals where synthetic data was created assuming the pulse-formation model is correct (i.e. $\Delta\tau = 0$) with $\tau_{form} = 1.5$ Ga and $p_{max} = 0.5$, with count areas artificially inflated by a factor of 10. Left: expected likelihood for the pulse-formation model, as a function of τ_{form} and at p_{max}. Red contours show 1-, 2-, and 3-σ confidence regions. Right: marginalized PDF for τ_{form}, assuming a uniform prior over p_{max}.

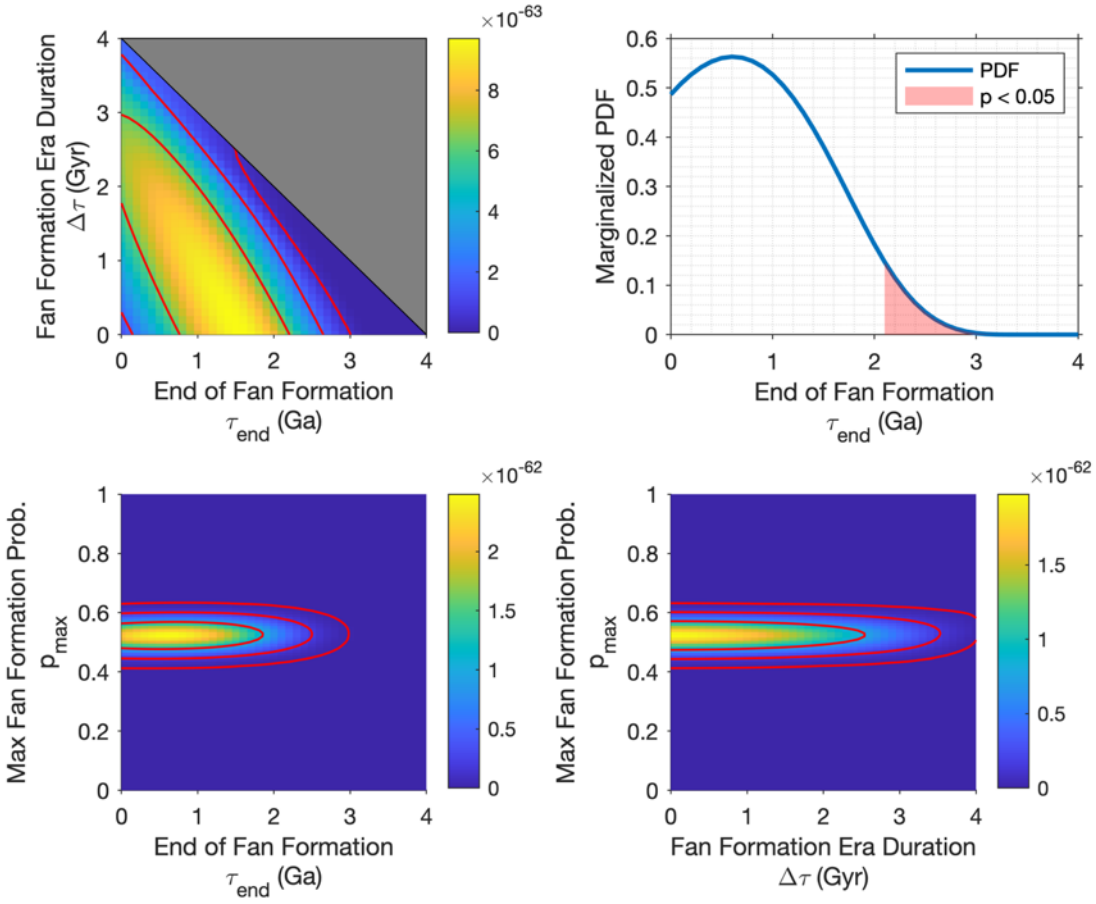

Figure C.4: Synthetic Data Inflated Area Prolonged-Formation Model Parameter Retrieval. Prolonged-model parameter retrievals where synthetic data was created assuming the pulse-formation model is correct (i.e. $\Delta\tau = 0$) with $\tau_{form} = 1.5$ Ga and $p_{max} = 0.5$, with count areas artificially inflated by a factor of 10. Top left: expected likelihood for the prolonged-formation model, as a function of τ_{end} and $\Delta\tau$, marginalizing over p_{max}. Greyed-out region was not modeled. Bottom left: expected likelihood for the prolonged-formation model, as a function of τ_{end} and at p_{max}, marginalizing over $\Delta\tau$. Top right: estimated posterior distribution for τ_{end}, marginalizing over $\Delta\tau$ and p_{max}. Bottom right: expected likelihood for the prolonged-formation model, as a function of p_{max} and $\Delta\tau$, marginalizing over τ_{end}. Red contours show 1-, 2-, and 3-σ confidence regions in the marginalized, 2-D parameter spaces. Note, this is not equivalent to the projection of confidence regions in 3-D parameter space down to 2-D.

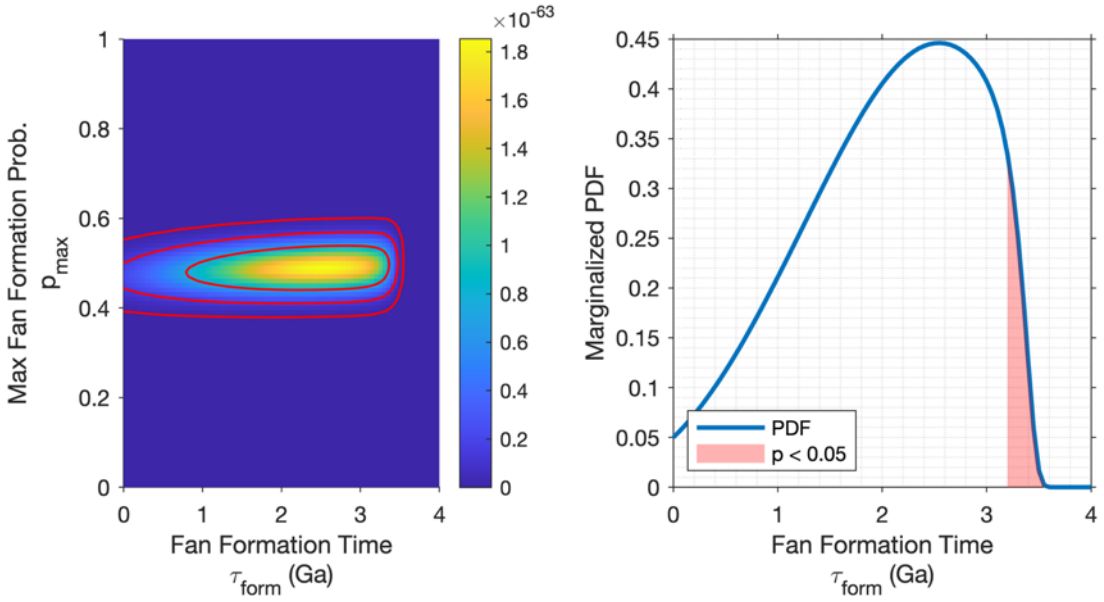

Figure C.5: Synthetic Data 3 Ga Pulse-Formation Model Parameter Retrieval. Pulse-model parameter retrievals where synthetic data was created assuming the pulse-formation model is correct (i.e. $\Delta\tau = 0$) with $\tau_{form} = 3$Ga and $p_{max} = 0.5$. Left: expected likelihood for the pulse-formation model, as a function of τ_{form} and at p_{max}. Red contours show 1-, 2-, and 3-σ confidence regions. Right: marginalized PDF for τ_{form}, assuming a uniform prior over p_{max}.

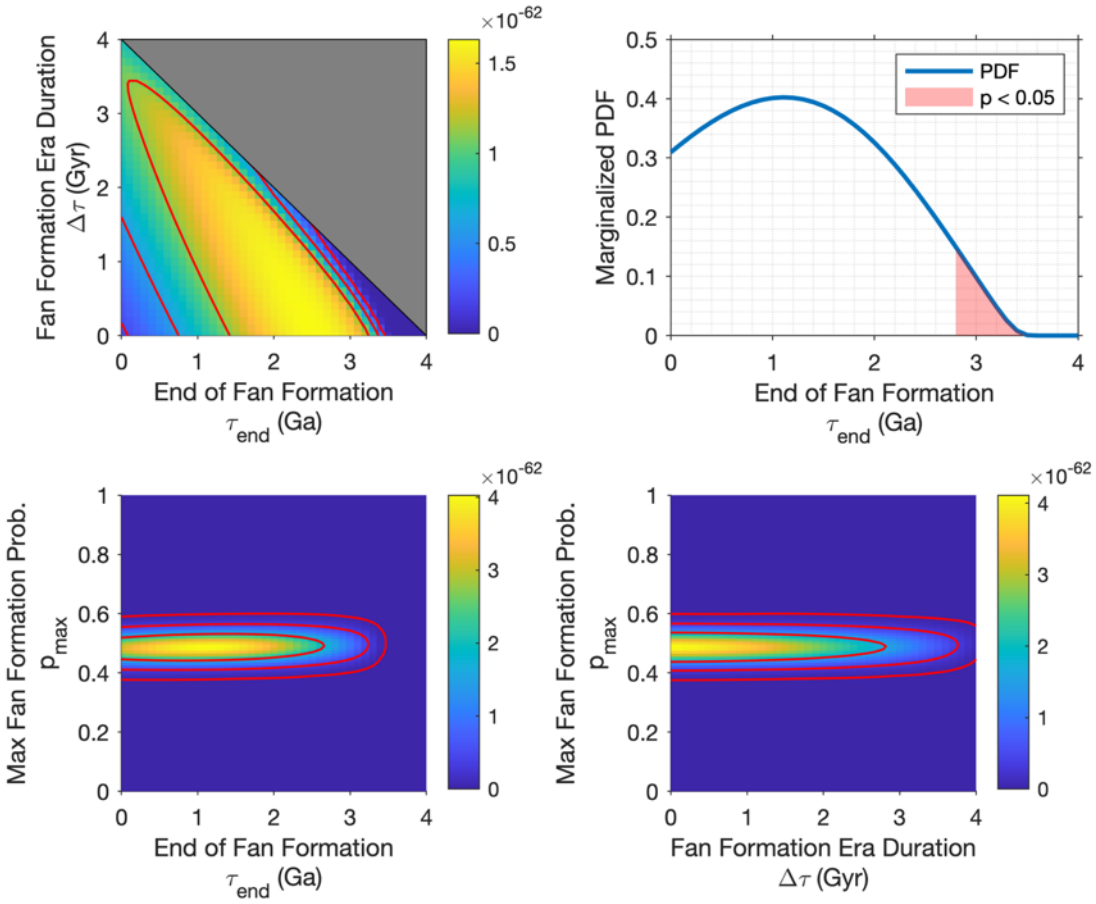

Figure C.6: Synthetic Data 3 Ga Prolonged-Formation Model Parameter Retrieval. Prolonged-model parameter retrievals where synthetic data was created assuming the pulse-formation model is correct (i.e. $\Delta\tau = 0$) with $\tau_{form} = 3$ Ga and $p_{max} = 0.5$. Top left: expected likelihood for the prolonged-formation model, as a function of τ_{end} and $\Delta\tau$, marginalizing over p_{max}. Greyed-out region was not modeled. Bottom left: expected likelihood for the prolonged-formation model, as a function of τ_{end} and at p_{max}, marginalizing over $\Delta\tau$. Top right: estimated posterior distribution for τ_{end}, marginalizing over $\Delta\tau$ and p_{max}. Bottom right: expected likelihood for the prolonged-formation model, as a function of p_{max} and $\Delta\tau$, marginalizing over τ_{end}. Red contours show 1-, 2-, and 3-σ confidence regions in the marginalized, 2-D parameter spaces. Note, this is not equivalent to the projection of confidence regions in 3-D parameter space down to 2-D.

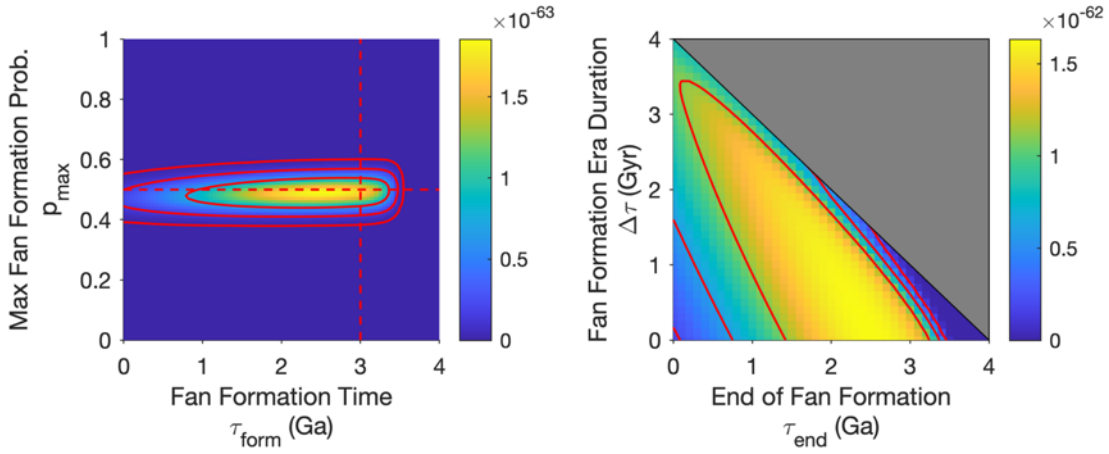

Figure C.7: Synthetic Data 3 Ga Summary. Side by side comparison of the main results in Figures C.5 and C.6. For an injection time of 3 Ga, the true parameter is within 1-σ of maximum likelihood retrieval.

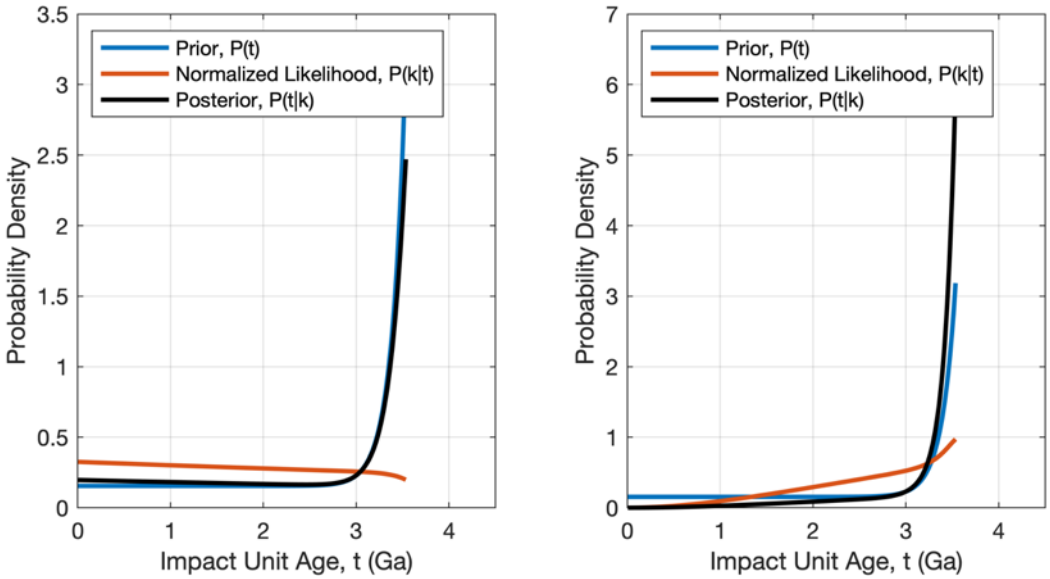

Figure C.8: Truncated Unit Age Estimation. Truncated age distributions at 3.54 Ga. These distributions cause essentially all of the AHi units to have ages > 3 Ga.

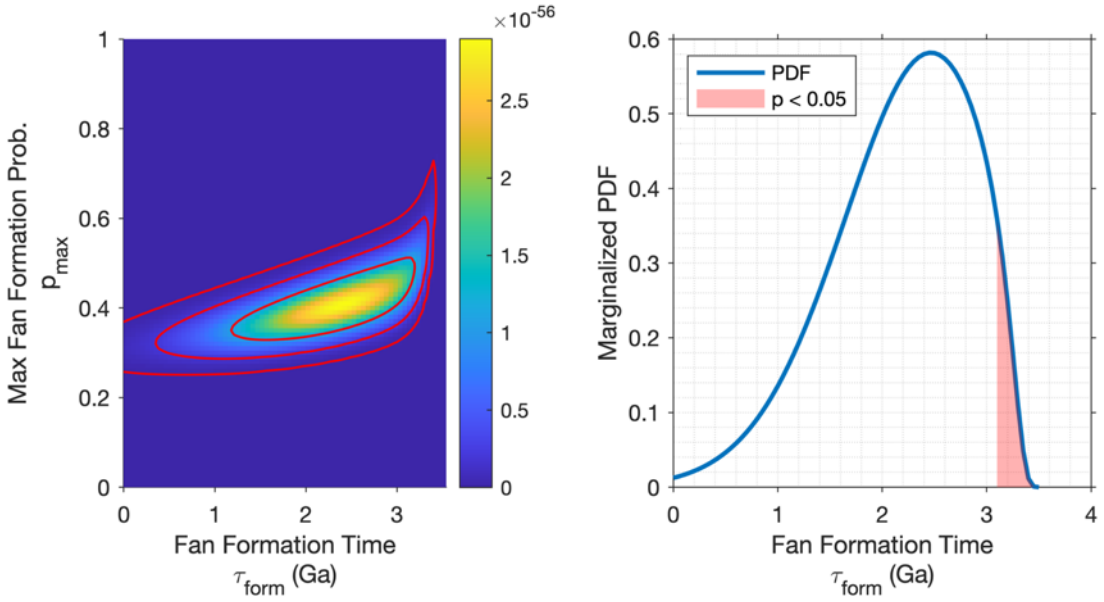

Figure C.9: Truncated Age Prior Sensitivity Test - Pulse Model. Pulse-model parameter retrievals where priors were truncated at 3.54 Ga. Left: expected likelihood for the pulse-formation model, as a function of τ_{form} and at p_{max}. Red contours show 1-, 2-, and 3-σ confidence regions. Right: marginalized PDF for τ_{form}, assuming a uniform prior over p_{max}. The results are skewed towards old ages.

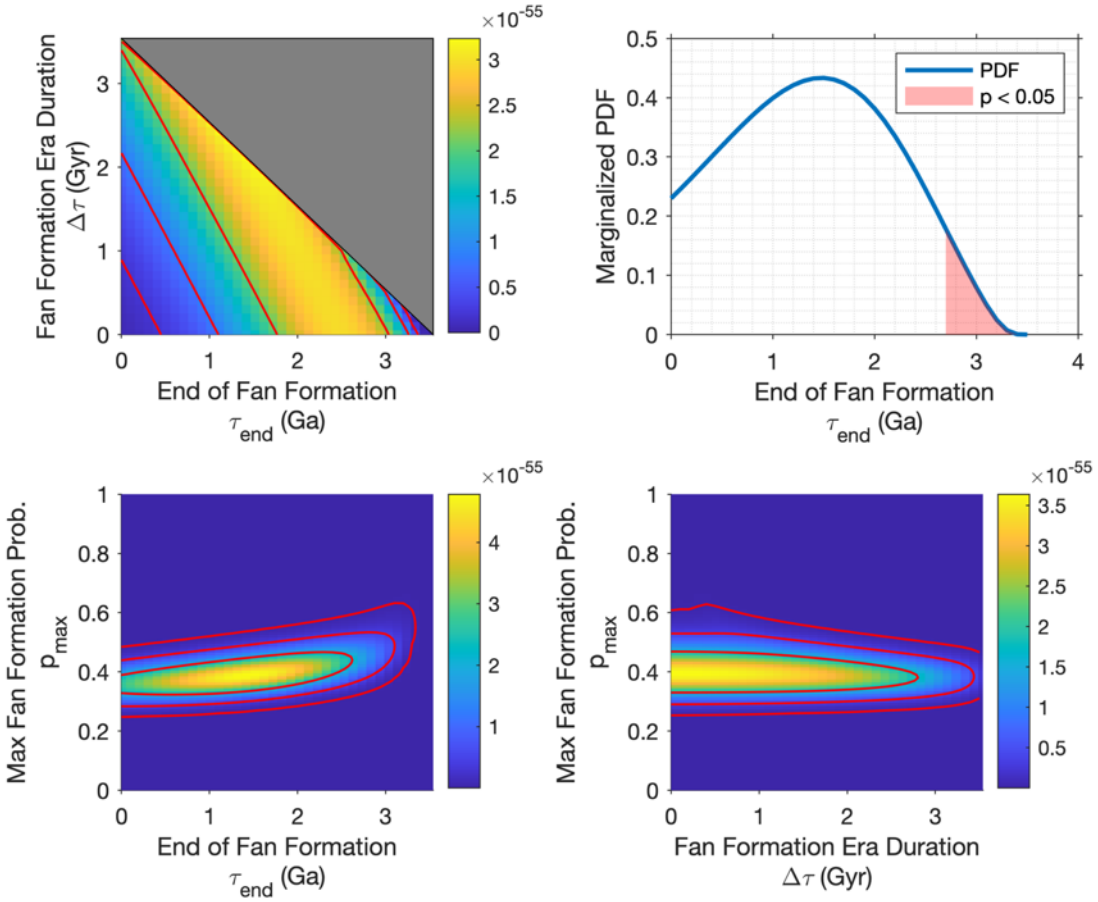

Figure C.10: Truncated Age Prior Sensitivity Test - Prolonged Model. Prolonged-model parameter retrievals where priors were truncated at 3.54 Ga. Top left: expected likelihood for the prolonged-formation model, as a function of τ_{end} and $\Delta\tau$, marginalizing over p_{max}. Greyed-out region was not modeled. Bottom left: expected likelihood for the prolonged-formation model, as a function of τ_{end} and at p_{max}, marginalizing over $\Delta\tau$. Top right: estimated posterior distribution for τ_{end}, marginalizing over $\Delta\tau$ and p_{max}. Bottom right: expected likelihood for the prolonged-formation model, as a function of p_{max} and $\Delta\tau$, marginalizing over τ_{end}. Red contours show 1-, 2-, and 3-σ confidence regions in the marginalized, 2-D parameter spaces. Note, this is not equivalent to the projection of confidence regions in 3-D parameter space down to 2-D.

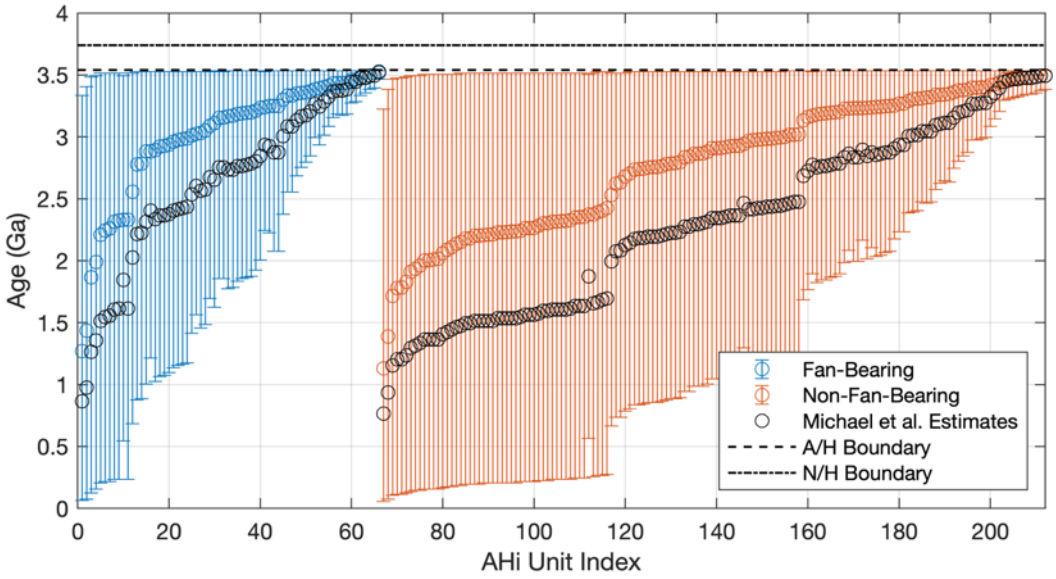

Figure C.11: Truncated Prior Unit Ages. Individual age estimates and 2σ error bars for each AHi unit using our Bayesian posterior method with the prior truncated at 3.54 Ga. Central estimates for our method are expected ages marginalized over age posterior distributions, while the Michael et al. (2016) method selects median values from the normalized likelihood function. Our strong prior systematically biases our age estimates upward, relative to Michael et al. (2016).

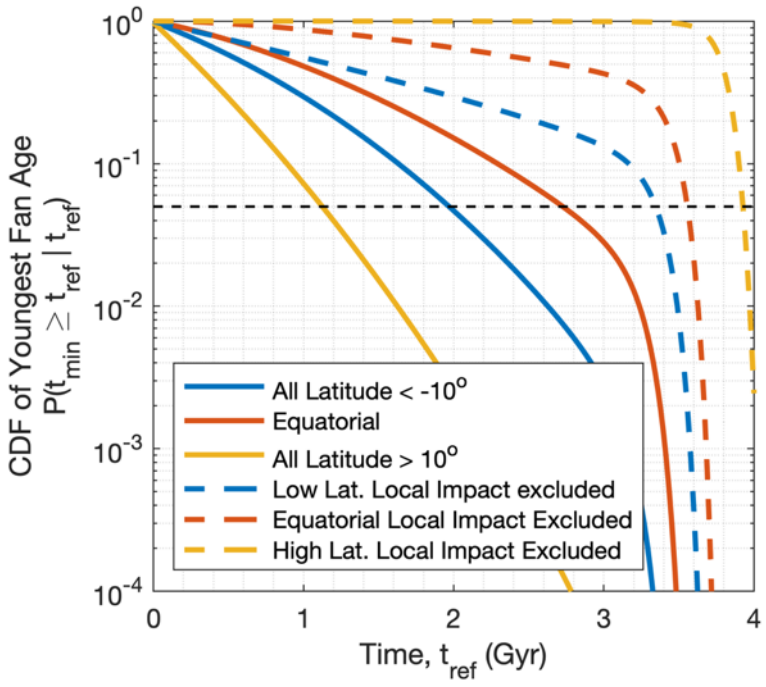

Figure C.12: Latitude Dependence of Fan Formation. Youngest Fan Age CDF. Cumulative probability distributions (CDF's) for the age of the youngest alluvial fan, t_{min}, as a function of t_{ref}. Colors/dashes indicate the population considered. Our results indicate that northern hemisphere fan formation had to have persisted into the last $\sim$ 1 Gyr, but that our constraint on the southern hemisphere is weaker. Note: this figure was made with a more recent version (May 2020 instead of March 2020) of the alluvial fans database.

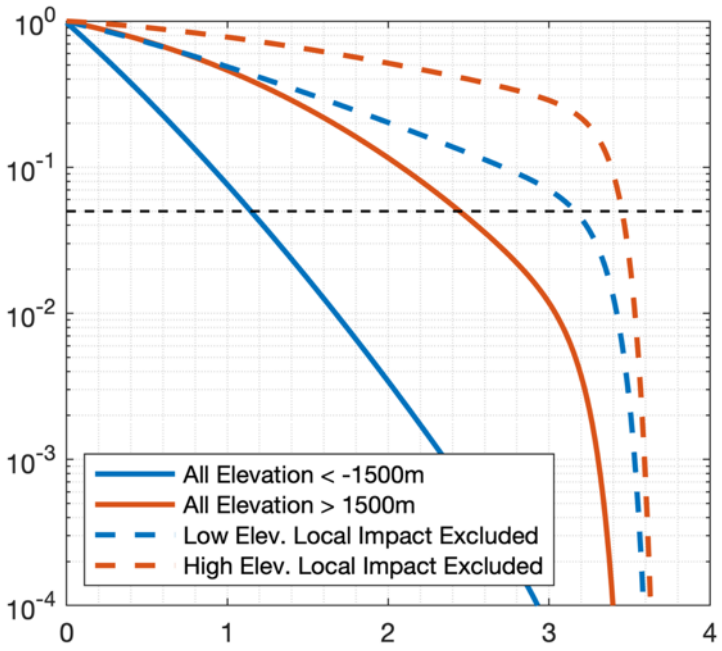

Figure C.13: Elevation Dependence of Fan Formation. Youngest Fan Age CDF. Cumulative probability distributions (CDF's) for the age of the youngest alluvial fan, t_{min}, as a function of t_{ref}. Colors/dashes indicate the population considered. Our results indicate that low-elevation fan formation had to have persisted into the last ~ 1 Gyr, but that our constraint on high-elevation fan formation is weaker. Note: this figure was made with a more recent version (May 2020 instead of March 2020) of the alluvial fans database.

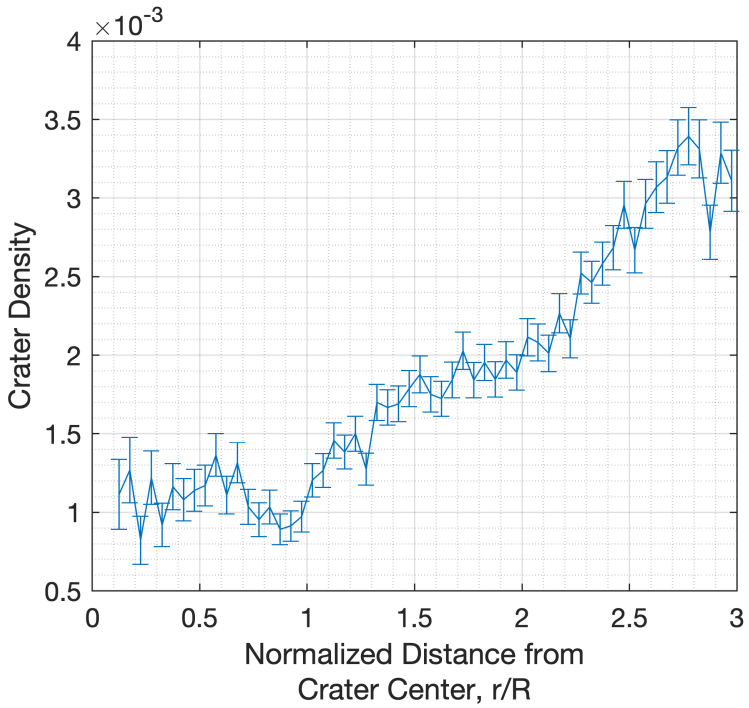

Figure C.14: Ejecta Crater Density as a Function of Distance from the Crater Center. Error bars are 1σ.

APPENDIX D

TABLE OF MARS INSTRUMENT ACRONYMS

MOLA	Mars Orbiter Laser Altimeter
THEMIS	Thermal Emission Imaging System
CTX	Context Camera
HRSC	High-Resolution Stereo Camera

Table D.1: Mars instrument acronyms used throughout thesis.

APPENDIX E

SUPPLEMENTARY FILES

See supplementary digital files.

E.1 Minor Planet Center Database

See supplementary digital files.

E.2 Elliptic Crater Database

See supplementary digital files.

E.3 AHi Unit Database

See supplementary digital files.